Eindhoven University of Technology

MASTER

Flat Plank Tire Tester Enhancements for Transient Measurements and Model Parametrization

Aertssen, Aron J.

Award date:
2023

EINDHOVEN UNIVERSITY OF TECHNOLOGY

Department of Mechanical Engineering
Dynamics and Control Research Group

SIEMENS

Flat Plank Tire Tester Enhancements for Transient Measurements and Model Parametrization

Automotive Technology
Master's Thesis

A.J. Aertssen
1007369
DC 2023.028

Supervisors:
ir. C. Lugaro (Siemens Digital Industries Software)
dr. ir. I.J.M. Besselink (Eindhoven University of Technology)

Eindhoven, April 2023

This report was made in accordance with the TU/e Code of Scientific Conduct for the Master thesis

Abstract

The Flat Plank Tire Tester is a moveable platform tire testing machine, which allows measuring the forces and moments generated by a tire subjected to various operating conditions. The transient properties of a tire can be accurately captured due to the extremely low operating speed of approximately 0.03 m/s. The recent implementation of a wheel rotation actuator provides the opportunity to investigate the longitudinal transient behavior of the tire under various operating conditions, but it removes the free-rolling ability of the tire. Furthermore, the implementation of the wheel rotation actuator has demonstrated the potential of state-of-the-art data acquisition and control hardware, servomotors, and control software with respect to the existing hardware and software of the machine.

In this thesis, the capabilities of the machine are extended in terms of both hardware and software. The hardware-related issues, that have been identified during this project, have been resolved or plans are set in motion to be implemented in the near future. The software issues are addressed by introducing new software for data logging and wheel rotation actuator control, providing a basis for the integration of the other electrically actuated degrees of freedom and automation of the measurements. A linear model of the wheel rotation actuator is adapted and extended to a nonlinear version. Both models are used to develop a controller that recreates free-rolling conditions. This allows for identifying the effective rolling radius of a tire in a convenient way. The functional testing results show that the controller ensures free-rolling conditions for passenger car tires throughout the allowable vertical force range of the machine. Furthermore, measurements are performed where the tire is subjected to nine longitudinal slip steps under varying operating conditions, which are the vertical force, tire inflation pressure, side slip angle, and camber angle. The results demonstrate that the Flat Plank can capture the longitudinal transient response, and it is clearly shown how the longitudinal transient response is influenced by the longitudinal slip magnitude and changing operating conditions. The measurement results are used to parameterize the linear transient model and the nonlinear transient model of Pacejka and the MF-Tyre/MF-Swift model. The models can represent the measured longitudinal transient response fairly accurately. However, the measurement results contain some non-tire-related dynamics, which significantly affect the measured transient response. Therefore, only quantitive conclusions can be drawn from the measurement and model results.

The main recommendation is to address the hardware issues of the machine, especially in terms of the electrically actuated degrees of freedom and the encoders. These two should be improved to bring the status of the machine to the next level to allow more consistent operating conditions of the tire, together with increasing the automation of the machine. Furthermore, it is strongly advised to repeat the pure longitudinal and combined slip measurements to obtain representative tire transient responses since the non-tire-related dynamics significantly influenced the measured transient responses presented in this work.

Keywords: Flat Plank Tire Tester, tire transient response, longitudinal slip, combined slip, tire transient modeling

Acknowledgments

First of all, I would like to express my sincere gratitude towards Carlo Lugaro and Igo Besselink, who have put boundless effort into guiding me throughout this project. Carlo, your vast knowledge of modeling and tire behavior, together with your enthusiasm, helped me a lot to bring this research to the next level. Igo, thank you for the opportunity to work on the Flat Plank Tire Tester, a truly unique machine, and for the freedom you gave me to shape my research. Your questions and feedback provided me with new insights to investigate and made me more critical of my findings.

I also want to thank my colleagues at TASS International. The four months at the office flew by and I learned a lot. Thank you all for answering my many questions and for the great atmosphere. A big thanks to the Automotive Technology lab personnel, Wietse, Erwin, and Gerard, who provided the necessary knowledge and skills to upgrade the Flat Plank. Also, the conversations at the coffee machine and the numerous cups of coffee always were welcome moments to unplug from my thesis.

Lastly, I would like to thank my family and friends for their non-technical and emotional support, which is and has been invaluable to me. A special thanks to Luuk and David, who were always available to discuss all sorts of questions, and who have proofread this thesis and provided me with helpful feedback. Additionally, David, you have been of great help with your knowledge of the Flat Plank and the wheel rotation actuator.

Once again, thank you all for the support!

List of Symbols

Symbol	Description	Unit
a	Half of contact length	m
c_{cx}	Longitudinal carcass stiffness	N/m
$C_{F\kappa}$	Longitudinal slip stiffness	N
$C'_{F\kappa}$	Local longitudinal slip stiffness	N
$C_{F\kappa,0}$	Initial value of longitudinal slip stiffness	N
c_{px}	Tread element stiffness per unit length	N
C_x	Longitudinal tire stiffness	N
C_z	Tire vertical stiffness	N/m
C_{z0}	Nominal tire vertical stiffness	N/m
d_{pi}	Normalized tire inflation pressure difference with respect to the nominal pressure	-
e	Error	N
e_w	Weighted error	N
e_r	Relative error	%
e_t	Total error	N
F_x	Longitudinal tire force	N
$F_{x,r}$	Longitudinal tire force reference	N
$F_{x,r0}$	Longitudinal tire force operating point	N
$F_{x,ss}$	Steady-state longitudinal tire force	N
F_y	Lateral tire force	N
$F_{y,ss}$	Steady-state lateral tire force	N
F_{meas}	Measured force	N
F_{model}	Modeled force	N
F_z	Vertical tire force	N
F_{z0}	Nominal vertical force	N
F_{z1}	Vertical force 1 used in measurements	N
F_{z2}	Vertical force 2 used in measurements	N
F_{z3}	Vertical force 3 used in measurements	N
g	Gravitational acceleration	m/s^2
i	Total speed reduction ratio	-
i_{RED}	Speed reduction ratio of hypoid reduction gearbox	-
i_{SD}	Speed reduction ratio of slewing drive	-
J_{eff}	Effective inertia	kg·m^2
J_M	Motor inertia	kg·m^2
J_T	Tire inertia	kg·m^2
J_{WS}	Worm screw inertia	kg·m^2
J_{WW}	Worm wheel inertia	kg·m^2
k_{eq}	Equivalent torsional stiffness of transmission components	Nm/rad
k_{cx}	Longitudinal carcass damping	Ns/m
k_i	Torsional stiffness of each component in the transmission	Nm/rad
$K_{x1}^{'}$	Normalized longitudinal slip stiffness	-
m	Fraction of the contact patch where adhesion occurs	-
m_c	Contact patch mass	kg
M_{in}	Input torque	Nm
M_F	Friction torque	Nm
M_M	Control effort torque	Nm

Symbol	**Description**	**Unit**
M_{out}	Output torque	Nm
M_{RED}	Torque between the motor and transmission	Nm
M_{SD}	Torque between transmission and tire	Nm
M_T	Tire torque	Nm
m_{veh}	Vehicle curb mass	kg
M_{WS}	Worm screw torque	Nm
M_{WW}	Worm wheel torque	Nm
p	Tire inflation pressure	bar
p_0	Nominal tire inflation pressure	bar
p_1	Tire inflation pressure 1 used in measurements	bar
p_2	Tire inflation pressure 2 used in measurements	bar
r_0	Free tire radius	m
r_e	Effective rolling radius	m
r_l	Loaded tire radius	m
$RMSE$	Root-mean-square error	N
s	Laplace variable	-
T_D	Tuning parameter of lead compensator	-
t_{kcx}	Longitudinal carcass damping coefficient	s
u	Longitudinal deformation of the contact patch	m
V_x	Road velocity	m/s
V_{sx}	Longitudinal wheel sliding velocity	m/s
V_{sx}^*	Longitudinal sliding velocity of the contact patch	m/s
V_{sy}	Lateral wheel sliding velocity of the rim	m/s
α	Steering angle	deg
α_{BL}	Half of the backlash angle	deg
α_l	Tuning parameter of lead compensator	-
γ	Camber angle	deg
ΔF_z	Change in vertical force before and after the longitudinal slip step application	N
η	Combined efficiency of slewing drive and hypoid reduction gearbox	%
θ_D	Relative angular displacement between input and output gear	rad
θ_M	Motor axle angular position	rad
θ_T	Tire angular position	rad
θ_w	Wheel angular position	rad
κ	Longitudinal slip	%
κ_0	Longitudinal slip operating point	%
κ_{act}	Actual longitudinal slip value	%
κ_{des}	Desired longitudinal slip value	%
κ'	Longitudinal slip of the contact patch	%
μ	Friction coefficient	-
σ_c	Contact patch relaxation length	m
σ_x	Longitudinal relaxation length	m
$\sigma_{x,0}$	Initial value of longitudinal relaxation length	m
ω	Servomotor reference velocity	rad/s
ω_m	Actual angular velocity of the servomotor	rad/s
ω_T	Tire angular speed	rad/s
$\omega_{T,0}$	Tire angular speed operating point	rad/s

Operator	**Description**
$\sim$	Linearized variable
$\cdot$	Time derivative of variable

Sign Convention for Force and Moment and Wheel Slip

The ISO convention is used in this work, which is shown in Figure 1.

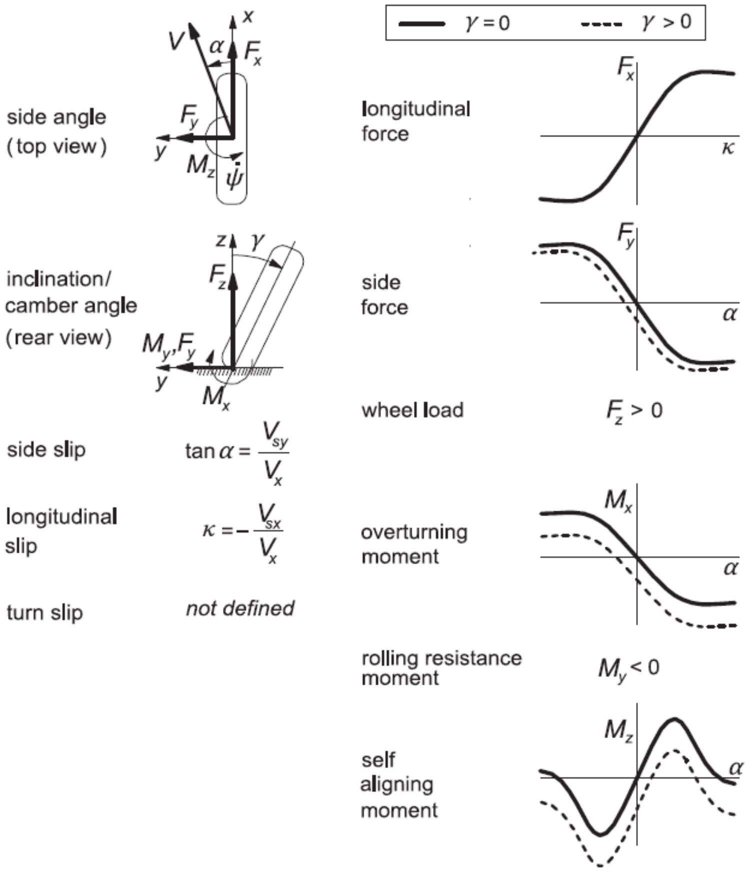

Figure 1: ISO convention. Adapted from [1, Appendix 1].

Contents

Chapter 1

Introduction

1.1 Project Context and Problem Definition

The pneumatic tire provides the interface between vehicle and road and plays a major role in the dynamics of a vehicle. The tire characteristics and the tire-road contact have been studied extensively to comprehend tire behavior under various circumstances. These studies have resulted in multiple models with distinct approaches to represent tire behavior. Tire measurement data lies at the foundation of tire research to understand and model tire behavior and to validate and parameterize models. Therefore, dedicated tire-testing machines have been developed to subject tires to the desired operating conditions and measure the forces and moments generated.

The Flat Plank Tire Tester is a movable platform machine and is employed at Eindhoven University of Technology (TU/e) since 2003. The machine has been used for many years by the TU/e and external companies to conduct tire research. Siemens Digital Industries Software (SI DW) is one of the companies that uses this machine to improve and parameterize their commercial MF-Tyre/MF-Swift tire model. Siemens SI DW is interested in the development of the machine to extend its capabilities and explore new research fields in order to improve their tire model. Therefore, they contribute to this project as a knowledgeable stakeholder and provide supervision and advice.

The capabilities of the machine have been extended by the implementation of the wheel rotation actuator by Van Blijderveen [2]. The actuator prescribes the rotational velocity of the mounted wheel, effectively governing the longitudinal sliding velocity of the tire. As a result, the machine allows to investigate the longitudinal transient behavior of a tire for pure and combined slip conditions under varying operating conditions. The Flat Plank has been extensively used to analyze lateral transient tire behavior [1, 3]. The existing literature does not present measurements to illustrate the longitudinal transient behavior. This thesis closes this gap.

However, it proves challenging to perform these measurements with the Flat Plank machine in its current status. Additionally, the wheel rotation actuator removes the free-rolling capability of the wheel due to the inherent characteristics of the actuator. As a result, it is time-consuming to identify the effective rolling radius, which is required for the longitudinal slip measurements. Furthermore, the Flat Plank has been improved incrementally over the years, which leads to actuators and measurement systems varying in age, wear, and level of sophistication. Consequently, the control interfaces for the different degrees of freedom of the machine vary, which means that the motion of each actuator is solely dependent on the input of the operator without the possibility of linking it to other measured states of the machine. This leads to a challenging process to execute longitudinal slip measurements. Also, the data acquisition hardware and software are outdated and partially obsolete. In contrast, the implementation of the wheel rotation actuator has shown the possibilities of state-of-the-art data acquisition and control hardware, servomotors, and control software.

1.2 Research Objectives

The goal of this research is to identify the longitudinal transient response of a tire under varying operating conditions. However, the problem definition given in the previous section illustrates the encountered difficulties in achieving this goal. Therefore, new software will be developed to provide a control interface for the wheel rotation actuator, together with the possibility to log the measured states of the machine. The software will provide the possibility to input the desired longitudinal slip value and enable the wheel rotation once the road displacement is initiated by the operator. Additionally, it must allow for the extension of its functionalities for future developments. Furthermore, a controller will be designed to recreate the free-rolling conditions of the tire to simplify the identification of the effective rolling radius. A model of the wheel rotation actuator will be developed to design and test the controller, whereafter its performance is verified on the machine. Pure longitudinal and combined slip measurements under various operating conditions will be executed where the tire is subjected to longitudinal slip steps to obtain the longitudinal transient response. The measurement results are used to parameterize three tire models, which are the linear transient model, the nonlinear transient model of Pacejka [1], and the MF-Tyre/MF-Swift model of Siemens DI SW [4]. A comparison is made between the results of the models and the measurement results to investigate the accuracy of the transient models, together with an analysis of the dependency of the transient model parameters on the operating conditions.

In summary, four objectives are defined, which are listed below.

1. The design and implementation of software for actuator control and data logging.
2. The design of a free-rolling controller to identify the effective rolling radius of a tire, together with testing the controller to assess its performance.
3. The execution of longitudinal and combined slip measurements to determine the longitudinal tire response under varying operating conditions.
4. The evaluation of the accuracy of the linear transient model, the nonlinear transient model of Pacejka [1], and the MF-Tyre/MF-Swift model [4] in terms of the longitudinal transient response.

1.3 Contributions of this Thesis

Multiple proposals to resolve the issues of the machine have already been implemented in the course of this project and after the measurements performed for this thesis. Some other improvements have been set in motion to be implemented in the near future. They will lead to better measurement results, simplify the operation of the machine, and allow the automation of measurements in the future together with the developed software and the free-rolling controller. Additionally, the software will provide a foundation for the implementation of electric actuation of the other degrees of freedom.

The measurements presented in this thesis will show the extended capabilities of the machine in terms of longitudinal slip actuation. As a result, new fields of tire research become accessible to contribute to the development and validation of tire models. This thesis discusses three tire models that have been parameterized using the measurement results, as a first step into tire modeling using this novel type of measurement.

1.4 Thesis Outline

Chapter 2 describes the literature review that has been performed on the topics of tire testing, the Flat Plank Tire Tester, and transient tire behavior. Subsequently, an overview of the current hardware and software status of the Flat Plank Tire Tester is given in Chapter 3, to coherently summarize the status for future reference. Chapter 4 explains the developed software to log data and control actuators. The free-rolling controller is implemented in this software, for which the wheel rotation actuator model to design the controller and functional testing results are described in Chapter 5. Both the software and free-rolling controller are employed to perform longitudinal slip measurements for varying operating conditions. The results of these measurements are presented in Chapter 6. In Chapter 7, the measurement results are employed to parameterize three tire models and to investigate to what extent the models are capable of representing the longitudinal tire transient behavior. Additionally, the influence of operating conditions on the model parameters is discussed. The last chapter provides the conclusions of this thesis, together with recommendations for future research.

Chapter 2

Literature Review

2.1 Tire Testing

The tire has a vital role in the driving behavior of a road vehicle, as it is the only interface of the vehicle with the road. The tire transmits the forces required to support and move a vehicle [5]. Therefore, tires are highly engineered components whose performance is designed to meet the requirements of a vehicle manufacturer such as handling, traction, and wear [6, 3]. The substantial influence of the tire on vehicle behavior raises the need to evaluate tire behavior early in the design process, which is facilitated by the application of virtual vehicle and tire models.

Several approaches to tire modeling exist to create mathematical models for simulation purposes. These approaches can be divided into three main categories: empirical, simple physics-based, and detailed physics-based models. The empirical models describe measured tire behavior through mathematical formulas, which may contain a multitude of parameters. These parameters are usually determined using regression analysis to obtain a satisfactory fit to the measurement data. A well-known semi-empirical model is the *Magic Formula* tire model, which is based on a sin(arctan) formula yielding an excellent fit, but fails to provide the cause of the perceived tire behavior. A physics-based model, such as the relatively simple brush model, is particularly helpful to better understand the physics behind the tire behavior. Detailed physics-based models are used to perform a thorough analysis to gain more in-depth knowledge of tires. For example, *RMOD-K* [7] is a detailed model that uses a finite element approach to subdivide the tire into many smaller, simpler parts that allow the input of, e.g., a three-dimensional road unevenness. This model category may be suitable to investigate the effects of changing material properties or tire structure [1].

Tire testing is required to develop, improve and parametrize these models. For example, the parameters of the *Magic Formula* tire model are determined using measurement data. Dedicated testing facilities using various approaches have been developed, and each method has its strengths and weaknesses. A distinction in testing facilities can be made between outdoor and indoor testing. Outdoor testing on the road captures realistic conditions in which a tire normally operates: different road surfaces, ambient temperatures, and dry, wet, or snowy roads. The tire-testing trailer of TASS International allows testing of passenger car and motorcycle tires at any road surface and almost any condition [8]. However, it is difficult to precisely control the environmental conditions during outdoor testing. With indoor testing, it is possible to more accurately control environmental factors. The most challenging conditions to recreate are the road surface and curvature. The indoor tests are traditionally performed on an internal or external drum, an example is the Tire Measurement Tower shown in Figure 2.1. These types of machines can have an asphalt surface to represent actual road surface conditions, but have a road curvature. Machines, like the MTS Flat-Trac® depicted in Figure 2.2, do not have the road curvature. This machine is basically a large belt-grinder, which employs sandpaper to represent road surface conditions. Wheel forward speed levels can be produced by both these types of machines that are typical of driving scenarios. Drum and belt tire testing machines are explained in detail in [1, Chapter 12]. The Flat Plank Tire Tester is a moveable platform tire tester operating at very low velocities, as opposed to the high-velocity operation of the MTS Flat-Trac® and Tire Measurement Tower. This research focuses on the Flat Plank Tire Tester.

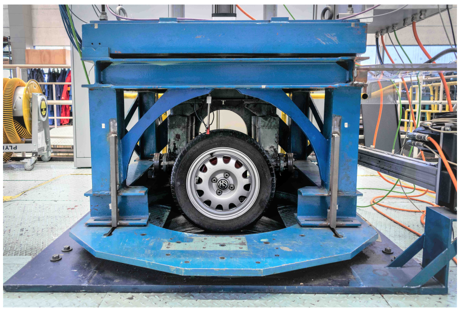

Figure 2.1: Tire Measurement Tower placed on the dynamometer at the Automotive Lab of the Eindhoven University of Technology [9, Figure 2.1].

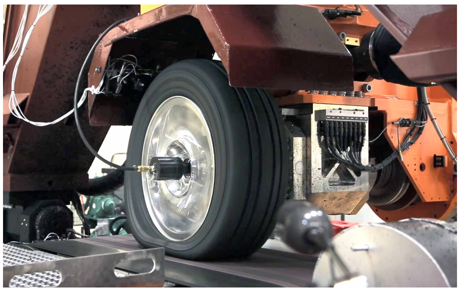

Figure 2.2: MTS Flat-Trac® Tire Force & Moment Measurement system [10].

2.2 Flat Plank Tire Tester

The Flat Plank Tire Tester, illustrated in Figure 2.3, was developed in 1960 at Delft University of Technology. The machine is employed at the Eindhoven University of Technology (TU/e) since 2003. The Flat Plank Tire Tester moves a plank covered in sandpaper, the yellow part in Figure 2.3, from one side to the other with a tire pressed against it. The wheel is mounted on a measurement hub, equipped with strain gauges, which measure the forces acting on the wheel axle. These measured forces are transformed into forces and moments at the tire contact patch, according to ISO conventions [2, 11].

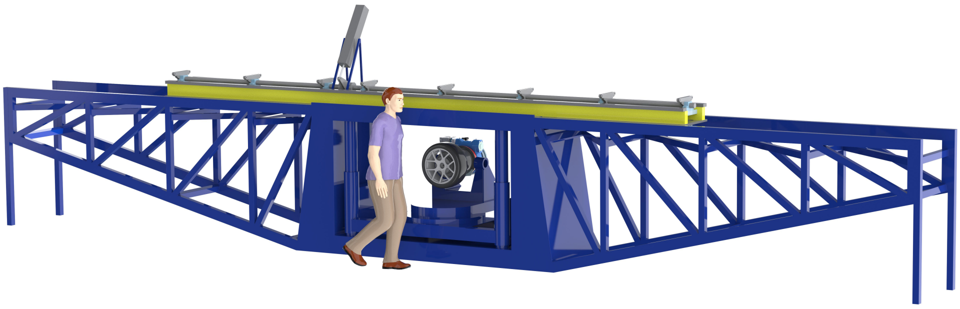

Figure 2.3: Render of the Flat Plank Tire Tester in its current state.

The plank can move with two fixed velocities, approximately 0.0015 m/s and 0.03 m/s. The vertical position of the wheel center with respect to the plank can be adjusted to obtain the desired vertical force on the tire. The maximum allowed vertical force is 8 kN. It is possible to steer the wheel 360°, but in practice, the used range is ±90°. Furthermore, the plank can be tilted to ±15° to represent road camber. The measurement hub can also be cambered to ±30°, thus allowing a total range of ±45°. Cleats can be attached to the plank to determine the enveloping behavior of a tire. The allowable tire radius that can be mounted ranges from 0.210 m to 0.387 m. The Flat Plank Tire Tester provides a means to perform stiffness, transient slip, camber, impulse turning, and cleat measurements at very low speeds. These measurements are used to determine tire properties such as the vertical, longitudinal, and lateral stiffness, and the effective rolling radius. The Flat Plank is also used to support optical measurements, which provide direct measurements of the tire carcass deformation. Pijs [12] developed a rim equipped with an optical sensor, which has been used in measurements on the TASS International tire-testing trailer, to validate the carcass representation of the TreadSim tire model. Shetty [13] addressed the recommendations of Pijs [12] to improve the accuracy of the optically measured data and performed similar measurements on the Flat Plank. The low-speed operation means that the optical hardware, which has a relatively low frame rate, captures ample frames to obtain the marker positions.

The most recent addition to the Flat Plank Tire Tester is the wheel rotation actuator, introduced by Van Blijderveen [2]. He implemented an electric servomotor to control the rotational speed of the tire in order to introduce a longitudinal slip. The wheel rotation actuator is depicted in Figure 2.4. The design consists of ① the electric servomotor, ② the hypoid reduction gearbox, ③ the slewing drive, and ④ the flexplate drum. The figure also shows ⑤ the measurement hub and ⑥ the mounted tire. The hypoid reduction gearbox and slewing drive compose the transmission, which is necessary to convert the high-speed, low-torque operation of the servomotor to the low-speed, high-torque required. A flexplate drum is used to deal with axial, radial, and angular alignment errors, and to only transmit the motor torque. The flexplate drum consists of two thin metal sheets (flexplates) separated by a rigid drum. The flexplates are exceptionally stiff towards in-plane forces and torsion in comparison with out-of-plane forces and bending. Therefore, a braking or driving torque can be transferred, while the forces and moments in the other directions remain minimal. The drum connects the output of the transmission with the central shaft of the measurement hub to which the wheel is connected.

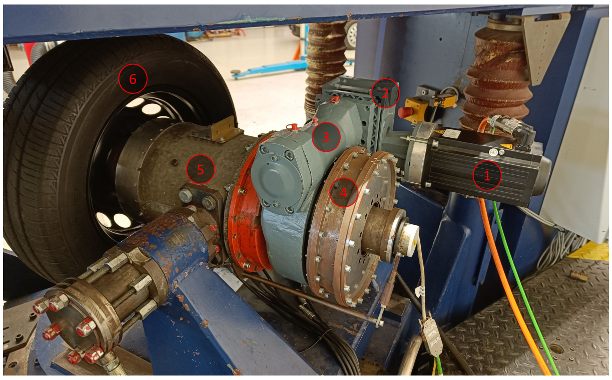

Figure 2.4: ①-④ wheel rotation actuator, ⑤ measurement hub and ⑥ tire of the Flat Plank Tire Tester.

Van Blijderveen [2] subjects the tire to a longitudinal slip by using the servomotor in speed control, which means that the servomotor tracks the supplied reference wheel velocity ω. This wheel velocity has to be determined for the desired longitudinal slip level κ based on the plank velocity V_x and the effective rolling radius r_e of the tire by

$$\omega = \frac{V_x}{r_e}(1+\kappa). \tag{2.1}$$

The effective rolling radius is determined when the tire is rolling freely and longitudinal slip κ is equal to zero. However, due to the inherent self-locking of the slewing drive, it is no longer possible to freely rotate the tire by moving the plank when the tire is pressed against it. Self-locking means that the input can drive the output, but the slewing drive locks up when the output tries to drive the input. As a result, the wheel will remain fully locked and does not rotate when the tire is pressed against the plank and the plank starts moving. As a result, Van Blijderveen needed to disconnect the flexplates so the tire can rotate freely again. This allows performing a measurement to obtain the required data to calculate the effective rolling radius, whereafter the flexplates need to be connected again so the servomotor can control the angular wheel velocity. The effective rolling radius of a tire is dependent on the measurement conditions to which the tire is subjected. This means that this time-consuming process of disconnecting the flexplates has to be repeated if any changes in the measurement conditions are desired. For that reason, Van Blijderveen [2] suggests recreating the free-rolling conditions of a tire by introducing a controller that minimizes the longitudinal force of the tire, then the flexplates do not need to be uncoupled.

The current status of the hardware and software of the Flat Plank is discussed in Chapter 3. Additionally, this chapter describes the issues of the machine, together with implemented or proposed solutions.

2.3 Transient Tire Behavior

Tires respond with a certain lag when a sudden change of input occurs. This phenomenon is called the relaxation behavior of a tire, which is primarily dependent on the traveled distance and the excitation frequency. The Flat Plank Tire Tester is suitable to measure relaxation behavior. The low-speed operation eliminates the speed-dependent response of the tire since rubber is a viscoelastic material, whose response is dependent on the excitation frequency. Therefore, the low-speed operation of the Flat Plank allows for ignoring the viscous effect of the rubber, meaning that only the elastic response remains.

The relaxation behavior can be represented by a first-order system response using the linear transient model of Pacejka [1]. The transfer function of the longitudinal force response is given by

$$\frac{F_x}{\kappa} = \frac{C'_{F\kappa}}{\frac{\sigma_x}{|V_x|}s+1}, \tag{2.2}$$

where F_x is the longitudinal tire force, $C'_{F\kappa}$ is the local longitudinal slip stiffness, σ_x is the longitudinal relaxation length, V_x is the forward velocity, s is the Laplace variable and κ is the longitudinal slip. The relaxation length is dependent on the operating conditions of the tire, such as the vertical force and the tire inflation pressure. This model suffices to model the response for small steps in longitudinal slip but fails to incorporate the reducing relaxation length for large slip steps [1, 14].

In the research of Van Blijderveen [2], the wheel rotation actuator is used to perform slip step measurements for different levels of longitudinal slip at a constant vertical force. Also, different vertical forces for two constant levels of slip are considered. Figure 2.5 shows the longitudinal forces, which gradually build up and level off to a constant value, for different levels of slip. The force responses for the different slip values clearly show the longitudinal relaxation behavior, and it is seen that the relaxation length decreases with increasing slip. Additionally, the plot shows that the positive slip levels (driving) produce a higher absolute force than their negative counterpart (braking). The difference in peak friction that is observed between driving and braking moments is expected and explained by a theoretical perspective [15]. Figure 2.6 shows that an increasing vertical force leads to an increasing relaxation length, which complies with the theory of lateral relaxation length.

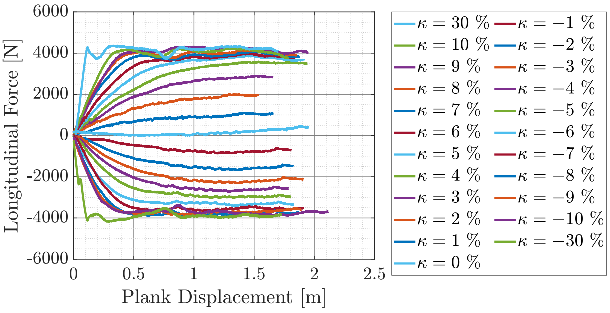

Figure 2.5: 23 longitudinal tire force measurements as a function of plank displacement after the slip steps with levels ranging from -30 % to 30 % for a constant vertical force. Adapted from [2, Figure 6.1].

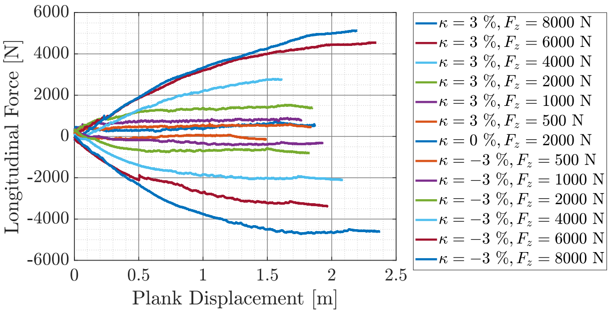

Figure 2.6: The longitudinal force as a function of plank displacement for slip step measurements at 3 %, 0 %, and -3 % at various vertical forces. Adapted from [2, Figure 6.2].

Dinesh [16] analyzed measurements done on a Flat-Trac machine to identify and evaluate the parameters of two transient tire models, which are able to describe the longitudinal transient response of the tire. The linear transient tire model, given by (2.2), is only valid for small steps of slip. The non-linear transient tire model can cope with higher slip values by including a physical model of the tire carcass stiffness and damping. By comparing the models to the measurement data, it is shown that both models can fairly accurately represent the measured response over the entire input range of excitation frequencies provided the slip level is close to 0 %. Furthermore, Dinesh [16] identified a significant difference in the longitudinal stiffness of a tire between a standstill and a rolling condition.

2.4 Summary

This chapter describes the necessity of tire testing to develop and parameterize different types of tire models. Different methods of tire testing are presented, both indoor and outdoor, with their respective advantages and disadvantages. A more detailed review of the Flat Plank Tire Tester is given since this machine is the focal point of this research. Lastly, a short introduction to transient tire behavior is given.

Chapter 3

Flat Plank Status

Several modifications have been made to the Flat Plank in recent years to improve the machine and enable new types of measurements. Additionally, multiple hardware and software changes have been made throughout this project. The incremental nature of these improvements results in the actuators and measurement systems varying in age, wear, and level of sophistication. This chapter describes the hardware and software status of the Flat Plank at the start of this project with the known issues and proposed and implemented solutions. In this way, all changes, issues, and solutions are grouped together for future reference.

3.1 Hardware

This section explains the layout of the machine, the actuation of the degrees of freedom, and the data acquisition system. This provides a more detailed overview of the hardware architecture of the machine. The known hardware issues of the machine will be described, followed by their corresponding solutions. The hardware architecture of the Flat Plank is shown in Figure 3.1, which visualizes the hardware components that are required to perform measurements. The components are described in more detail in the following subsections.

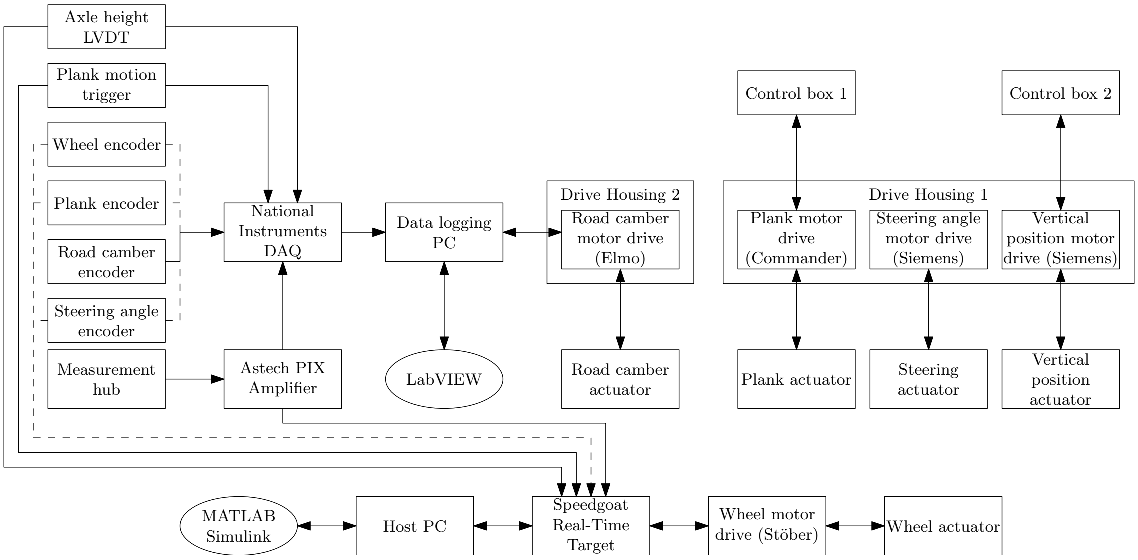

Figure 3.1: Hardware architecture of the Flat Plank. The dashed lines indicate that the corresponding encoders can be connected to either the National Instruments system or the Speedgoat.

Layout of the Machine

The machine, shown in Figure 3.2, consists of three parts, which are the main frame ①, the measurement platform ②, and the plank ③. Each part is explained in more detail below.

① The main frame supports the measurement platform and the plank. The main frame supports the measurement platform with four pillars that constrain all motion except the z-translation of the measurement platform. The plank is supported by the main frame via ball bearings, which constrain the plank in the negative and positive y-direction and the negative z-direction. Additionally, the plank is supported in the negative and positive y- and z-direction by linear roller bearings around the location where the tire is in contact with the road to carry the high loads occurring there.

② The measurement platform moves vertically with respect to the main frame and contains a turntable on which the measurement hub is mounted. The measurement hub is shown in Figure 2.4 in more detail. The turntable allows rotating (steering) the wheel about the z-direction, and the measurement hub can rotate about the local x-axis with respect to the turntable to introduce a wheel camber angle. The measurement hub can move laterally in the local y-direction with respect to the turntable to position the wheel with respect to the road.

③ The plank, of which a cross-section is shown in Figure 3.3, consists of the plank structure ① and the road ②. The road is a steel plate covered with sandpaper. The road is suspended from the plank structure via the connecting rods ③. The connecting rods, the rotation support ④, and the half-moon guide ⑤ constrain the road in y- and z-direction with respect to the plank structure. The road can rotate about the x-axis with respect to the plank structure to create a road camber angle, as shown in Figure 3.4. This is achieved by rotating the camber rotation rod ⑥, which rotates the camber rotation triangle ⑦ that is attached to the connecting rods. Movement in the x-direction of the road with respect to the plank structure is constrained by a ball bearing on both ends of the road.

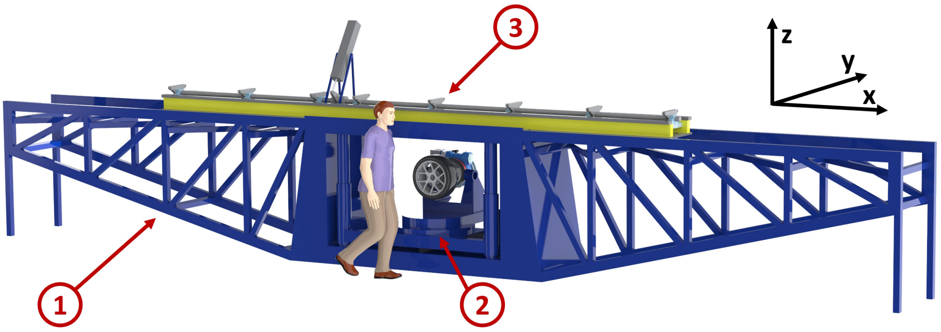

Figure 3.2: Render of the Flat Plank Tire Tester: main frame ①, measurement platform ②, plank ③.

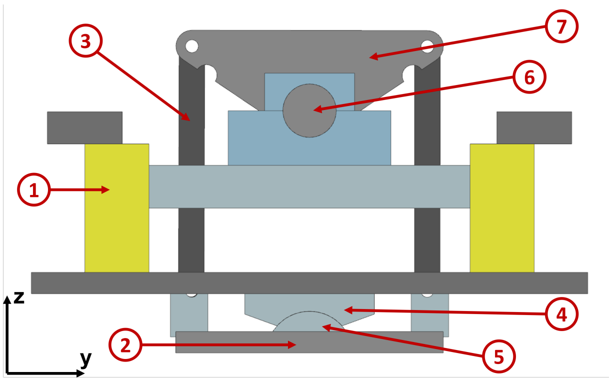

Figure 3.3: Cross-section, in the y-z plane, of the plank in non-cambered position: plank structure ①, road ②, connecting rod ③, rotation support ④, half-moon guide ⑤, camber rotation rod ⑥, and camber rotation triangle ⑦.

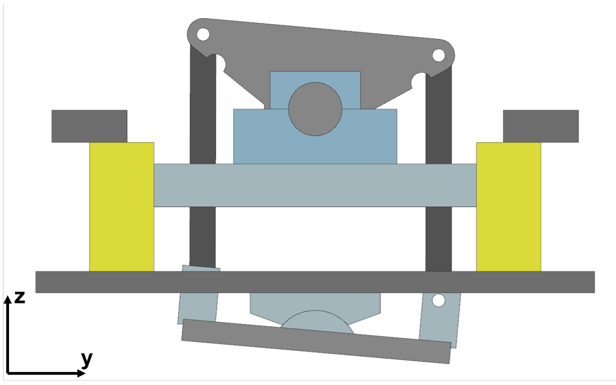

Figure 3.4: Cross-section, in the y-z plane, of the plank in a cambered position.

The main frame and plank have been shortened during this project, for it to physically fit in the basement of the renovated Automotive Technology (AT) Lab. This has reduced the total road length by 1.6 m, the road length is now equal to 4.22 m. The road plane was not fully covered in sandpaper in the past. This sandpaper has been replaced after the shortening of the machine, which increases the effective road length since the road plane has been fully covered in sandpaper.

Actuation of the Degrees of Freedom

The five degrees of freedom of the machine are actuated via electric motors. The actuation process of each degree of freedom is described below.

- The plank is translated in the x-direction by pinions that engage on gear racks on either side of the plank. The two pinions are mounted on a single shaft, which is connected to a worm gear reduction that is driven by an electric motor through a belt-pully arrangement. The speed and direction of the translation are selected via rotary switches on control box 1.
- The vertical position of the measurement platform is changed via two screw linear actuators, that are driven by an electric motor via a reduction gearbox and chain gear. The platform is lowered or raised via a rotary switch on control box 2.
- The road camber angle is governed via a linear actuator. The motor drives the planetary gear set, which in turn drives the ball screw linear actuator. The whole setup is mounted on the plank structure, and the output link of the linear actuator is connected with a radial offset to the rotation rod. As a result, a road camber angle is obtained by extending or retracting the linear actuator. The camber angle is set in the LabVIEW software, which is described in Section 3.2.
- The steering angle of the measurement hub is set by a worm drive, which is actuated by a motor via a belt drive and chain gear. The control buttons are located on the motor drive itself.
- The wheel rotation actuator controls the angular wheel position when the flexplates are connected, as explained in Section 2.2. The wheel rotation actuator is controlled via a MATLAB Simulink model running on a Speedgoat Real-Time Target Machine [17], which will be explained in Section 3.2. The wheel is rotated by the translation of the plank if the flexplates are disconnected and the wheel is in contact with the road.

Three degrees of freedom can be changed manually. The lateral position of the measurement hub with respect to the turntable is set by a handwheel. The rotation of the measurement hub to obtain a wheel camber angle is also done manually, as described in the manual of the machine [18]. It is also possible to set the steering angle via a handwheel. This is convenient as the protractor that indicates the steering angle is located on the same side as the handwheel, while the motor drive is positioned on the other side.

Data Acquisition

Various signals of the Flat Plank are measured during the operation of the machine. They are listed in Table 3.1 together with the corresponding measurement method. The signals that are measured using encoders are relative to the start of the measurement, since the encoders are of the relative type. The camber angle of the measurement hub is not actively measured, but has to be determined by the operator using an inclinometer. The steering angle is also readable from the protractor that is mounted on the turntable, which indicates the absolute steering angle in comparison to the relative steering angle measured by the encoder.

Table 3.1: Measured signals on the Flat Plank Tire Tester, with their corresponding measurement method.

Measured signals	**Measurement method**
Forces & moments	Strain gauges
Loaded wheel radius	Linear variable differential transformer (LVDT)
Road displacement & velocity	Rotary encoder
Road camber angle	Rotary encoder
Steering angle	Rotary encoder
Wheel angular rotation & velocity	Rotary encoder
Plank motion trigger	Photoelectric sensor

The output signals of the strain gauges are amplified by an Astech PIX amplifier since the strain gauges output several millivolts. This allows an analog-to-digital converter to transform analog signals into digital signals. The amplified strain gauge signals, together with the other measured signals, are supplied to a National Instruments (NI) data acquisition system. This system contains the analog-to-digital converter and provides an interface between the measured signals and the data-logging PC. The plank motion trigger sends a signal to the data-logging software to start logging when a metal strip, which is mounted on the plank, passes the sensor. In this way, the measurements start at the same road displacement.

In this project, the Speedgoat has been upgraded to allow the input of analog and digital signals, since it is desired to move the data logging to this machine. The IO317 [19] and IO132 [20] input/output (IO) modules have been installed, where the former provides digital IO connectivity and the latter analog inputs and outputs. Additionally, adaptations have been made to the measurement cables to allow the logging of the signals on both the data-logging PC and the Speedgoat.

Hardware Issues

A number of hardware issues have been identified during the measurements performed in this research or in the previous research of van Blijderveen [2]. Additionally, some problems surfaced when attempting to explain certain measurement results during the post-processing of the measurement data. The following list summarizes the known hardware issues of the Flat Plank.

1. The five electrically actuated degrees of freedom are actuated using different brands of electric motors, communication protocols, and types of feedback. This significantly complicates the operation of the machine, because a unified approach to control these five degrees of freedom is not available.
2. An issue with the different control methods for the degrees of freedom is the difficulty of synchronously starting the road displacement and wheel rotation. As a result, the operator has to toggle the switch for the road displacement just after setting the rotational velocity and effectively trying to account for varying actuation time delays. This leads to a force step with varying amplitude, which has to be sufficiently small for the tire to reach free-rolling conditions before a slip step is introduced [2].
3. An air spring system is present to obtain a constant vertical force instead of a fixed axle height. However, this system does not function anymore and has been partially removed, eliminating the possibility of performing measurements with a constant vertical force.
4. The plank displacement and wheel rotation encoders produce low-quality signals compared to the encoder signals of the Stöber servomotor. These encoders have 20000 pulses per rotation, while the encoder of the servomotor has 8.3 million positions. The relatively low number of positions is presumably the cause of the low-quality signal. Additionally, the mechanical connection between the wheel encoder shaft and the measurement hub shaft is possibly inadequate, since it is uncertain whether the wheel encoder shaft is rigidly connected to the measurement hub shaft.
5. The logged road velocity is not truly the translational road velocity. It is actually the rotational velocity of the pinion gear multiplied by its pitch radius to obtain a translational velocity. This means that the speed variations due to gear meshing between the rack and the pinion are not accounted for. This includes speed fluctuations caused by wear, misalignment, and trapped tire debris. It is unknown to what amplitude the measured speed variations of the pinion gear are transmitted to the translational velocity of the plank.
6. The analog output signals of the strain gauges and LVDT are transmitted via cables to the data acquisition hardware that are approximately 12 m long. The cables are routed through a cable duct in which the power cables for the motors are placed as well. As a result, the power cables introduce a significant amount of noise into the measured analog signals.
7. It is not possible to log the encoder signals in both the LabVIEW and the Simulink software simultaneously. Additionally, the road camber angle and steering angle encoders are not connected to the Speedgoat.
8. The plank was shortened on one side by grinding through the road surface and the plank structure. As a result, one of the bearings that constrain the road surface in the x-direction with respect to the plank structure was also removed and not reinstalled. This results in a play of approximately 1.15 mm in the x-direction.
9. The connecting rods are adjustable in length to eliminate play between the rotation support and the half-moon guide. However, the connecting rods have been extended in the past for unknown reasons. This introduced a play of approximately 3 mm in the y-direction and 1.3 mm in the z-direction between the half-moon guide and the rotation support.
10. There is a free play of approximately 0.2° between the worm screw and worm gear of the steering mechanism of the measurement hub. As a result, the tire can steer during measurements, even though a fixed steering angle of 0° is set. This leads to the tire generating a small lateral force. Additionally, the steering angle encoder measures the angle of the worm screw that is converted to the steering angle of the measurement hub. Thus, the play in steering angle is not measured.
11. The plank is not consistently guided in the lateral direction by each ball bearing, due to poor alignment of the bearings. As a result, the uneven meshing of the rack-and-pinion gear on both sides of the road leads to lateral movement of the plank throughout the longitudinal motion of the plank. Similarly, the plank is not equally supported by the ball bearings in the vertical direction. The plank seems to undulate over and fall off of bearings, which presumably leads to variations in the vertical tire force.
12. A weld between the input shaft of the rack-and-pinion gears and the output shaft of the worm gear reduction was torn during a measurement, shortly after the last measurements for this project had been

performed. The crack in the weld slowly evolved over time, presumably due to the increased strain introduced by the measurements in recent longitudinal slip actuation projects.
13. The sandpaper used on the road quickly wears when a significant amount of measurements are performed, especially during pure or combined slip. The sandpaper has been replaced at the start of this project, as suggested by Van Blijderveen [2]. The new type of sandpaper proved inadequate for the application as it wore rapidly. Subsequently 3M Safety-Walk [21] has been applied, since better longevity has been experienced in the past. Nevertheless, this high-quality material still wears relatively quickly, meaning that sandpaper does not seem a durable option.
14. A flexplate drum, used to transmit torque from the wheel rotation actuator to the measurement shaft, aims to transmit a pure torque. With the currently used short drum, only partial decoupling of the parasitic forces from the measurement is achieved [2]. The drum radially preloads the measurement shaft, leading to sinusoidal longitudinal and vertical parasitic forces with an amplitude of approximately 200 N.
15. Different types of adapters are available to allow different types of rims to be mounted on the measurement hub. It is crucial that the adapter, and therefore the wheel, is sufficiently concentric with the measurement hub. Otherwise, the tire has a radial runout leading to a varying vertical force due to the fixed axle height during a measurement. The concentricity is achieved by using a sliding fit between the measurement hub and the adapter. However, some adapters have a too loose fit, meaning that it is challenging to concentrically mount the adapter.
16. The road hits the rack-and-pinion drive shaft when the road camber actuator is homed, which results in damage to the road. The camber actuator homing procedure extends the linear actuator to one side until the limit switch on that side is reached. It turns out that the limit switch position has been changed for unknown reasons, leading to the linear actuator extending too far.
17. The position of the servomotor of the wheel rotation actuator is suboptimal in terms of ease of operation. The servomotor hits the pillar when a steering angle larger than 48° is desired. This means that the operator has to move the measurement hub laterally inward to ensure the servomotor does not hit the pillar. The reduction gearbox of the wheel rotation actuator is of inferior quality with regard to backlash and efficiency [2].
18. The output of the LVDT is converted to the loaded wheel radius of the tire. The relation between the output voltage and the radius is linear, but it is unknown whether the currently used coefficients are still correct.
19. The measurement hub has been calibrated in 2008 for the last time and it is unknown if the calibration parameters are still valid.
20. The wheel rotation actuator is not implemented in the existing safety circuit of the Flat Plank. This means that the wheel rotation actuator will keep rotating the wheel when the emergency button is pressed, while motions of the other electrically actuated degrees of freedom are safely stopped.

Solutions

The proposed solutions to the aforementioned hardware issues are given in the list below. Some of these solutions have already been implemented, but only after the measurements for this project have been performed. The solution number corresponds to the issue number, listed in the previous section.

1. Throughout this project, meetings have been held together with the Automotive Technology Lab personnel and the Equipment and Prototype Center (EPC) [22] to replace the existing, outdated electric motors with Stöber-brand servomotors. This allows actuating of all degrees of freedom in a similar fashion as the rotation of the wheel. Unfortunately, the lead times of the servomotors and especially their corresponding motor drives are excessive due to the global chip shortage. This means that these motors are not yet installed before finishing this project. It might be possible to integrate the current motor drives in the Speedgoat software as a temporary solution.
2. The issue of asynchronous starting of the road displacement and wheel rotation is resolved by supplying the plank encoder signal to the Speedgoat. This allows enabling the wheel rotation actuator once the plank starts moving. This feature is implemented in the new software, which is explained in more detail in Chapter 4.
3. A more constant vertical force may be achieved once the current motors are integrated into the Speedgoat software or are replaced with Stöber-brand ones. A controller can be designed that varies the axle height to maintain the reference vertical tire force.
4. The encoders should be replaced by state-of-the-art versions with more pulses per rotation, preferably using the EnDat communication interface that the servomotor also employs [23, 24]. Furthermore, the current mounting of the encoders should be reviewed and improved if deemed necessary.

5. The translational road velocity should be measured more accurately, which can be achieved by either a linear or rotary encoder. A linear encoder appears to be the best option, but might not be applicable due to the lateral movement of the plank. It is suggested to use a small wheel, which does not slip. It can be mounted on a rotary encoder and rolls over the same face as the ball bearings.
6. The power and measurement cables have been rerouted to reduce the amount of noise induced by the power cables. In the future, the power supply to all motors and the measurement equipment will be completely separated into two cabinets to further reduce the noise injection once the current motors are replaced by Stöber versions.
7. The LabVIEW software becomes obsolete once all motors can be controlled via the Simulink software, which eliminates the need for simultaneously logging encoder signals.
8. EPC has fabricated a part that is mounted onto the plank structure and constrains the road in the longitudinal x-direction again. A play of 0.1 mm is kept to allow the road to be cambered without too much friction.
9. EPC has readjusted the connecting rods to eliminate the play between the rotation support and the half-moon guide.
10. The steering angle encoder should directly measure the steering angle of the measurement hub rather than the worm screw angle. This allows to actively control the steering angle of the hub in the Simulink software, once the motors have been replaced.
11. The plank-supporting ball bearings have been cleaned, reinstalled, and adjusted to allow a play of 0.1 mm between the ball bearings and plank structure. However, it proved to be challenging to properly align the bearings, which means that lateral movements and undulations of the plank are still present. To properly align the bearings, the main frame should first be set level with the plank removed from the frame. Thereafter, the bearings that vertically support the plank should be set level with respect to each other. Lastly, the plank can be reinstalled and the lateral guiding bearings can be adjusted to allow a play of 0.1 mm.
12. EPC manufactured a new axle with a keyway to drive the rack-and-pinion gear as a repair to the sheared-off weld.
13. The sandpaper can be fairly easily replaced, but a more permanent and durable solution is desired. A possible solution is to mechanically roughen a metal sheet, to obtain the same friction level as typical road friction, and mount it on the machine. Another solution is bonding an aggregate, such as bauxite, to the road surface using a resin binder. This technique, called high friction surface treatment, is widely applied in highway engineering to increase road friction [25]. Further research is required to explore the possibilities and make a substantiated decision.
14. Van Blijderveen [2] suggests replacing the flexplate drum with a longer version to decrease the preloading of the measurement shaft. Additionally, he advises remanufacturing the end shaft piece from scratch to obtain proper concentricity with the measurement shaft. This suggestion is still valid and encouraged, but does not have priority in this research. The logging of data using a Simulink model allows the implementation of parasitic force filter as a function of the angular wheel position. This will be explained in more detail in Chapter 4.
15. The adapters that do not have a sliding fit with the measurement hub should be replaced to ensure the concentricity of the adapter with the measurement hub. Additionally, it should be ensured that newly designed adapters are manufactured in such a way that they have a sliding fit with the measurement hub.
16. The issue of homing the camber actuator, where the road hits the drive shaft, has been resolved by repositioning the limit switch.
17. Van Blijderveen proposes to reposition the motor and replace the cheap reduction gearbox with a higher-quality servo reducer. The proposal is described in [2, Appendix B].
18. The LVDT should be calibrated, which can be achieved using a ruler to measure the distance from the measurement shaft center to the road.
19. The measurement hub should be recalibrated.
20. In the new software, the wheel rotation actuator will be enabled if the plank is moving. The wheel rotation actuator will thus be disabled when the emergency button is pressed since the plank stops moving. This is a short-term solution. In the long term, a new safety circuit will be realized together with the implementation of the Stöber-brand servomotors. Controlling all degrees of freedom using the newly developed software allows creating software-based safety features. For example, it is possible to define the maximum road displacement of the machine using the plank displacement encoder and stop the plank movement once this software-based limit is reached. The mechanical limit switches provide backup in case the software-based limit switch fails.

3.2 Software

The following two subsections describe the software that is used for data logging and control of the road camber angle and wheel rotation actuator. Then, the software issues and corresponding solutions are listed.

LabVIEW

A Graphical User Interface (GUI) has been designed in LabVIEW [26] and is used to log the measurement data and control the camber actuator. The GUI has been developed over time, e.g., road camber control has been added. The most recent version contains three tabs. The first tab contains the settings of the data acquisition software, where parameters such as sampling frequency, ET-value of the mounted rim, and storage location & file name are entered. Additionally, the loaded wheel radius and the longitudinal, lateral, and vertical force are displayed numerically. The second tab visualizes all measured signals, as listed in Table 3.1, in multiple plots. The third tab allows setting the camber angle of the road to a sinusoidal or triangular profile of desired frequency, amplitude, and offset. Additionally, the plank can be homed to reinitialize the zero position of the actuator. The desired motion profile and corresponding parameters are sent to the motor drive of the camber actuator via the RS232 protocol, whereafter the software that is embedded in the motor drive controls the camber motion.

The amplified strain gauge outputs are converted to log and visualize the measured forces and moments in the LabVIEW software. This conversion is explained in more detail in Appendix A. The loaded wheel radius is determined from the output of the LVDT. The encoder data is converted from pulses to angles using the number of pulses per rotation of the corresponding encoder. This results in the camber, steering, and wheel angle, and wheel velocity. The output of the plank position encoder is multiplied by the pitch radius to obtain the translational position and velocity of the plank. The logged data can be saved to a text file once a measurement is finished.

MATLAB Simulink

The wheel rotation actuator is controlled via MATLAB Simulink software, which runs on the Speedgoat Real-Time Target. A Simulink model is developed during the project of Van Blijderveen [2] and consists of a GUI and a subsystem, which contains the underlying control structure. The operator has to compile the model on the Host PC and deploy it to the Speedgoat for each measurement. The GUI allows changing parameters of the actuator, which are enabling or disabling the wheel rotation servomotor, selecting the operation mode, setting the amplitude, frequency, and offset of the reference profile, and starting and stopping the reference profile. The operation modes are speed or torque control, thus the servomotor tracks a reference speed or torque, respectively. The possible reference profiles for speed control are a constant value, a sinusoidal waveform, or a triangular waveform. The GUI visualizes the torque percentage and the reference and actual rotational motor velocity. The subsystem consists of the control structure to communicate with the Stöber motor drive via the EtherCAT protocol [27], together with the functions to generate the desired reference profile based on the settings in the GUI.

Various signals of the wheel rotation actuator are logged, such as the elapsed time and the actual and reference velocity and torque. These signals are sent to the MATLAB workspace of the Host PC once the model running on the Speedgoat is terminated. Subsequently, the operator can manually save the workspace if desired. The data logging using MATLAB is completely separate from the LabVIEW software without any means of synchronization between the two datasets.

Software Issues

The following list summarizes the software issues of the current setup.

- There is little knowledge of the LabVIEW software among the lab personnel and students. Additionally, the software has been adapted over the years without documentation and contains various obsolete functions.
- It is challenging to perform longitudinal slip measurements with the current user interface, actuator control, and data recording distributed over two unsynchronized devices. It is not possible to synchronize the two software programs during a measurement. This presents challenges during data processing if signals of both datasets have to be compared.
- The execution of the Simulink model on the Speedgoat has to be terminated after each measurement to obtain the logged signals of that measurement. This means that the model has to be compiled and deployed to the Speedgoat for each measurement, which takes up to 2 minutes per measurement. This

significantly increases the time required to perform a measurement, since a measurement typically takes 5 minutes.
- It is not possible to control the wheel speed to compensate for anomalies in the plank speed since this signal is not available in the Simulink software [2].

Solutions

These issues described above are resolved by the newly developed MATLAB Simulink software for the Speedgoat, which is explained in Chapter 4. MATLAB Simulink is known by university students and personnel, and the software has a helpful online community and extensive technical support. The issue of re-compiling and re-deploying of the Simulink model for each measurement is resolved by developing a GUI for the Host PC which communicates with a dedicated model running on the Speedgoat. The separate GUI allows the extraction of measurement data from the Speedgoat without terminating the model. Changes to the software and their motivation should be thoroughly kept track of, which can be simplified by using the GitLab platform. The LabVIEW software will become obsolete once all motors are replaced by Stöber versions, which will be controlled via the Speedgoat machine. However, this replacement has not yet been realized

The newly developed software improves the data logging and actuator control, however, some issues and limitations remain and are listed in Section 4.3.

3.3 Summary

This chapter describes the current layout, actuation of degrees of freedom, and data logging methods of the Flat Plank in terms of software and hardware. The software and hardware issues of the machine are listed to combine all known problems in a single chapter, which is useful for future reference. Many hardware issues have been resolved, which means that the quality of the measurement data has improved, while some problems remain to be solved in the future.

Chapter 4

Software Design

The implementation of the wheel rotation actuator on the Flat Plank has shown the potential of the Speedgoat Real-Time Target Machine in combination with a Stöber servomotor. The current software issues illustrate that the existing software setup of the machine fails to provide a single, comprehensible GUI to log measurement data and control the electrically actuated degrees of freedom of the machine. Therefore, it is desired to create software for the Speedgoat that is able to log data, control the actuators, and implement safety features.

This chapter describes the developed software using MATLAB Simulink. Firstly, the objectives and requirements of the software are defined, which are needed to develop suitable software. Subsequently, the structure of the software is explained, followed by the issues, limitations, and future improvements.

4.1 Objectives and Requirements

The main objective of the software is to combine the data logging, actuator control, and user interface into the Speedgoat. The goal is to control the Flat Plank and log measurement data via a comprehensible GUI on the Host PC that communicates with the control model on the Speedgoat. The Stöber motor drive and the measuring equipment are connected to the Speedgoat, as illustrated in Figure 3.1. Thus, the Host PC provides an interface between the operator and the Flat Plank via the Speedgoat. Several objectives originate from the operating procedure of the Flat Plank. Therefore, the operating procedure is explained, whereafter the requirements are listed.

Flat Plank Operating Procedure

It is possible to mount different types of wheels onto the Flat Plank using the corresponding adapter, where each rim has a certain ET value. The ET value and adapter thickness influence the calculation of the forces and moments at the tire-road contact point. Therefore, it must be possible to change these values. The wheel camber angle, road camber angle offset, and steering angle offset are not measured by the machine and must be provided to the data-logging software. EtherCAT provides the communication between the Speedgoat and the Stöber drive and requires an EtherCAT Network Information (ENI) file. This file describes the components of the network structure, such as the slave configuration of the network.

The measurement procedure starts with setting the measurement conditions, such as the steering angle or the tire inflation pressure. Subsequently, the operator changes the axle height to obtain the desired vertical force, whereafter the data logging is started. The measurement starts by initiating the road displacement and ends when the operator stops the road displacement or the plank reaches the maximum displacement. The data logging is ended and the data is saved, if desired. It is convenient for the operator to numerically see the measured signals, especially when vertically loading the tire. Additionally, plotting the forces and moments against time or road displacement allows the operator to verify the measurement results. For example, whether the tire has reached steady-state conditions and the measurement can be terminated.

The flexplate drum radially preloads the measurement shaft leading to sinusoidal parasitic signals, which are dependent on the angular position of the tire. It is possible to reduce their influence by implementing parasitic signal filtering, which removes the sinusoidal disturbances from the measurement results. For that reason, it is favorable to provide the functionality to identify the parasitic signals and filter these out if desired. The filtering procedure is explained in more detail in Appendix C. The result of this filtering is shown in Figure 4.1, where it is seen that the amplitude can be significantly reduced from 300 N to 15 N.

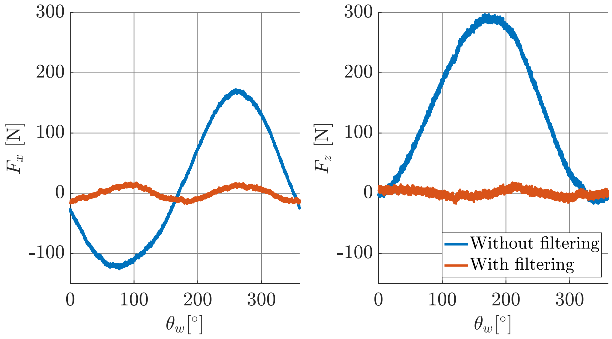

Figure 4.1: The effect of the parasitic signal filtering on the longitudinal tire force F_x and vertical tire force F_z for different wheel rotation angles θ_w.

The wheel rotation actuator introduces the possibility to subject the tire to a longitudinal slip. The main issue is that it is challenging to actuate the tire rotation and road displacement synchronously. Therefore, the tire rotation must be enabled at the same time as the plank starts moving. The Stöber servomotor can track a reference position, velocity, or torque profile. The position profile is required for parasitic signal identification and is convenient for positioning the tire to the correct starting rotation. The velocity profile is required for the longitudinal slip measurements since the desired slip value is obtained by regulating the rotational velocity of the wheel. The free-rolling controller is used to determine the effective rolling radius of a tire and is explained in Chapter 5. This controller outputs the reference torque that the servomotor has to track, meaning that the torque profile must be implemented as well. As a result, six operation modes are desired that utilize one of the aforementioned profiles and are explained below.

Longitudinal slip control	Longitudinal slip control must enable the operator to subject the tire to a longitudinal slip waveform by selecting the desired waveform and its parameters. The currently desired waveforms are constant, step, double step, sine, or triangle. It must be relatively simple to add other waveforms. The reference wheel rotational velocity has to be calculated based on the provided effective rolling radius, the road velocity, and the selected waveform and parameters.
Wheel position control	The wheel position control operation mode has to allow the specification of the desired angular position of the wheel, whereafter the internal control structure of the servomotor rotates the wheel with a constant velocity to that position. Additionally, it is convenient to send the tire to a predetermined position, which is equal to 0°, 120°, 240°, 360°, or 1080°. 1080° is required to determine the parasitic signals, as is explained in Appendix C.
Velocity control	The operator can specify the wheel rotational velocity after which the servomotor tracks this velocity. A possible application of this mode is to measure the radial runout of the adapter using a dial gauge while the wheel rotates at a constant velocity and verify whether the adapter is mounted concentrically.
Torque control	The servomotor tracks the reference torque, which is provided by the operator. This operation mode has been used for testing purposes during the design of the free-rolling controller.
Free-rolling	Free-rolling implements the free-rolling controller, which provides a reference torque to regulate the generated longitudinal tire force.
Homing	The Stöber servomotor contains a built-in absolute encoder, which measures the position, velocity, and acceleration of the output axle. The internal control structure of the Stöber drive software uses this position to rotate the wheel to the desired angular position when using the wheel position control mode. The Stöber software allows redefining the 0° rotation, which might be desired during measurements. Therefore, the homing operation mode must provide a method to define the current angular wheel position as the 0° rotation in the Stöber drive software.

It is desired to log the reference and actual position, velocity, and torque of the servomotor. The Stöber drive requires certain steps to be taken before the servomotor is enabled and usable for measurements. These steps are defined in the Stöber operation manual and have to be implemented to allow the operator to enable and disable the servomotor, send reference profiles, and retrieve the actual signals.

Requirements

Several requirements arise from these objectives that determine the design of the software. The requirements consist of general requirements for both the GUI and control model and high-level requirements for each. The specific requirements have an R1 and R2 prefix for the GUI and control model, respectively.

In general, it must be simple to apply modifications and implement additions to the GUI and control model for future enhancements and extensions. Furthermore, the control interface and structure for the Stöber servomotor of the wheel rotation actuator have to provide a foundation for the other Stöber servomotors that will be implemented in the future. This means that the overall control structure has to be applicable to each servomotor and only specific operation modes have to be created for each servomotor.

Specifically, the GUI must be able to:

R1.I connect with the Speedgoat, deploy a control model, and execute it,
R1.II start and stop the logging of data,
R1.III save the logged data with the desired name at the desired file location,
R1.IV display the measured signals, listed in Table 3.1, numerically,
R1.V show the measured forces and moments in time plots,
R1.VI change constants for the specific measurement conditions, such as the ET-value,
R1.VII enable and disable the wheel rotation actuator,
R1.VIII select the operation mode of the wheel rotation actuator and specify the corresponding parameters of each mode,
R1.IX display reference and actual signals of the wheel rotation actuator,
R1.X display the EtherCAT network status,
R1.XI load the required measurement data for the parasitic signal filtering,
R1.XII enable and disable the parasitic signal filtering.

The Simulink control model has to be able to

R2.I import the measured analog and digital data of the Flat Plank that are supplied via the IO modules,
R2.II establish the EtherCAT communication network,
R2.III implement the constant inputs corresponding to R1.VI,
R2.IV compute the forces and moments based on the strain gauge outputs according to Appendix A,
R2.V determine the loaded wheel radius using the axle height LVDT output,
R2.VI convert the output of the encoders using the corresponding number of pulses per rotation,
R2.VII log the desired data,
R2.VIII actuate the wheel rotation actuator once the plank starts moving,
R2.IX provide the required control and communication structure for the Stöber motor drive,
R2.X implement the six operation modes of the wheel rotation actuator, specified on page 16,
R2.XI calculate the reference signals based on the selected operation mode and the specified parameters,
R2.XII supply the reference signal to the Stöber motor drive and obtain the actual signals,
R2.XIII implement the parasitic signal filtering based on the wheel angular position.

There are some nice-to-have functionalities in addition to these requirements. These functionalities are not necessary for the software to function properly, but are convenient for the operator. The functionalities have an N prefix and are listed below.

N.I Typically, a measurement is repeated three times at a wheel starting angle of 0°, 120°, and 240°. The wheel rotation actuator controls the angular position of the wheel, meaning that the operator cannot manually rotate the wheel to the desired starting position. The parasitic force identification procedure requires the tire to rotate three full revolutions. Therefore, it would be convenient to allow the operator to select a starting position to which the wheel will be rotated.
N.II It is helpful to plot the measured forces and moments against road displacement. In this way, the operator can directly see at what plank displacement a remarkable event, which might need further investigation, occurs.

4.2 Software Design

The objectives and requirements are used to design the GUI and Simulink control model. Satisfying the requirements should result in a GUI and control model that allows the operator to log measurement data and control the wheel rotation actuator in a comprehensible manner. Additionally, the nice-to-have functionalities will provide convenient tools to support the operator in performing measurements.

MATLAB App Designer is used to create the GUI, which allows creating and modifying the GUI via a drag-and-drop approach of visual components, such as buttons, edit fields, and plots. The App Designer software automatically generates the code to create the visual component and provides callback function templates to call the code that should be executed when the visual component is toggled by the operator. The control model is designed in Simulink, which is a graphic block-oriented programming tool. Both environments inherently allow for easy implementation of changes. The Simulink control model of Van Blijderveen [2] is created in MATLAB R2020b, but the R2022a version provides more functionalities for MATLAB App Designer in conjunction with the Speedgoat functions. Therefore, the Host PC and Speedgoat have been updated to MATLAB R2022a Update 2.

The following two subsections describe the high-level design of the GUI and control model, which have been created from scratch and developed during this project. The development process starts with an investigation of the existing LabVIEW and Simulink software to understand the current approach for data logging and actuator control. Thereafter, a basic GUI and control model have been created where only a few basic functions are implemented. Subsequently, the software is expanded through testing and implementing functionalities, ultimately leading to the current version of the software that is described in this chapter. A short review, followed by the prospects of the software, is provided after the high-level design explanation.

GUI

The GUI is visualized in Figure 4.2, where it can be seen that it consists of two major segments. The first segment is the main ribbon, which is located at the top and is always visible to the operator. The second segment contains four control tabs, where only the content of the selected tab is visible. In the figure, the `Visualization` tab is selected.

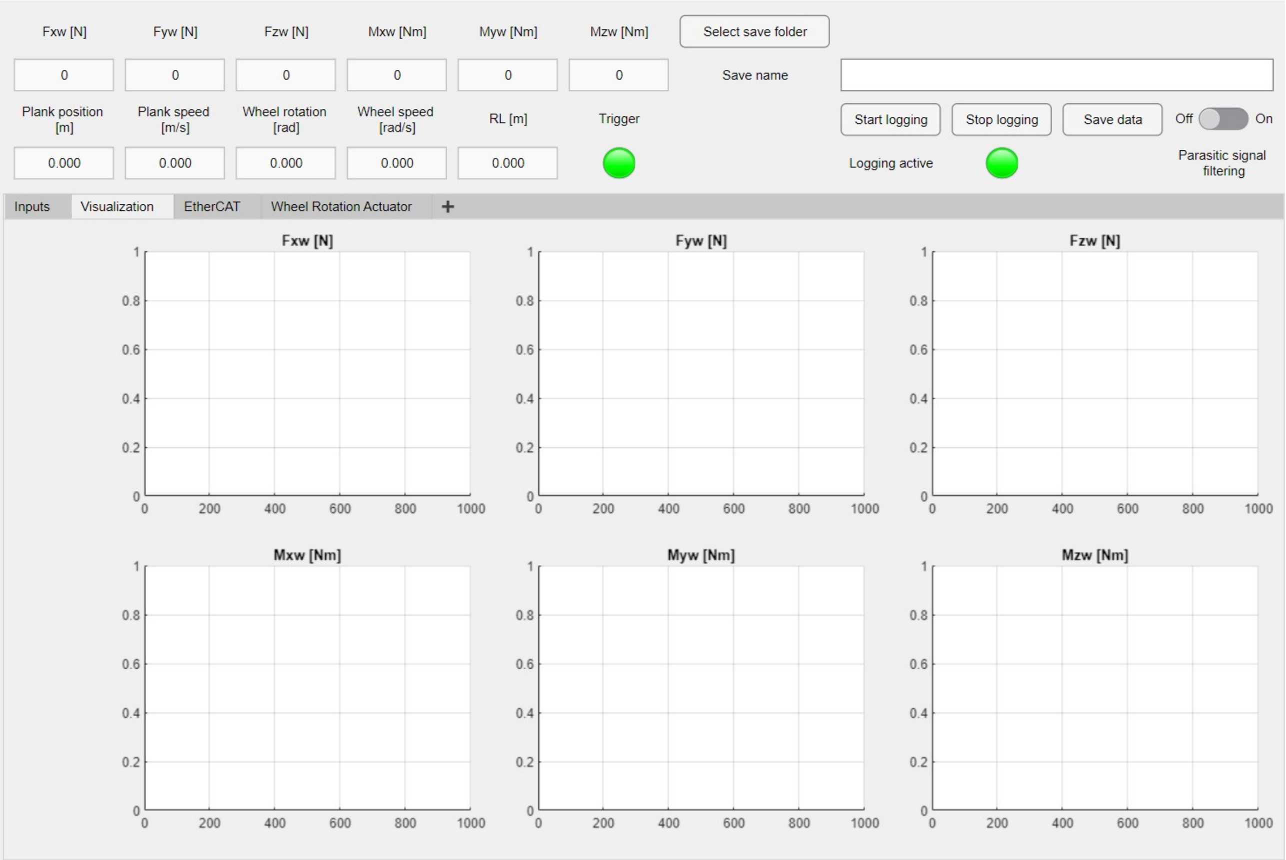

Fxw [N] 0
Fyw [N] 0
Fzw [N] 0
Mxw [Nm] 0
Myw [Nm] 0
Mzw [Nm] 0
Plank position [m] 0.000
Plank speed [m/s] 0.000
Wheel rotation [rad] 0.000
Wheel speed [rad/s] 0.000
RL [m] 0.000
Parasitic signal filtering Off

Figure 4.2: Screenshot of the GUI, which consists of the main ribbon and the control tabs, where the `Visualization` tab is selected.

The main ribbon displays the measured signals numerically and provides edit fields and buttons for the data logging and saving capabilities. Additionally, the ribbon contains an indicator light to show the operator whether the plank motion trigger has been activated and whether the data logging is active. A switch is used to enable and disable parasitic signal filtering.

The control tab segment is located below the main ribbon and contains four tabs. The first tab, `Inputs`, contains buttons to connect with the Speedgoat, deploy the control model, and start or stop the execution of the model. The operator can also input the constants, e.g. the ET-value of the rim, in numerical edit fields. Additionally, a button provides the option to load the required measurement data for parasitic signal filtering. This tab is visualized in Figure B.1. The `Visualization` tab contains six figures to plot the measured wheel forces and moments. The third tab shows the EtherCAT network status and is depicted in Figure B.3. The `Wheel Rotation Actuator` tab is shown in Figure 4.3, and consists of multiple panels. The operator can enable and disable the servomotor in the `Drive Status` panel and an indicator light shows whether the servomotor is in an error state. The operator selects the desired operation mode in the `Operation Mode` panel. This enables the corresponding panel, while the other operation mode panels are disabled. Each operation mode panel provides the required inputs for the control model to generate the reference signal for the Stöber drive to track. The `Longitudinal Slip Control` panel provides four subpanels for the waveform input, where the corresponding subpanel is enabled based on the waveform choice. Additionally, two edit fields for the operator are available to input the effective rolling radius and the start distance where the waveform needs to be subjected to the tire.

Fxw [N]: 0
Fyw [N]: 0
Fzw [N]: 0
Mxw [Nm]: 0
Myw [Nm]: 0
Mzw [Nm]: 0
Save name:
Plank position [m]: 0.000
Plank speed [m/s]: 0.000
Wheel rotation [rad]: 0.000
Wheel speed [rad/s]: 0.000
RL [m]: 0.000

Operation mode:
- ● No mode
- ○ Free Rolling
- ○ Longitudinal Slip Control
- ○ Homing
- ○ Wheel Position Control
- ○ Velocity Control
- ○ Torque Control

Waveform choice:
- ● No mode
- ○ Sine
- ○ Constant
- ○ Triangle
- ○ Step
- ○ Double Step

Effective rolling radius [m]: 0
Start distance [m]: 1.5
Longitudinal slip [-: 0
Slip step value [-]: 0
Frequency for sine: 0
Velocity for triangle [1/s]: 0
Amplitude [-]: 0
Number of periods ([0 inf]): 0
Direction (0 is positive, 1 is: 0
Slip step value 1 [-]: 0
Start distance 1 [m]: 1.5
Slip step value 2 [-]: 0
Start distance 2 [m]: 2.5
Target position [deg]: 0
Actual position [deg]:
Target velocity [RPM]: 0
Actual velocity [RPM]:
Effective rolling radius [m]:
Actual torque [Nm]:
Target torque [Nm]: 0

Figure 4.3: Screenshot of the `Wheel Rotation Actuator` tab of the GUI.

The MATLAB GUI is the front-end GUI, whereas the MATLAB code linked to the components composes the back end. When the operator, e.g, clicks on a button or edits text or numbers in edit fields, the code linked to that specific component is executed, which effectively means that the changes are applied to the control model. In other words, the back end provides the interface between the visual GUI components and the underlying control model. The back-end structure is not discussed, but can be found in the software manual of the Flat Plank.

Control Model

The control model layout is visualized in Figure 4.4. The model consists of seven subsystems, which output one or more bus signals and may have one or more bus inputs. A bus signal allows all signals within a subsystem to be outputted as one combined signal. This reduces line complexity and clutter, together with the easy addition and removal of signals. The subsystems are explained below.

User input	This subsystem obtains the constant inputs that the operator enters in the `Inputs` tab of the GUI and combines them into one bus signal.
Measured data acquisition	The `Measured data acquisition` subsystem contains two underlying subsystems for the acquisition of analog and digital measurement data. The `Analog measurements` and `Digital measurements` subsystems contain the configuration and import blocks for the Speedgoat IO132 and IO317 modules, respectively. Additionally, the `Analog measurements` subsystem implements parasitic signal filtering.
Measurement hub	The obtained analog data is converted to forces and moments at the wheel center and at the tire-road contact point in the `Measurement hub` subsystem, according to the calculations given in Appendix A. Furthermore, the loaded wheel radius is calculated, the digital encoder data is converted to obtain the road and wheel position and velocity, and it is determined whether the plank motion trigger has been activated.
EtherCAT	The `EtherCAT` subsystem provides the configuration block of the EtherCAT Master. The configuration block enables the control model to communicate with the Stöber drive via dedicated process data object (PDO) blocks. These blocks can receive and transmit data over the EtherCAT network.
Actuators	This subsystem provides the implementation of the wheel rotation actuator in the `Wheel Rotation Actuator` subsystem, which consists of two finite state machines. One state machine provides the necessary communication with the Stöber drive to enable the servomotor. The second state machine implements the calculation of the reference signals for the Stöber drive, based on the chosen operation mode with the corresponding parameters. The reference signal is sent to the Stöber drive once the plank starts moving, which is determined using the plank displacement encoder data.
Heartbeat	A periodically updated heartbeat signal is used to verify whether the GUI on the Host PC is still functioning normally. If the GUI freezes or fails otherwise, the heartbeat can be used to safely stop the measurement.
Datalogging	The `Data logging` subsystem combines all buses into one master bus, which is provided to the `File Log` block in Simulink. This block sends the master bus data to the Host PC once the operator stops the logging of data, after which it can be saved via the GUI.

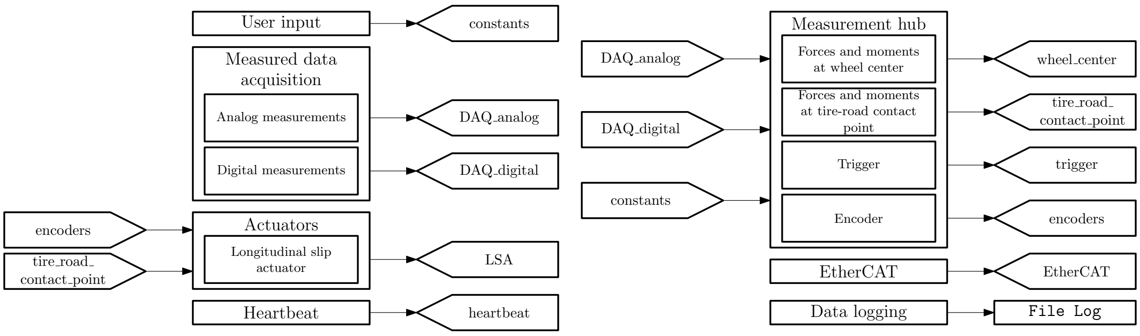

Figure 4.4: Layout of the control model of the Speedgoat.

Review & Prospects

The software described provides almost the same functionalities as the two separate, non-synchronized software systems that have been used in the past. Only control of the road camber angle and the logging of the road camber and steering angle are not yet possible. Unfortunately, the current MATLAB version only allows time as the x-variable of an axis, which means that N.II cannot be implemented. Beyond these missing functions, the GUI and control model fulfill the requirements and provide the operator with a clear and understandable approach for data logging and actuator control.

An important contribution of this software is the parasitic force filter, which reduces the influence of the preloading of the measurement shaft and improves the accuracy of the measurement results. The results are also improved in terms of sampling frequency and noise compared to the existing LabVIEW software. Performing longitudinal slip measurements is significantly improved due to the automatic actuation of the wheel rotation actuator, together with the wheel rotation actuator reference signals being road displacement dependent. Once the road displacement is initiated by the operator, the control model provides a reference rotational velocity of the wheel to subject the tire to the desired longitudinal slip value. As a result, the operator only has to supply the effective rolling radius and the desired operation mode and parameters instead of manually calculating the reference rotation velocity and separately initiating the wheel rotation and road displacement. The road displacement dependency allows starting of the reference waveform at a certain displacement. In this way, the start of the waveform is synchronized between different measurements, which simplifies the data processing. The implementation of the free-rolling controller, which will be explained in Chapter 5, allows performing a free-rolling measurement to obtain the required data to determine the effective rolling radius of the tire for the desired operating conditions. This simplifies the identification of the effective rolling radius compared to the approach used by Van Blijderveen [2]. Lastly, the predetermined position buttons provide the operator with a convenient solution for rotating the tire to the desired angular position.

The design of the GUI and control model allows expansion and adaptation of the software. Extra tabs can be added to the control tabs segment to control additional motors that will be implemented, visually separating the actuation of degrees of freedom without cluttering the existing tabs. The panel implementation of the operation modes and waveforms in the GUI can be extended to realize more modes and waveforms. The subsystem layout of the control model structures the implemented functions, and new functions can be added to the respective subsystems. The control interface and structure for the existing Stöber drive provide a foundation for the new Stöber servomotors that will replace the outdated motors. Additionally, the finite state diagram that implements the operation mode and waveform generation can be extended to add new modes or reference waveforms, corresponding to the additions in the GUI.

The software also allows the implementation of safety systems. For example, it is possible to implement a safety feature that ensures that the wheel can only be rotated by the wheel rotation actuator if the loaded wheel radius is larger than the free radius of the tire and the vertical force is in the vicinity of 0 N. The free radius is calculated based on the tire dimensions, which the operator has to supply. This eliminates the possibility of rotating the tire while it is in contact with the stationary road, so the tire and sandpaper do not needlessly wear.

4.3 Issues, Limitations and Solutions

The most important limitation is the manual actuation of the road displacement and vertical axle position by the operator instead of actuation via software using the Speedgoat. The wheel is actuated based on the encoder signal, but there is an actuation delay in the wheel rotation once the road displacement has been actuated by the operator. Presumably, the delay is a combination of the measurement delay of the encoder and the software implementation that decides whether the road motion has started. As a result, the tire generates a significant negative force and it takes up to 1.5 m of road displacement for a typical passenger car tire to reach free-rolling conditions again. This is unfavorable for certain longitudinal slip measurements where the tire needs the full plank length to reach steady-state conditions, which is thus not possible. Also, the vertical tire force varies since the vertical axle position is constant, the plank undulates over the support bearings, and the adapter might not be sufficiently concentric with the measurement hub.

Additionally, a constant road velocity is used in the reference angular wheel velocity calculation during the longitudinal slip measurements since the oscillations in the road displacement encoder, due to the meshing of the rack and pinion, results in an excessive oscillatory reference velocity. This constant road velocity is set equal to 0.03092 m/s, which is determined by averaging the measured road velocity of 26 measurements.

The update frequency of the GUI reduces significantly when the execution time exceeds 1000 s. The exact reason for this behavior is unknown, but it is presumably caused by a large amount of data that needs to be transmitted from the Speedgoat to the Host PC and/or the plotting of the signals in multiple graphs in combination with the high sampling frequency. A workaround is created where the complete dataset is sent to the Host PC whereafter only the desired measurement data is saved, since Simulink does not provide a dedicated function to log only a portion of data. The reduced update frequency also means that the heartbeat functionality is not functional, since this requires updating the signal each 0.5 s while the update period becomes as large as 1 s.

The steering angle encoder, road camber angle encoder, and road camber control are not implemented in the current software. The steering angle encoder implementation did not work for unknown reasons, but it was not further investigated since this encoder data is seldom used. It is not exactly known how the road camber angle encoder and control were implemented in the LabVIEW software. Additionally, the RS232 protocol used to communicate with the road camber actuator drive is not supported by the IO modules of the Speedgoat. Moreover, the existing motors will be replaced in the near future, which eliminates the need to implement the current camber motor and RS232 communication. Therefore, it was decided to not implement the road camber encoder and actuator.

The implementation of the existing motors or the replacement of these motors with Stöber-brand motors resolves the issue of manual operation of the road displacement. The plank actuation can be slightly delayed to ensure that the wheel and road start to move with as little time difference as possible if a delay between the wheel rotation and road displacement remains to exist. Actuation of the vertical axle position provides the possibility to design a controller that controls the vertical force on the tire by varying the vertical axle position.

It is also proposed to replace the existing encoders with updated versions, as explained in Chapter 3. The new encoders provide higher-quality signals, which is advantageous for the calculation of the effective rolling radius among other things. Additionally, it is strongly advised to directly measure the actual road displacement instead of deriving it from the pinion shaft position. This will allow compensating the wheel angular velocity for the actual anomalies in the plank velocity, this is also suggested by Van Blijderveen [2]. The encoder replacement would mean that it is no longer necessary to investigate why the current steering angle encoder cannot be implemented.

4.4 Summary

The objectives of the software have been explained in this chapter, from which the requirements have been derived. The high-level design of the developed GUI and control model is described to show that they fulfill the general and specific requirements. Some issues and limitations of the software remain, and proposed solutions are explained. A substantial amount of issues may be resolved by replacing the existing, outdated motors and encoders. Nevertheless, the developed software allows performing various types of measurements. A free-rolling controller to determine the effective rolling radius of a tire has been developed, which will be explained in Chapter 5. The identified effective rolling radius is subsequently used in the longitudinal and combined slip measurements using the slip control operation mode, which is explained in Chapter 6.

Chapter 5

Free-Rolling Controller Design

5.1 Motivation

Free-Rolling Controller

The implementation of the wheel rotation actuator removes the free-rolling capability of the mounted wheel. This means that the flexplates have to be physically decoupled to obtain a freely-rolling wheel and be able to determine the effective rolling radius. This is explained in more detail in Section 2.2. To simplify the procedure of identifying the effective rolling radius and thus reducing the required measurement time, it is desired to implement a controller that regulates the longitudinal force of the tire to its rolling resistance value by adjusting the applied wheel torque. The controller regulates the actuator torque to mimic the free-rolling conditions of the tire when the tire is pressed against the plank. The effective rolling radius for a specific tire and measurement condition can be identified from the measured data. Thereafter, this effective rolling radius, together with the desired longitudinal slip value, can be supplied to the software. The software calculates the required rotational speed of the actuator to create the requested longitudinal slip for that tire and the measurement conditions.

Model Development

To design a suitable controller, a model of the plant is created to represent the physical setup. Using this plant in a closed-loop feedback control model allows investigating the performance and robustness of the controller. Moreover, developing a model provides a means to understand the dynamics of the physical system. Furthermore, testing various controller designs in simulations to determine the closed-loop stability and performance before assessing the actual performance on the Flat Plank itself decreases the risk of damaging expensive parts of the machine, since a poor controller could destabilize the system.

The development of the model for controller design consists of three parts. Firstly, the linear plant model developed by Van Blijderveen [2] is adapted to determine the frequency response of the closed-loop system. This frequency response provides an indication of the performance and stability of the closed-loop controlled system. The second part is the creation of a nonlinear model that incorporates nonlinearities present in the physical setup. A promising controller design, created using the linear model, is implemented in the nonlinear model. This allows assessing the controller performance and stability in the time domain. Once a suitable controller that meets the specifications is found using the linear and nonlinear model, it is tested on the physical setup to determine the actual response and validate the models.

The layout of the closed-loop system is shown in Figure 5.1. The system consists of a controller C and plant P, which represents the wheel rotation actuator. The to-be-controlled system state is the longitudinal force of the tire $F_{x,T}$. The controller acts on $F_{x,e}$, which is the error between the reference longitudinal force $F_{x,r}$ and the actual longitudinal tire force. The output of the controller is the required wheel actuator moment M_M.

In the following section, the linear plant model will be described, followed by the design of a controller using the linear plant model. Subsequently, the nonlinear plant model will be discussed and the nonlinearities present in the physical setup will be introduced. Finally, the results of experiments with the designed controller implemented on the Flat Plank will be presented, together with a discussion of the results.

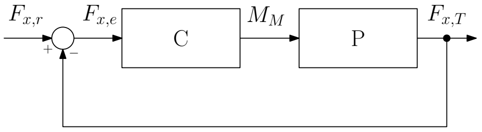

Figure 5.1: Block diagram of the closed-loop longitudinal force control system.

5.2 Linear Plant Model

The linear plant model discussed in this section is an adapted version of the model created by Van Blijderveen [2]. The slewing drive in the wheel rotation actuator is expected to dominate the overall response as a result of the high friction. Therefore, the wheel rotation actuator is represented as a slewing drive with modified inertia, to account for all rotating components in the assembly [2]. The use of kinematic equations to calculate the angular speeds is based on the assumption that there is no backlash between the gears in the system.

The plant consists of the servomotor, slewing drive, hypoid reduction gearbox, and rim with tire. The plant is depicted in Figure 2.4, and a schematic representation is given in Figure 5.2. The output shaft of the servomotor is connected to the input of the hypoid reduction gearbox, the output of this gearbox is attached to the worm screw of the slewing drive. The hypoid reduction gearbox and the worm screw are modeled in the block WS. The worm wheel of the slewing drive, modeled in block WW, is connected via a shaft through the measurement hub to the rim with a tire. Block WW models the modified inertia of the rotating assembly and outputs the rotational velocity of the rim and tire. The torque M_{WW} that is applied on the worm wheel is found by subtracting the tire torque M_T from the worm screw torque M_{WS}. The rim and tire are modeled in block T. Based on the calculated tire moment M_T, the tire longitudinal force $F_{x,T}$ is calculated in block G. This force is used to calculate the control error in the controller block.

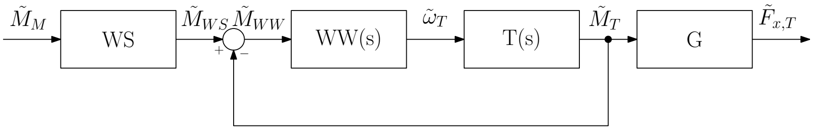

Figure 5.2: Block diagram layout of the plant model, which consists of a hypoid reduction gearbox and a worm screw (WS), a worm wheel (WW), a tire (T), and a conversion (G) block.

The plant is linearized around an operating point $F_{x,r0}$, and the $\sim$ operator indicates that the signal values are relative to that operating point. For instance, $\tilde{F}_{x,r}$ is taken with respect to the operating point $F_{x,r}$ and is obtained from $F_{x,r0}$ as given by

$$\tilde{F}_{x,r} = F_{x,r} - F_{x,r0}. \tag{5.1}$$

The servomotor moment $\tilde{M}_M$ is applied to the hypoid reduction gearbox with speed reduction ratio i_{RED}. The output of the reduction gearbox is connected to the slewing drive, which has a speed reduction ratio i_{SD}. Due to the high friction of the slewing drive, together with friction within the hypoid reduction gearbox, a significant amount of the servomotor moment is lost. An efficiency η, which is assumed constant by Van Blijderveen [2], is used to account for the torque loss. Thus, the conversion of $\tilde{M}_M$ to the worm screw torque $\tilde{M}_{WS}$ of the slewing drive is given by

$$\frac{\tilde{M}_{WS}(s)}{\tilde{M}_M(s)} = WS = \eta i_{RED} i_{SD}. \tag{5.2}$$

The assumption of a constant efficiency fails to represent the complex friction dynamics of the system, which are dependent on the rotational speed and torque, especially around standstill. Van Blijderveen [2] justifies the use of a constant efficiency by stating that the actuator is mainly used in the vicinity of the free-rolling speed of the tire, meaning that the rotational speed dependency of the friction can be neglected. Furthermore, in [2] it is assumed that the force dependency has a minor influence. To experimentally assess the accuracy of these assumptions, measurements with different levels of slip at different vertical forces are performed on the Flat Plank. The efficiency is determined by

$$\eta = \frac{M_{out}}{M_{in}} = \frac{M_T}{M_M - M_F} \cdot 100\%, \tag{5.3}$$

where M_T is the torque generated by the tire, M_M is the delivered torque by the servomotor, and M_F is the friction torque as a function of the rotational servomotor velocity, as given in Figure 5.3. The resulting efficiencies are shown in Figure 5.4. It can be seen that for different levels of slip, thus different levels of rotational speed, the efficiency remains approximately constant. The vertical force only moderately influences the efficiency. Therefore, the assumptions are deemed valid. A constant efficiency is determined by averaging the efficiencies of each measurement, leading to $\eta = 39.2$ %.

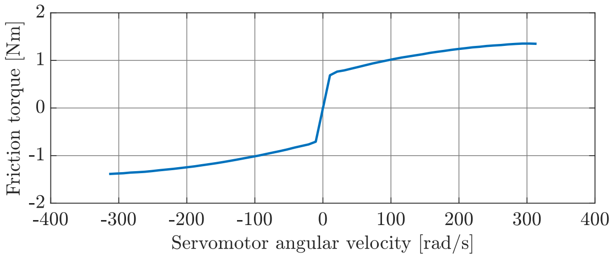

Figure 5.3: The experimentally identified friction torque as a function of the rotational velocity of the servomotor.

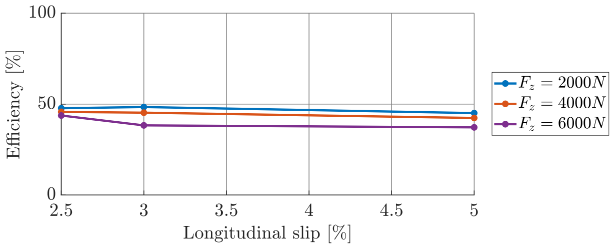

Figure 5.4: Calculated efficiency of the transmission of the wheel rotation actuator for different levels of slip and vertical force.

In the worm wheel block WW(s), the rotational speed of the wheel is determined by

$$\tilde{M}_{WW} = J_{eff}\dot{\tilde{\omega}}_T, \tag{5.4}$$

where ω_T is the rotational velocity of the wheel and J_{eff} is the effective inertia of the complete rotating assembly given by

$$J_{eff} = J_{WW} + J_T + \eta i_{SD}^2 \left(J_{WS} + i_{RED}^2 J_M \right). \tag{5.5}$$

The derivation of the expression for the effective inertia is given in Appendix D. The inertia of all the parts of the measurement hub and the actuator that are driven by the worm wheel are lumped together in J_{WW}. The total inertia of the rim, tire, wheel, adapter and lug nuts is represented by J_T. The individual inertias of the components that rotate at the rotational velocity of the worm screw are combined in J_{WS}. The inertia of the motor and the shaft coupling is given by J_M. The latter two inertias dominate the effective inertia, due to the high relative angular speed resulting from the square of the speed reduction ratio in (5.5). By rewriting (5.4) to the Laplace domain, it is possible to determine the transfer function from $\tilde{M}_{WW}$ to $\tilde{\omega}_T$, which is equal to

$$\frac{\tilde{\omega}_T(s)}{\tilde{M}_{WW}(s)} = WW(s) = \frac{1}{J_{eff}s}, \tag{5.6}$$

where s is the Laplace variable.

A perturbation of the rotating assembly angular speed $\tilde{\omega}_T$ produces a perturbation of the longitudinal force in the contact patch and therefore of the produced moment $\tilde{M}_M$. The tire behaves as a nonlinear damper that produces a force opposite to the direction of the slip speed. In the approach from [14], the nonlinear behavior is linearized around an operating point κ_0 that occurs at a certain angular velocity $\omega_{T,0}$. This leads to a gain that represents how the longitudinal tire force responds to slip perturbations around κ_0. The derivation of the transfer function $T(s)$ using the approach from [14] to represent the tire behavior is explained in [2]. The result is equal to

$$\frac{\tilde{M}_T(s)}{\tilde{\omega}_T(s)} = T(s) = \frac{K'_{x1} F_z r_e r_l}{V_x \left(\frac{\sigma_x}{|V_x|} s + 1 \right)}, \tag{5.7}$$

where K'_{x1} is the normalized longitudinal slip stiffness, F_z is the vertical force, r_e is the effective rolling radius, r_l is the loaded wheel radius, V_x is the plank speed and σ_x is the longitudinal relaxation length. Note that the assumption made in [2] that the loaded wheel radius is equal to the effective rolling radius is omitted. Furthermore, three assumptions are introduced to arrive at this result. Firstly, it is assumed that K'_{x1} is constant and thus does not depend on the slip at operating point κ_0. Secondly, the transient response of the tire as a result of the slip perturbations is implemented as a low pass filter, referred to as the linear transient model. Furthermore, the static parameter σ_x fails to represent the dependency of transient response on variations in slip level and vertical force within a simulation. Van Blijderveen [2] developed this model assuming a constant, non-zero slip level and vertical force. Therefore, a suitable relaxation length is chosen based on the specific slip and vertical force conditions.

Since the output of the plant has to be the longitudinal tire force, the generated tire moment $\tilde{M}_T$ is converted using the loaded wheel radius to obtain $\tilde{F}_{x,T}$. Therefore, the gain G is equal to

$$\frac{\tilde{F}_{x,T}(s)}{\tilde{M}_T(s)} = G = \frac{1}{r_l}. \tag{5.8}$$

The transfer function of the plant can be determined using the block diagram of Figure 5.2 and the individual transfer functions according to

$$\begin{aligned} P(s) &= \frac{\tilde{F}_{x,T}(s)}{\tilde{M}_M(s)}, && (5.9a) \\ &= \frac{G \cdot WS \cdot WW(s) \cdot T(s)}{1 + WW(s) \cdot T(s)}, && (5.9b) \\ &= \frac{i_{RED} i_{SD} \eta K'_{x1} F_z r_e |V_x|}{V_x J_{eff} s \left(\sigma_x s + |V_x|\right) + K'_{x1} F_z r_e r_l |V_x|}. && (5.9c) \end{aligned}$$

5.3 Model Parameters

The used parameters for the controller design are listed in Table 5.1. The tire-specific parameters are those of a Toyo NanoEnergy 3 tire of size 195/65 R15 with a tire inflation pressure of 2.5 bar. The combined efficiency of the reduction gear and slewing drive is determined experimentally as described in Section 5.2. The vertical force is the nominal force of the tire, which is normally used on a Toyota Prius XW50 (fourth generation). The reduction ratios are values provided by the manufacturer. The individual inertia values are taken from [2, Section 4.2]. The effective inertia is calculated using (5.5). The normalized longitudinal slip stiffness is determined from measurements, as well as the effective rolling radius, the loaded wheel radius, the relaxation length, and the average road velocity.

Table 5.1: Parameters used in the linear and nonlinear plant model.

	Description	**Value**
η [%]	Combined efficiency of the reduction gear and slewing drive	39.2
F_z [N]	Vertical force	3700
i_{RED} [-]	Speed reduction ratio of the reduction gear	30.32
i_{SD} [-]	Speed reduction ratio of the slewing drive	47
J_{eff} [kg m^2]	Effective inertia of the complete rotating assembly	1287
J_M [kg m^2]	Effective inertia of the motor shaft and connecting shaft	0.001260
J_{WW} [kg m^2]	Effective inertia of the parts driven by the worm wheel	0.2483
J_{WS} [kg m^2]	Effective inertia of the motor driven by the worm screw	0.005808
J_T [kg m^2]	Effective inertia of the tire, rim, and lug nuts	1
J_{TW} [kg m^2]	Effective inertia of the tire, rim, lug nuts, worm wheel, and worm screw	14.08
K'_{x1} [-]	Normalized longitudinal slip stiffness	24.5
r_e [m]	Effective rolling radius	0.3081
r_l [m]	Loaded wheel radius	0.2955
σ_x [m]	Relaxation length	0.4505
V_x [m/s]	Road velocity	0.03092

5.4 Controller Design

By using the transfer function $P(s)$ of the linear plant, together with the parameters in Table 5.1, it is possible to verify whether a certain controller design ensures stability and achieves the desired performance in the frequency domain. This section describes the desired performance specification and the designed controller, and it discusses the frequency domain results.

Since only a limited road distance is available on the Flat Plank, it is favorable to achieve steady state as quickly as possible to ensure that the tire is in steady state for a significant portion of the road. This allows to accurately determine the effective rolling radius. The measured signals are averaged during post-processing for the total time the tire is in steady state to decrease the influence of noise on the measured signals. It is desired to achieve steady-state within 48.5 s, which is approximately 1.5 m of road displacement resulting in around 2.7 m being available to obtain steady-state measurement data. Furthermore, the controller needs to have sufficient disturbance rejection since the measuring hub outputs noisy signals. Lastly, a certain gain and phase margin are needed to create a safety margin with respect to instability. Variations in the open loop gain may occur as different types of tires can be mounted on the machine, where each type has its distinctive characteristics. It is found from the literature that a phase margin of 30° to 60° and a gain margin of 1 to 3 are usually applied in controller design [28, 29]. Therefore, the desired phase and gain margin are set to 40° and 2, respectively.

The controller has been designed using the loop-shaping method. The open-loop frequency domain response is designed using this approach to satisfy the requirements of the closed-loop system. It is found that a PI controller supplemented with a lead compensator result in the desired performance for the model parameters in Table 5.1. The PI controller is given by

$$C_{PI}(s) = 5 \cdot 10^{-4} \left(\frac{1}{s} + 10 \right). \tag{5.10}$$

The lead compensator is used to achieve the required phase margin and is equal to

$$C_L(s) = \frac{T_d s + 1}{\alpha_l T_d s + 1}, \tag{5.11}$$

where $T_d = 0.1105$ and $\alpha_l = 0.2174$. The controller $C(s)$ is equal to

$$C(s) = C_{PI}(s) C_L(s). \tag{5.12}$$

The settling time of the closed-loop system is determined by applying a step input to the closed-loop transfer function. The step response is shown in Figure 5.5. It shows that the settling time is equal to 32.7 s, meaning that the tire reaches steady-state within 1.01 m. Therefore, the requirement of settling time is well-satisfied. The Bode-plot of the open-loop transfer function is shown in Figure 5.6 to assess the phase and gain margin. In the plot, the phase margin is indicated by the arrow with the annotation ‘PM’. The phase margin is equal to 39.9°. The gain margin is not indicated in the plot, since it is equal to infinite as the phase does not cross -180°. As a result, both margin requirements are met.

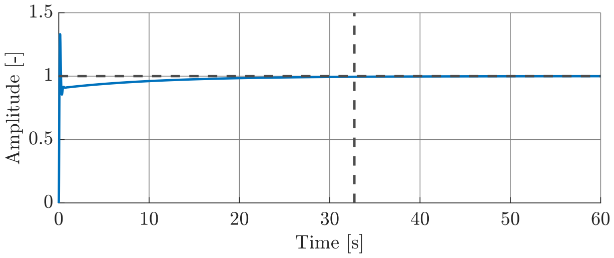

Figure 5.5: Step response of the closed-loop transfer function $H(s)$. The vertical dashed line indicates the settling time.

The performance of a controller in the frequency domain is assessed by using the sensitivity function S and complementary sensitivity function H given by

$$S(s) = \frac{1}{1 + C(s)P(s)}, \tag{5.13a}$$

$$H(s) = \frac{C(s)P(s)}{1 + C(s)P(s)}. \tag{5.13b}$$

The sensitivity function describes the transfer function from external disturbances to the output. Hence, lower values of $|S|$ lead to higher attenuation of disturbances. The complementary sensitivity function is the transfer function from the reference value to the output, meaning that it is desired to have $|H|$ close to 1. In Figure 5.7, the Bode plot of both the sensitivity functions is visualized. From the sensitivity plot, it can be seen that there is good disturbance rejection for low frequencies. The DC magnitude of H is equal to 0 dB and decreases slightly to -0.77 dB for increasing frequency. At around 2.43 Hz, the complementary sensitivity reaches a peak of 3.98 dB, whereafter the magnitude decays. The bandwidth and settling time of a system are closely related, as a higher bandwidth results in a shorter settling time. Therefore, the bandwidth of the system is a result of

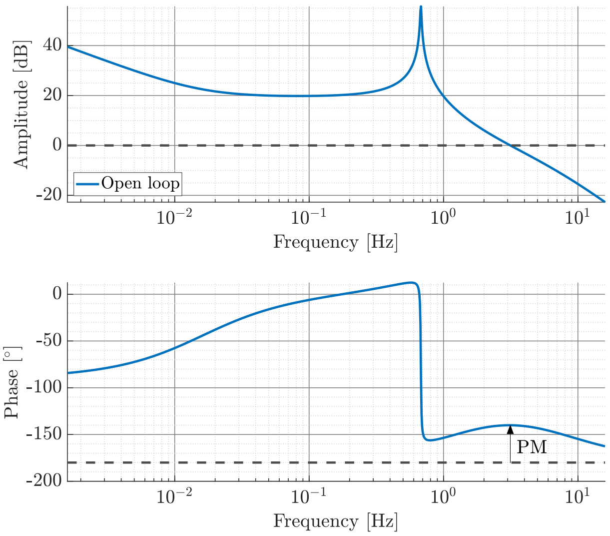

Figure 5.6: Magnitude and phase of the open loop transfer function, plotted against the frequency. The annotation 'PM' indicates the phase margin.

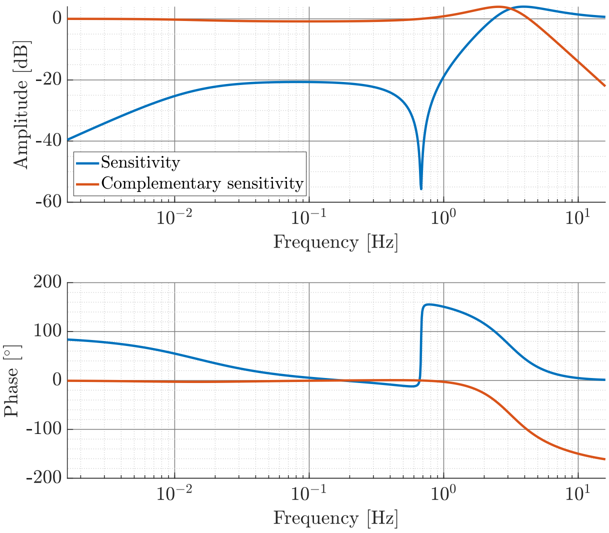

Figure 5.7: Magnitude and phase of the complementary sensitivity H and sensitivity S, plotted against the frequency.

the settling time requirement. The bandwidth is equal to 5.2 Hz and exceeds the bandwidth requirement of Van Blijderveen [2] of 2.4 Hz for the speed control mode.

In Figure 5.8, the pole-zero maps for the sensitivity and complementary sensitivity function are depicted. Only the poles of the complementary sensitivity are visible since the poles of both functions are equal. The closed-loop system is stable since the poles of H, and thus of the closed-loop transfer function, are in the left-half plane. Since one of the poles and one of the zeros of H are very close to each other, they compensate each other. The frequency response of S shows a dip at approximately 0.68 Hz which correpsonds to the pair of complex conjugate zeros close to the imaginary axis.

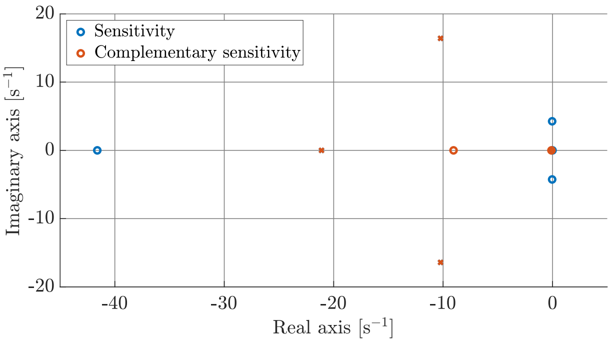

Figure 5.8: Pole-zero map of the sensitivity and complementary sensitivity function.

The designed controller shows promising results in terms of the specified requirements and good disturbance rejection. The controller behavior is evaluated in the frequency domain to obtain an indication of its performance and stability by using the linear plant model. However, the linear plant fails to represent the dynamics of the physical system since nonlinearities of the real system are omitted. Therefore, a nonlinear plant model will be developed to evaluate the performance of the controller and the stability of the closed-loop system with a more accurate representation of the physical system.

5.5 Nonlinear Plant Model

Model Layout & Nonlinearities

The nonlinear plant model is created to incorporate the nonlinearities that significantly contribute to the dynamics of the physical system. This means that not every effect is implemented. It is desired to keep the model simple whilst it is still capable of representing the physical system in such a way that the controller performance can be assessed.

The first nonlinearity that is implemented is the backlash dynamics between two gears. The wheel rotation actuator drives a hypoid reduction gearbox and a slewing drive, each containing one or more gear pairs. The backlash of the transmission is determined by blocking the output, being the worm wheel of the slewing drive, and rotating the input, which is the input shaft of the reduction gearbox. The coupling between the output shaft of the motor and the input of the hypoid reduction gearbox is backlash-free [30]. This approach allows to simplify the transmission to a single-gear pair with a reduction ratio

$$i = i_{RED} i_{SD}, \tag{5.14}$$

and a backlash angle of 30°.

The second nonlinearity is the friction in the system, consisting of the friction in the servomotor, the transmission, and the measuring hub. This friction has a highly nonlinear characteristic and depends on various effects such as velocity, load, temperature, and lubrication [31, 32]. The friction consists of two components. One is the efficiency of the hypoid reduction gearbox and slewing drive, the other is the residual friction that is always produced even if the tire does not generate a reaction torque. The former is proportional to the applied torque and is already incorporated by η given by (5.3). Since no equipment is available to determine the residual torque of each component individually, a combined friction torque is determined. The combined friction torque is defined as the torque that the servomotor has to deliver, which is estimated by the Stöber drive, to rotate at a constant angular velocity while the wheel is mounted, but is hanging freely. This means that no load torque is applied, and the first friction component is equal to zero. However, the friction is dependent on the load. During free-rolling measurements, the tire rotates in the vicinity of the free-rolling speed and will thus generate small longitudinal forces. This results in a small load torque around the wheel spin axis, of which only a negligible portion is applied to the servomotor since the total speed reduction ratio is large. As a result, it is assumed that the friction torque does not depend on the load torque which is generated by the tire. Also, it is expected that the components of the slip actuator operate at a certain, constant, temperature which rules out the temperature dependency of friction torque. Therefore, it is assumed that the friction torque is only dependent on the angular velocity of the motor, which is experimentally determined.

The slewing drive locks up when the tire tries to drive the input, due to inherent characteristics of the slewing drive. This phenomenon occurs at the start of a measurement, where the road starts moving but the tire cannot rotate due to this self-locking. This means that the tire quickly develops a longitudinal force, and the controller requires time to respond to this sudden, large change in force. This results in damage to the tire and the sandpaper, which accumulates over the measurements. To circumvent this, a fixed value of 2 Nm is added to the controller output once the road starts moving. This removes the necessity of implementing this nonlinearity into the model.

As a result of the assumption that the transmission consists of only one gear pair, it is possible to represent the physical wheel rotation actuator in a simplified way, as shown in Figure 5.9. The layout of the closed-loop system remains the same as depicted in Figure 5.1, but the linear plant $P(s)$ is replaced by the nonlinear plant depicted in Figure 5.10. The input and output of the plant remain equal to the motor torque M_M and longitudinal tire force $F_{x,T}$, respectively. In the nonlinear model, the dynamics of the Stöber drive of the wheel rotation actuator are omitted. It is assumed that this Stöber drive has a sufficiently large bandwidth and disturbance rejection to track the requested torque, and it is therefore not included in the model.

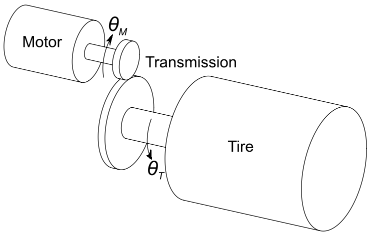

Figure 5.9: Simplified representation of the wheel rotation actuator.

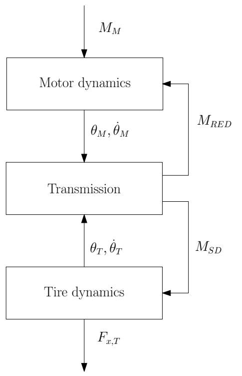

Figure 5.10: Block diagram of the nonlinear plant model.

Nonlinear Model Equations

The plant is subdivided into three parts as can be seen in Figure 5.10. The first part, the motor, describes the dynamics of the motor and includes the combined friction torque M_F of the system. By applying Newton's second law for rotation, the equation governing the motor dynamics is given by

$$M_M - M_F(\dot{\theta}_M) - M_{RED} = J_M \ddot{\theta}_M. \tag{5.15}$$

In this equation, M_M is motor torque, θ_M is the angular rotation of the motor axle, M_{RED} is the torque between the motor and the transmission, and J_M is the equivalent inertia of the motor shaft and the connecting shaft between the motor output and hypoid reduction gearbox input. The measured friction torque $M_F(\dot{\theta}_M)$ is visualized in Figure 5.11.

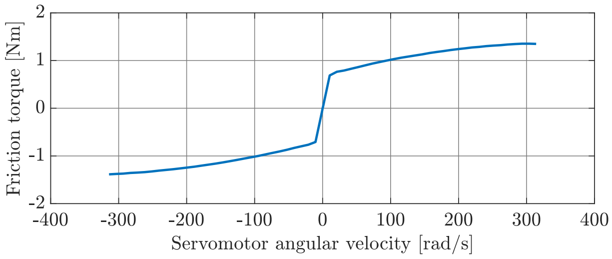

Figure 5.11: The experimentally identified friction torque as a function of the rotational velocity of the servomotor.

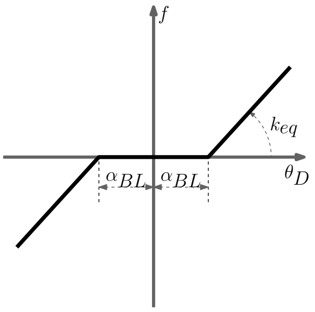

Figure 5.12: Visualization of the dead-zone model that is implemented to represent the backlash dynamics between two gears. In the plot, the nonlinear spring characteristic f is plotted against the relative angular displacement θ_D.

The second part contains the dynamics of the transmission where the backlash is modeled using a dead-zone model, which essentially represents a nonlinear spring as shown in Figure 5.12 [33, 34]. The equation describing the nonlinear spring characteristic is given by

$$f(\theta_D) = \begin{cases} k_{eq}\left(\theta_D - \operatorname{sgn}(\theta_D)\alpha_{BL}\right), & |\theta_D| \geq \alpha_{BL} \\ 0, & |\theta_D| < \alpha_{BL} \end{cases}, \tag{5.16}$$

where $\alpha_{BL} = 15°$ is half of the backlash angle, and $k_{eq} = 2000$ Nm/rad is the equivalent torsional stiffness of the components in the transmission. This stiffness is determined by calculating the torsional stiffness k_i of each individual component, whereafter k_{eq} is found using

$$\frac{1}{k_{eq}} = \sum_{i=1}^{N} \frac{1}{k_i}, \tag{5.17}$$

where N is the number of components. The relative angular displacement θ_D between the input gear and the output gear is given by

$$\theta_D = \theta_M - i\theta_T, \tag{5.18}$$

where θ_T is the angular rotation of the tire. It is assumed that there is no friction in the backlash region ($|\theta_D| < \alpha_{BL}$). A small artificial damping d is introduced in the system to prevent it from having undamped vibration modes that would make it difficult to be numerically integrated in the time domain. Subsequently, M_{RED} is given by

$$M_{RED} = f(\theta_D) + d\dot{\theta}_D. \tag{5.19}$$

Considering the combined efficiency of the transmission, and the total reduction ratio i, the torque between the transmission and the tire M_{SD} is given by

$$M_{SD} = \eta i M_{RED}. \tag{5.20}$$

The third part implements the dynamics of the wheel and tire. The approach to modeling the tire dynamics is equal to that of the linear plant. M_{SD} is applied to the wheel, accelerating the output components with equivalent inertia J_{TW}. The tire generates a longitudinal force in the contact path acting against the direction of the moving road, leading to a moment M_T about the wheel spin axis. The tire dynamics are described by

$$M_{SD} - M_T = J_{TW}\ddot{\theta}_T, \tag{5.21}$$

where the equivalent inertia J_{TW} consists of the inertia of the tire, rim, lug nuts, worm wheel, and worm screw. M_T is given by (5.7), and $F_{x,T}$ is obtained by dividing the wheel moment with the loaded wheel radius r_l. Instead of assuming a constant road velocity in the linear model, the acceleration of the road that is required to reach the reference speed V_x from standstill is incorporated. This acceleration is experimentally determined and equal to 0.206 m/s^2.

Time Domain Performance

The controller and nonlinear plant are implemented in MATLAB Simulink, which allows the simulation of the dynamics to assess the performance and the stability in the time domain. The simulation uses the parameters in Table 5.1. At the start of the simulation, the wheel, motor, and road are stationary, and the initial value of θ_D is 0°. At 0.1 s, the road accelerates with constant acceleration to its steady-state velocity V_x. The simulation ends when the road has reached the maximum displacement of 4.2 m, which takes approximately 136 s.

During free-rolling conditions, the tire generates a small negative longitudinal force, known as the rolling resistance. During experiments, it turns out that it is not possible to regulate the longitudinal force if a braking moment needs to be applied when the servomotor is used in torque control. In Figure 5.13, the servomotor torque for different vertical forces is plotted against various levels of longitudinal slip. For negative slip levels, only the friction torque M_F needs to be delivered by the servomotor. The slewing drive provides the required braking torque when the tire needs to be slowed down due to the result of the high friction. The servomotor only needs to deliver the no-load friction torque to prevent the slewing drive from self-locking. Therefore, it is decided to use a small positive reference longitudinal force $F_{x,r}$ to circumvent this issue. The reference value that is used in both the simulation and the experiment is equal to 50 N, which is close to the rolling resistance force of a tire.

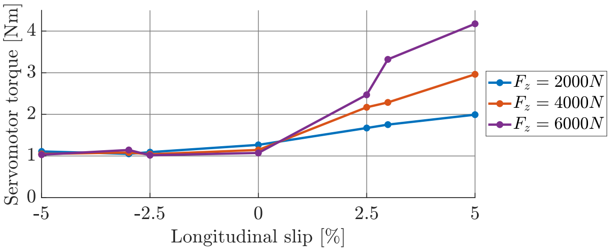

Figure 5.13: The torque delivered by the servomotor for different vertical forces and slip levels.

In Figure 5.14 and Figure 5.15, simulation results for $F_{x,T}$ and θ_D are displayed. In both plots, a zoomed-in section is given for the first 0.03 m of the road displacement where the start of the road is indicated by the dashed vertical line. The motor output M_M accelerates the input of the transmission, which means that θ_D grows positive until the two gears engage after moving through the backlash. The gear engagement is indicated in the zoomed-in plot of Figure 5.14 by the black diamond. Up until the point the gears engage, the tire rotates freely while the road is moving. This means that the tire should generate a negative longitudinal force, while Figure 5.14 shows that the tire generates a positive force. This is the result of the artificial damping term in (5.19). The motor accelerates the tire once the gears engage. This results in the peak longitudinal force, whereafter the force steadily decreases until the reference value of 50 N is reached. Figure 5.15 shows that once the gears are engaged, they remain engaged throughout the whole plank displacement.

The simulation results show that the linear controller is capable of regulating the longitudinal tire force to the reference value even with the nonlinearities present. In terms of the requirements, the longitudinal tire force is within ± 5 % of the reference value after 1.41 m, which satisfies the settling distance requirement for the Toyo tire for the specified operating conditions.

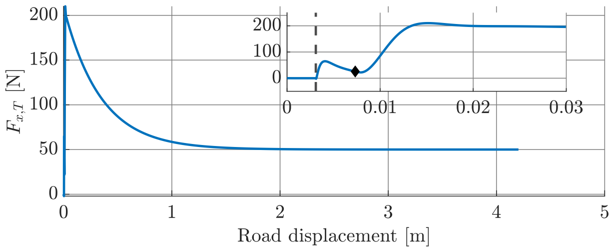

Figure 5.14: Simulated longitudinal tire force plotted against road displacement, with a zoomed-in section of the first 0.03 meter of road displacement.

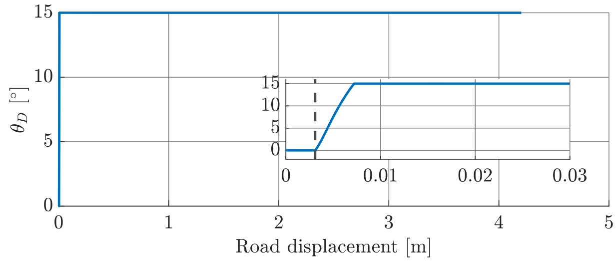

Figure 5.15: Simulated relative angular displacement plotted against road displacement, with a zoomed-in section of the first 0.03 meter of road displacement.

5.6 Functional Testing

The simulation results show that the controller is capable of regulating the motor torque to obtain a freely rolling tire within a reasonable road distance. Therefore, the controller is implemented on the Flat Plank and experiments are done to investigate the performance and stability of the controller under a variety of common measurement conditions.

Firstly, a comparison between the simulation and measurement results for the Toyo NanoEnergy 3 tire is made. The characteristics of this tire are used in the plant models to develop and test the controller. Comparing the simulation and measurement results gives an insight into the accuracy of the model and its underlying assumptions. Then, experiments are discussed where the Toyo tire is subjected to a range of vertical forces. Since the vertical force influences multiple tire characteristics, the experiments will show whether the controller can cope with this variation. Measurement results are presented for three tires of different manufacturers and sizes operating at their nominal condition. The main reason to use these tires is the difference in the free radius r_0 of the tires. This means that the loaded tire radius r_l varies, which affects the generated moment around the wheel's spin axis. The tires cover a significant portion of the allowable radii on the machine, and it is assumed that this range is sufficient to verify whether the controller can handle this variation of the loaded tire radius. Moreover, different types of tires also each have different characteristics, which influence the longitudinal force response.

Each measurement is repeated three times, at a starting angle of 0°, 120°, and 240°. This mitigates the influence of random errors, and allows to determine the spread of the results and assess the reliability of the result.

Simulation vs. Measurement

In Figure 5.16 and Figure 5.17, the simulated and measured tire longitudinal force and motor torque are depicted. A zoomed-in section is shown in each figure to visualize the dynamics at the start of the road displacement. In the simulation environment, the road movement is started after 0.1 s. Therefore, the measured data is shifted by 0.1 s to align the start of the road displacement in the simulation and the measurement.

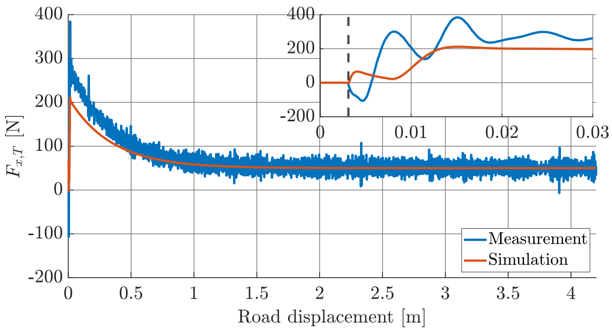

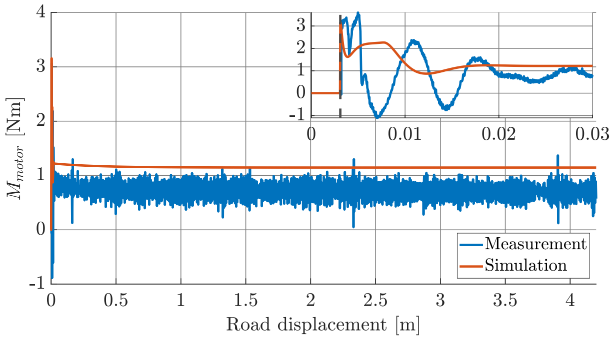

Figure 5.16: Longitudinal force of the measurement and simulation, for the Toyo NanoEnergy 3 tire at nominal conditions.

Figure 5.17: Motor torque of the measurement and simulation for the Toyo NanoEnergy 3 tire at nominal conditions.

As is visible in the zoomed-in section, in the measurements the tire first generates a negative force. The occurrence of the negative force is explained by the fact that the Simulink control model running on the Speedgoat has to respond to the start of the plank, which is actuated by the operator. Since only the wheel rotation actuator is controllable from the Simulink control model, it is not possible to start the wheel rotation and road displacement in sync. Therefore, the free-rolling controller in the Simulink control model is enabled once the road starts moving, which is measured by the plank position encoder. Due to a small delay, the tire is momentarily standing still while the road moves, leading to a build-up of a negative longitudinal force until the wheel starts rotating. Unfortunately, the delay varies between different tests, which means that it is not possible to incorporate a constant delay in the model.

The overshoot of the measured tire force is higher compared to the simulated force. This is the result of the mismatch between the modeled and actual combined friction torque M_F. The simulated steady-state motor torque shows a significant difference with the measured torque as shown in Figure 5.17. Furthermore, the measured longitudinal force shows oscillations, while the simulated force does not. The high-frequency oscillations are inherent to measurements, as noise is introduced to the measured signals. Some noise is filtered by the measurement amplifier, the data acquisition system, and during post-processing. The largest part of the oscillations occurs due to the varying road velocity. It is assumed in the model that the velocity is constant. On the Flat Plank, the road is moved using a rack-and-pinion, one on each side of the road. The velocity of the road is not constant due to the meshing of the pinion with the rack. This varying velocity leads to a non-constant longitudinal slip, ultimately leading to oscillations in the longitudinal tire force. Some larger oscillations arise, for example at a road displacement of approximately 0.15 m, 2.35 m, and 3.90 m, which are due to worn patches in the sandpaper on the road surface. Due to a different friction level, the generated tire force changes quickly. The controller responds to this force change causing it to overshoot. This overshoot is visible in Figure 5.18 at a road displacement of approximately 0.15 m, 2.35 m, and 3.90 m. Lastly, a small error is introduced due to parasitic signal filtering to reduce the influence of the radial preload of the shaft end piece on the shaft. This filtering reduces the influence of the parasitic signals, but a sinusoidal-like error remains with an amplitude of approximately 15 N.

The non-constant road velocity and the difference in steady-state torque are included in the nonlinear model. In steady-state, the motor torque that has to be delivered is dominated by the friction torque at that specific rotational speed since the generated moment about the spin axis of the wheel is negligible. The look-up table of the friction torque that is used in the model, depicted in Figure 5.11, is scaled so the steady-state value of the simulated friction torque matches the measured friction torque at the specific, steady-state rotational speed. Furthermore, the measured road velocity is supplied to the nonlinear model as an input signal. The longitudinal tire force and servomotor torque of the improved simulation and measurement are given in Figure 5.18 and Figure 5.19, where it can be seen that the improved simulation and measurement results match much better. The oscillations in the measured and simulated force are of the same frequency, but different amplitude, which is visualized in the zoomed-in section of Figure 5.18. This result indicates that the road velocity seems to be the source of the oscillations.

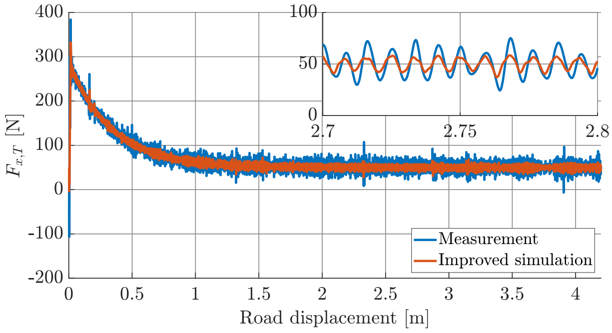

Figure 5.18: Longitudinal force of the measurement and improved simulation, for the Toyo NanoEnergy 3 tire at nominal conditions.

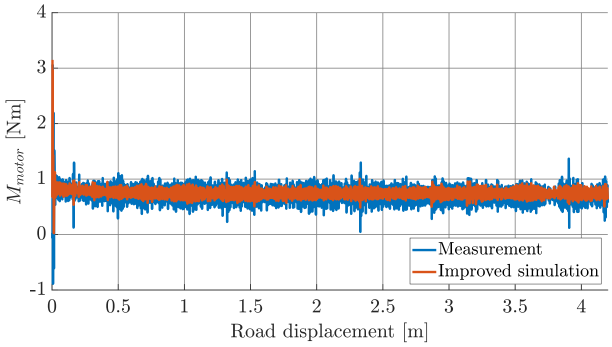

Figure 5.19: Motor torque of the measurement and improved simulation for the Toyo NanoEnergy 3 tire at nominal conditions.

The settling distance and steady-state error are determined to discuss the performance of the controller. It is challenging to accurately determine the settling distance and error due to the oscillations in the measured force. Therefore, an exponential function is fitted, as explained in Appendix E, of which the result is shown in Figure 5.20. The settling distance of the measurement is equal to 1.54 m while the simulated result is 1.41 m, as a result of the difference in friction torque which influences the longitudinal force response. The settling distance of the improved simulation is equal to 1.54 m, which matches the settling distance of the measurement. The steady-state error of the measurement is determined by calculating the relative difference between the average longitudinal force for the last 1.5 m of road displacement and the reference value of 50 N. The steady-state error of the measurement 0.54 %.

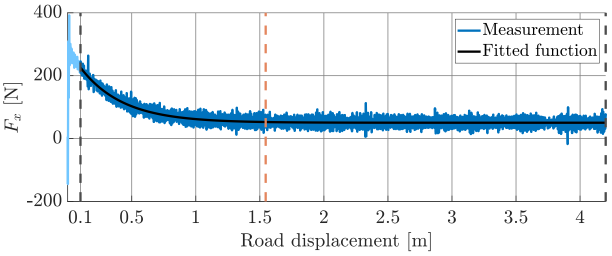

Figure 5.20: Measured longitudinal tire force and the fitted exponential function, plotted against the road displacement. The two black, vertical dashed lines indicate the start and end points of the fit. The orange, vertical dashed line indicates the settling distance.

The goal of the free-rolling controller is to determine the effective rolling radius of a tire under specific measurement conditions without having to disconnect and reconnect the flexplates. The measured road velocity and angular velocity of the servomotor are used to determine the effective rolling radius. The reason to use the angular servomotor velocity, instead of wheel velocity, is the higher quality of the signal as explained in Section 3.1. Since it is assumed that the tire is in free-rolling condition, it is possible to determine the effective rolling radius r_e using

$$r_e = i\frac{V_x}{\omega_M}\cos(\alpha), \tag{5.22}$$

where ω_M is the angular velocity of the servomotor and α is the steering angle, which in this case is equal to 0°. The mean V_x and ω_M are calculated for the road displacement where the tire is assumed to be in steady-state, which is from 1.54 m to 4.1 m. For the measurements at each initial rotation, the effective rolling radius is calculated. A mean effective rolling radius is determined by averaging the three results for that specific measurement condition. For the measurement discussed in this subsection, the average effective rolling radius is equal to 0.3108 m. The free-rolling radius that is measured with disconnected flexplates is equal to 0.3081 m. The error between these two effective rolling radii is 0.88 %. This shows that the free-rolling controller, at least in this specific operating condition, is capable of providing measurement data to accurately determine the effective rolling radius without having to physically disconnect and reconnect the flexplates of the wheel rotation actuator.

Influence of the Vertical Force

The free-rolling controller is designed based on the tire parameters of the Toyo NanoEnergy 3 tire at a specific vertical force. To assess the robustness of the controller in terms of varying loading conditions of the tire, this section describes the results of measurements where the tire is subjected to five levels of vertical force at a tire inflation pressure of 2.5 bar: $F_z \in [1000\ 1850\ 3700\ 5550\ 8000]$ N. This range covers the allowable vertical force range on the Flat Plank.

The steady-state error is plotted against the vertical force in Figure 5.21. Three repetitions per vertical force are indicated. As can be seen, the absolute error is within 1 % without a clear dependency on the vertical force. The settling distance is given in Figure 5.22, which shows that the vertical force has a negligible influence on the settling distance as the difference between the minimum and the maximum value is less than 0.05 m.

The results show that the vertical force hardly influences the longitudinal force response during a free-rolling measurement. To explain this observation, the applied longitudinal slip as a function of road displacement is calculated using the identified effective rolling radius from the corresponding measurement. In Figure 5.23 the calculated longitudinal slip is plotted against the road displacement for five levels of vertical force. It turns out that the longitudinal slip is in the vicinity of 0 % after 0.02 m of road displacement for all measurements with varying vertical force. The relaxation length at the lowest vertical force is approximately 0.08 m, and the relaxation length increases with increasing vertical force. This means that the contact patch cannot deform sufficiently to reach the high longitudinal slip levels and thus does not develop large longitudinal forces. Therefore, the vertical force hardly influences the longitudinal force response, explaining why the steady-state error and settling distance are comparable for all vertical forces.

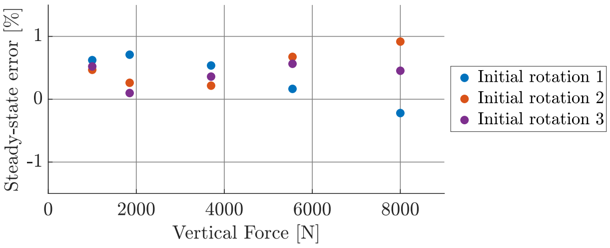

Figure 5.21: Steady-state error for the different vertical forces, for the three starting positions per vertical force.

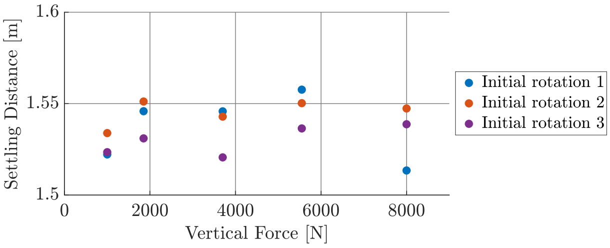

Figure 5.22: Settling distance for the different vertical forces, for the three starting positions per vertical force.

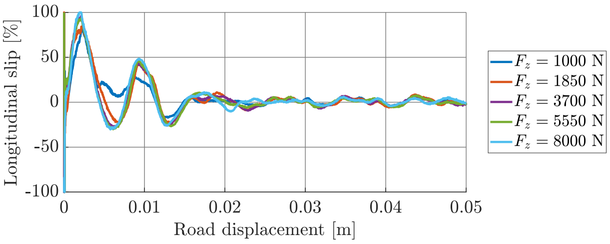

Figure 5.23: Calculated longitudinal slip level plotted against the road displacement.

Influence of Tire Parameters

The Flat Plank allows measurements of different kinds of tires, which differ in parameters such as tire radius, contact patch dimensions, and stiffnesses. These parameters influence the longitudinal force response, potentially leading to an unstable closed-loop system as the free-rolling controller is designed using the parameters of a specific tire for one measurement condition. Therefore, three types of tires are used in measurements in their respective nominal conditions and are listed in Table 5.2. The nominal conditions are the nominal vertical force F_{z0}, nominal tire inflation pressure p_0, and free radius r_0.

Table 5.2: Name, size, free radius, and nominal conditions of the three tires which have been mounted on the Flat Plank to test the free-rolling controller.

	Michelin EnergySaver	**Toyo NanoEnergy**	**Continental EcoContact**
Tire size	165/65 R14	195/65 R15	155/70 R19
F_{z0} [N]	2400	3700	3250
p_0 [bar]	2.1	2.5	2.8
r_0 [m]	0.285	0.318	0.350

The resulting steady-state error and settling distance are visualized in Figure 5.24 and Figure 5.25, respectively. The steady-state error for the Michelin tire is more spread out than those of the Toyo and Continental tires. Nevertheless, the absolute error is smaller than 1.5 %, which in essence means that the error is smaller than 0.75 N with respect to the reference of 50 N. The larger spread of the Michelin tire also holds for the settling distance, but the difference between the minimum and maximum distance of all measurements is less than 0.06 m.

Finally, an experiment with a racing tire is performed. The controller is not able to regulate the longitudinal tire force to the reference value and force oscillations of approximately 600 N occur. The suspected reason for this behavior is the high longitudinal slip stiffness of the racing tire, which is significantly higher than that of road tires [1]. As a result, the control loop becomes unstable since the open loop gain becomes too large. Therefore, a method for tuning the control loop parameters should be developed to make the system able to deal with special tires.

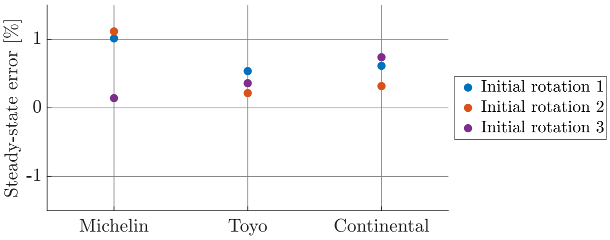

Figure 5.24: Steady-state error for the different tires, for the three starting positions per tire.

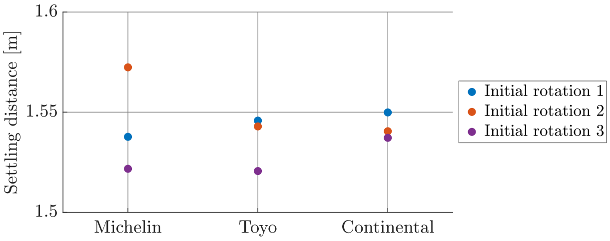

Figure 5.25: Settling distance for the different tires, for the three starting positions per tire.

5.7 Summary

To develop a controller that is capable of regulating the longitudinal tire force to the desired reference value, the linear plant model of the wheel rotation actuator from Van Blijderveen [2] is adapted. The linear model is expanded to a nonlinear version that implements friction and backlash dynamics to include the nonlinearities of the physical setup.

A PI controller, supplemented with a lead compensator, is designed using the linear model. This controller achieves the desired performance in the frequency domain. It is verified whether the controller can deal with the nonlinearities that are present in the physical setup by means of a simulation in MATLAB Simulink. The controller is implemented on the Flat Plank to perform measurements since both the frequency and the time domain results are satisfactory.

A comparison is made between the nonlinear model and the measurement results, which show that the model sufficiently accurately represents the physical system after making minor adjustments to the model. Additionally, the controller is subjected to different measurement conditions to assess its robustness. The results indicate that the controller is capable of creating free-rolling conditions for multiple passenger car tires under varying vertical forces, but fails to do this for a racing car tire. The tuning of the controller parameters for this specific tire does not present particular challenges and a method can be developed in the future. Nevertheless, the controller is capable of providing the necessary measurement data to identify the effective rolling radius of a passenger car tire, without having to disconnect and reconnect the flexplate drum.

Chapter 6

Tire Transient Measurements

In this chapter, the focus is on the transient longitudinal and combined slip measurements that are performed on the Flat Plank. These measurements are carried out using the Speedgoat GUI and control model described in Chapter 4. The results are used to identify the parameters of two longitudinal transient tire models and the MF-Tyre/MF-Swift model, which is the subject of Chapter 7. This chapter begins by explaining the goal of the experiments, followed by the measurement methods. Subsequently, the results are described together with a discussion of the results, where only the results for the Toyo tire are presented. The given trends and explanations also hold for the Continental tire tested.

6.1 Goals

The wheel rotation actuator provides a new method to identify the longitudinal transient behavior. The main goal of the measurements is to investigate the influence of different operating conditions on the longitudinal transient behavior of a tire. A longitudinal slip step is applied to a free-rolling tire to obtain the transient longitudinal force response, from which the tire model parameters can be identified. The operating conditions that are varied are the vertical force, tire inflation pressure, side slip angle, and camber angle.

An additional objective is to evaluate the repeatability of the measurement results. This gives an indication of the reliability of the identified parameters, together with the necessity to repeat measurements and average their results to obtain a representative set of parameters.

6.2 Measurement Methods

This section explains the measurement plan, which describes the types of tires, the nominal conditions, the measurement types, and the operating conditions. Subsequently, the measurement approach and the post-processing of the data are explained.

Measurement Plan

The employed tires are a Toyo NanoEnergy 3 (195/65 R15 95T) and a Continental EcoContact 6 (155/70 R19 84Q) tire, which are commonly used on a Toyota Prius and BMW i3, respectively. In this research, the nominal vertical force F_{z0} is defined as

$$F_{z0} = \frac{m_{veh} g}{4}, \tag{6.1}$$

where m_{veh} is the curb mass of the vehicle on which the tire is commonly used. The nominal tire inflation pressure p_0 is defined as the inflation pressure that is advised by the car manufacturer for the corresponding vehicle. The vertical forces and inflations pressures that are applied in the measurements, together with their nominal values, are provided in Table 6.1. Note that the nominal side slip and camber angle are equal to 0°.

The measurements that are performed per tire are listed in Table 6.2, together with the corresponding operating conditions in terms of the vertical force F_z, tire inflation pressure p, side slip angle α, and camber angle γ. The longitudinal slip κ that is applied during each measurement is equal to $[0, \pm 1, \pm 2, \pm 5, \pm 10]$ %. The angular starting position of the tire prescribes how the circumferential irregularities, such as tire out-of-roundness, are related to the plank displacement. Therefore, each measurement is repeated at three angular positions, spaced 120° apart, to mitigate the effects of circumferential-related errors.

Table 6.1: Vertical forces and tire inflation pressures for the Toyo and Continental tire.

		Toyo	**Continental**
F_z [N]	F_{z1}	1850	1625
	$F_{z2} = F_{z0}$	3700	3250
	F_{z3}	5550	4875
p [bar]	p_1	2	2.3
	$p_2 = p_0$	2.5	2.8

Table 6.2: Performed measurements per tire, together with their corresponding operation conditions. The vertical forces and tire inflation pressures per tire are defined in Table 6.1.

Measurement	$\boldsymbol{\alpha}$	$\boldsymbol{\gamma}$	**Toyo**	**Continental**
Effective rolling radius	[0 1 5 10]°	[0 5]°	$F_z,\ p$	$F_z,\ p$
Contact patch	0°	0°	$F_z,\ p$	$F_z,\ p$
Vertical stiffness	0°	0°	up to $F_z = 6000$ N, p	up to $F_z = 6000$ N, p
Longitudinal transient	0°	0°	$F_z,\ p$	$F_z,\ p$
Longitudinal transient with camber	0°	5°	$F_{z2},\ p_2$	
Combined transient	[0 1 5 10]°	0°	$F_{z2},\ p_2$	$F_{z2},\ p_2$
Combined transient with camber	[0 1 5 10]°	[0 5]°	$F_{z2},\ p_2$	

Four operating conditions of the Toyo tire are repeated ten times from the same starting position to investigate the repetitiveness of the results. The measurements are performed at nominal vertical force and inflation pressure without camber, for the following conditions listed below.

- **Condition 1**: $\kappa = 1$ % and $\alpha = 0°$,
- **Condition 2**: $\kappa = 1$ % and $\alpha = 5°$,
- **Condition 3**: $\kappa = 5$ % and $\alpha = 0°$,
- **Condition 4**: $\kappa = 5$ % and $\alpha = 5°$.

Further information on the file structure of the measurements and the naming convention is presented in Appendix F.

Measurement Approach

The tire generates a negative longitudinal tire force at the start of a longitudinal slip measurement due to the delay of the wheel angular rotation actuation with respect to the plank displacement actuation, as discussed in Chapter 5. The longitudinal slip step is applied after 1.5 m, to achieve steady-state free-rolling before applying the slip step.

The steering and/or camber angle are applied before the tire is vertically loaded. The steering angle is manually set by rotating the handwheel and verifying the angle via the protractor. The camber angle is set via the LabVIEW software to the desired angle. The road camber controller regulates the camber angle to 0° during measurements without a camber angle.

Post-processing

The measured forces and moments contain disturbances that primarily originate from tire irregularities, unevenly worn sandpaper, non-constant road velocity, noise induced by surrounding electrical equipment, and parasitic forces remaining after applying the parasitic force filter. Therefore, the three measurements per operating condition are averaged to reduce the influence of the disturbances. The road displacement is used as an independent variable to which each measured signal is related. Each signal of each measurement is interpolated with respect to a road displacement ranging from 0 m to 4.1 m with an interval of 10^{-4} m, since the sampled road positions are not uniform between measurements. Subsequently, the measurement signals per operation condition are averaged, whereafter the averaged signals are filtered with a lowpass filter of 10 Hz.

6.3 Results & Observations

In total, more than 800 measurements have been performed to obtain data for the identification of the longitudinal transient and MF-Tyre/MF-Swift model parameters. In this section, a selection of the results for the Toyo tire is discussed to illustrate the results. Firstly, the influence of the operating conditions on the effective rolling radius is illustrated, followed by the pure longitudinal slip results for the nominal operating conditions. Subsequently, the influence of the vertical force, tire inflation pressure, side slip, and camber on the transient force response is discussed. The results shown for a specific varying operating condition mean that the other operating conditions are equal to their nominal value, unless explicitly indicated. The contact patch dimensions and stiffness measurements are not discussed in this section. The results of these measurements are given in Appendix G for the Toyo tire.

Effective Rolling Radius Results

The effective rolling radius r_e for different vertical forces and tire inflation pressures is given in Figure 6.1. It is seen that r_e decreases for increasing vertical force and increases for increasing inflation pressure. The effect of α and γ on r_e is illustrated in Figure 6.2, which shows that r_e increases until $\alpha = 5°$, whereafter it decreases. This effect is amplified when the camber angle is increased.

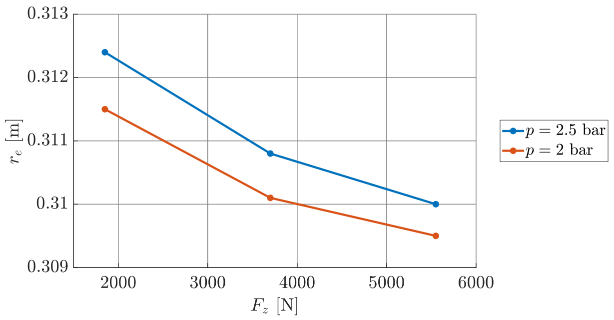

Figure 6.1: Effective rolling radii as a function of the vertical force for two tire inflation pressures.

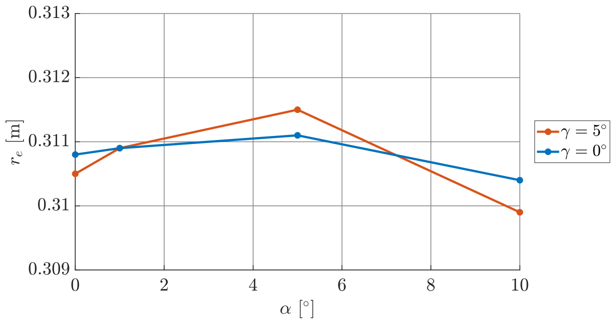

Figure 6.2: Effective rolling radii as a function of the side slip angle for two camber angles, at nominal vertical force and tire inflation pressure.

Nominal Results

Figure 6.3 shows the resulting longitudinal tire force when the Toyo tire is subjected to nine longitudinal slip step levels at its nominal vertical force and inflation pressure. Additionally, it shows two vertical dashed lines that indicate the zoomed-in section given in Figure 6.4, which visualizes the longitudinal force around the road displacement where the longitudinal slip step is applied to the tire. Figure 6.3 shows distinct levels of longitudinal force, which smoothly grow until they level off to a steady-state value. The transient behavior is clearly visible. It is furthermore observed that the force saturates within a smaller plank displacement for higher slip values.

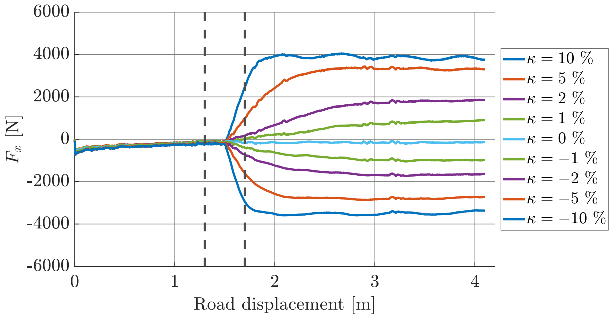

Figure 6.3: The longitudinal force responses as a function of road displacement for nine levels of slip applied to the Toyo tire at nominal conditions.

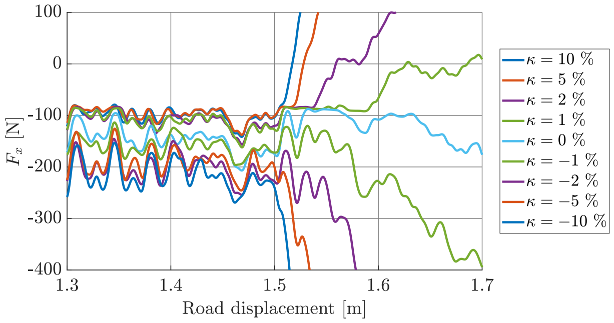

Figure 6.4: Zoomed-in section of Figure 6.3. The vertical lines in Figure 6.3 indicate the start and end of the zoomed-in section.

Figure 6.4 clearly shows that the tire generates a small, negative longitudinal force during free-rolling conditions. The wheel speed matches a reference rotational velocity during free-rolling, which is calculated using a constant road velocity and the effective rolling radius of the tire that is identified using the free-rolling controller. It is expected that the tire generates a longitudinal force of approximately 50 N since this is the reference value supplied to the free-rolling controller. A small deviation in free-rolling conditions occurs due to a mismatch between the expected and actual plank speed. The average road velocity before and after the longitudinal slip step is plotted against the desired longitudinal slip in Figure 6.5. The figure shows that the average V_x is close to 0.03096 m/s before the longitudinal slip step is applied for this operating condition, in contrast to 0.03092 m/s that is used in the Speedgoat control model. Additionally, the average velocity increases or decreases after the longitudinal slip step, corresponding to the sign and magnitude of the longitudinal slip value. The actual, average slip value κ_{act} is calculated during post-processing and is given per desired slip level κ_{des} in Table 6.3. This table shows that the actual slip value is -0.16 % for a desired slip of 0 %, which leads to the small, negative longitudinal force before the step is applied. Furthermore, it is seen that the actual slip magnitude is lower than the desired magnitude, except for -1 %.

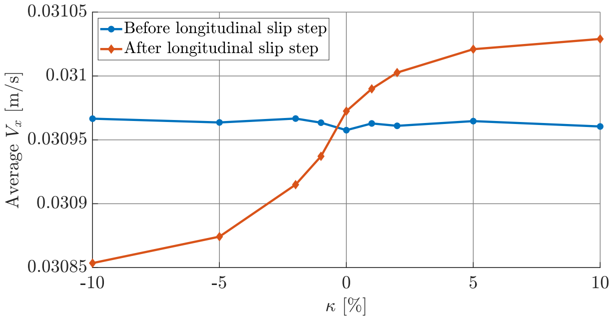

Figure 6.5: The average road velocity, before and after the slip step, is plotted against the longitudinal slip value.

Table 6.3: Desired and actual average longitudinal slip level and the percentual change in vertical force before and after the slip step is applied. The given values are of the Toyo tire measured under nominal conditions.

κ_{des} [%]	**-10**	**-5**	**-2**	**-1**	**0**	**1**	**2**	**5**	**10**
κ_{act} [%]	-9.80	-4.85	-1.98	-1.05	-0.16	0.78	1.73	4.66	9.61
ΔF_z [%]	-4.86	-3.36	-1.90	-1.41	-1.29	-0.80	-0.36	0.12	0.18

In Figure 6.3, it is seen that the positive slip measurements (driving) generate a steady-state force magnitude that is larger than the corresponding negative slip value (braking). There are a couple of reasons for this result. Firstly, the vertical force on the tire is not constant due to the fixed axle height. The relative change in average vertical force before and after the applied step slip is given in Table 6.3. The vertical force remains approximately constant for positive slip, while it decreases when introducing a negative slip. This directly influences the longitudinal force generation. Secondly, tires show an asymmetric response between negative and positive slip conditions, even with accurate slip [2, 15].

Some force fluctuations that are visible in Figure 6.3 seem to correlate with the longitudinal position of the plank. An undulation of the force responses for strictly positive slip is seen at a distance of 2.1 m. Similarly, two variations are seen at around 2.9 m for $\kappa \geq -1\%$ and around 3.2 m for all slip values. Figure 6.6 provides a zoomed-in section of the longitudinal force response and vertical force for $\kappa = 1\%$. The vertical dashed lines indicate the moments where the plank rolls onto or off a vertical support bearing. This indicates that the fluctuation at 3.2 m is presumably the result of the plank structure rolling off of a set of vertical support bearings, as explained in Chapter 3. The undulation around 2.9 m seems to be related to the vertical force variation seen in the bottom plot of Figure 6.6. No final conclusions can be drawn from the presented results and further research is required to identify the causes of the undulations.

Some force responses remain constant for a certain amount of road displacement after the slip step is applied to the tire. This behavior does neither occur for each slip value nor for a constant amount of road displacement, and it is also not constant between the ten repetitions of one operating condition. Figure 6.7 depicts the longitudinal forces responses of $\kappa = 1$ % and $\kappa = 2$ % for the road displacement around the application of the longitudinal slip step. The longitudinal force is approximately constant between the two black dots, which is approximately 0.080 m of road displacement for $\kappa = 1$ % and 0.035 m for $\kappa = 2$ %. The exact reason for the behavior is unknown, but it is suspected that this is the result of an interaction between the backlashes in the gearboxes of the wheel rotation actuator and the backlash in the rack-and-pinion gear of the plank actuation. However, the noisy signals of the wheel and plank position encoders do not allow for drawing a final conclusion.

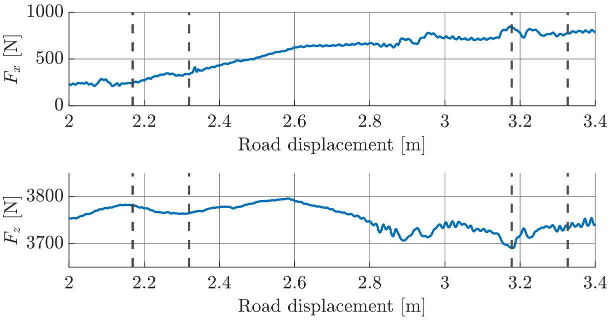

Figure 6.6: The longitudinal and vertical force of the measurement for $\kappa = 1$ % as a function of road displacement. The vertical dashed lines indicate the position of the bearings that support the plank structure.

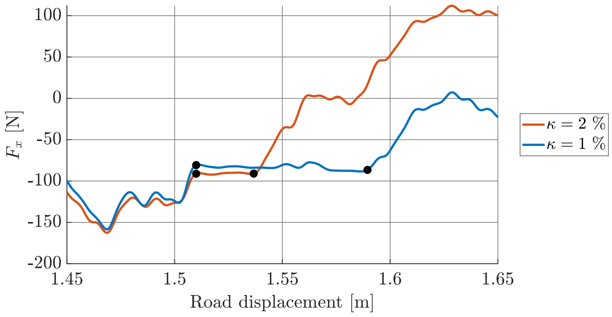

Figure 6.7: The longitudinal force responses for $\kappa = 1$ % and $\kappa = 2$ % as a function of road displacement. The black dots indicate the start and end of the road displacement where the force is approximately constant.

A limitation is encountered during measurements where $\kappa = 1\%$ since a stable force level is not reached within the available length of the plank. This is the result of the slower transient tire response when the applied slip is lower. Van Blijderveen [2] encountered the same issue because the road was covered only for 2.5 m in sandpaper in his case. The road is currently fully covered in sandpaper, however, the actuation delay requires 1.5 m of road displacement to reach steady-state conditions to apply the slip step. As a result, there is 2.7 m of road displacement available for the slip measurements, introducing almost the same limitation as in the study of Van Blijderveen [2]. The limitation indicates that it would be advantageous to apply the slip step directly at or shortly after the start of the plank displacement actuation. This requires the tire to start directly at free-rolling conditions, which can be achieved by implementing the plank displacement actuation in the updated software.

Vertical Force Variation

Figure 6.8 shows the longitudinal force response for the three vertical forces $F_z = [F_{z1},\ F_{z2},\ F_{z3}]$ for $\kappa = 5$ %. The longitudinal force responses are shown starting from 1.5 m of road displacement, where the longitudinal slip step is applied. This is done for all subsequent figures where the transient response is depicted. The initial 1.5 m of road displacement is required to obtain free-rolling conditions and is not relevant in the discussion of the results. It is seen that increasing the vertical force on the tire increases the longitudinal force that the tire develops for the same longitudinal slip value. The positive correlation between the vertical force and longitudinal force is consistent with experimental evidence and available theory [1, 35]. Additionally, the figure shows that increasing the vertical force makes the transient response slower. This is consistent with the effect of the vertical force on the lateral transient response [1]. The measurements with lower slip values and higher vertical forces do not reach steady-state conditions before the maximum road displacement is reached as a result of the slower response. The limitation is shown in Figure 6.9, where the force responses for $\kappa = 1$ % are visualized.

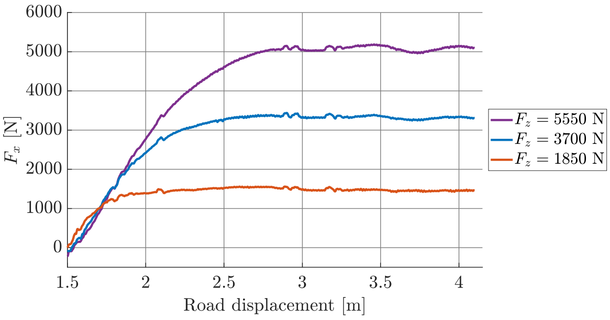

Figure 6.8: The longitudinal tire force plotted against the road displacement for $\kappa = 5$ % and three levels of vertical force.

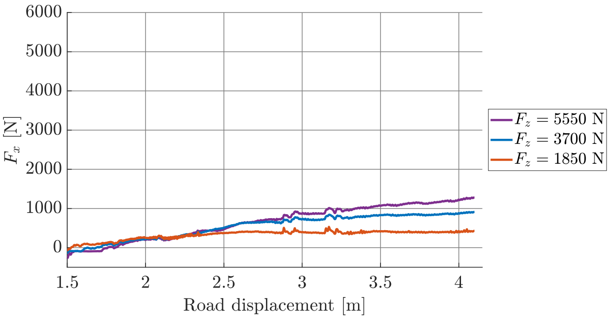

Figure 6.9: The longitudinal tire force plotted against the road displacement for $\kappa = 1$ % and three levels of vertical force.

Tire Inflation Pressure Variation

The influence of the tire inflation pressure on the longitudinal force response is shown in Figure 6.10, where can be observed that lowering the tire inflation pressure leads to an overall higher force magnitude for the given slip level of 5 %. This result is in accordance with the experimental results of Schmeitz et al. [35] and the theory of Pacejka [1]. This observation holds for all slip values except $\kappa = \pm 10$ %. The force response for $\kappa = 10$ % is shown in Figure 6.11, where the maximum longitudinal force for both tire inflation pressures becomes approximately equal. The maximum longitudinal force is dominated by the peak friction coefficient for higher slip values. Schmeitz et al. [35] show that almost all tested tires exhibit a peak longitudinal friction at a certain tire inflation pressure. The longitudinal slip level where the peak friction occurs is dependent on the tire and its operating conditions. Additional measurements are required to determine the longitudinal slip and inflation pressure that yield the highest friction. It should be noted that the experiments from Schmeitz et al. [35] are performed at higher velocities, where the thermal effects influence the results. The thermal effects during Flat Plank measurements are negligible due to the extremely low speed of the machine.

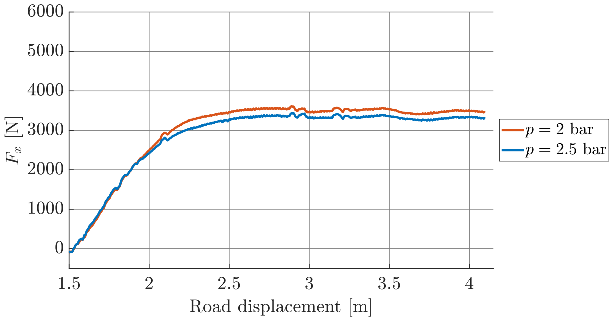

Figure 6.10: Longitudinal force response as a function of road displacement since a longitudinal slip step of 5 % has been applied, for the Toyo tire with a tire inflation pressure of 2 bar and 2.5 bar.

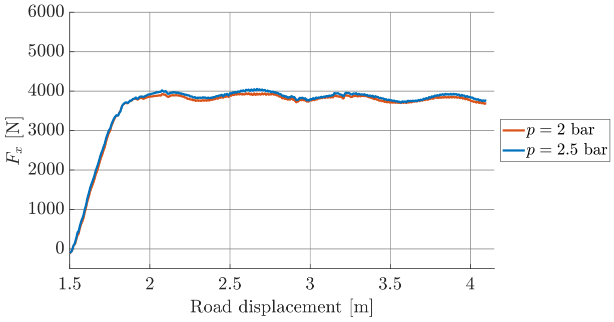

Figure 6.11: Longitudinal force response as a function of road displacement since a longitudinal slip step of 10 % has been applied, for the Toyo tire with a tire inflation pressure of 2 bar and 2.5 bar.

Side Slip Angle Variation

The combined slip results for $\kappa = 5$ % are shown in Figure 6.12, where four distinct levels of longitudinal force are seen for the four side slip angles. The lateral tire force is shown in Figure 6.13. The side slip angle is applied before the tire is vertically loaded. This means that the tire generates a lateral force and the contact patch is thus deformed when the longitudinal slip step is applied. A small lateral force is generated for $\alpha = 0°$. This is due to the free play in the steering mechanism, as discussed in Chapter 3.

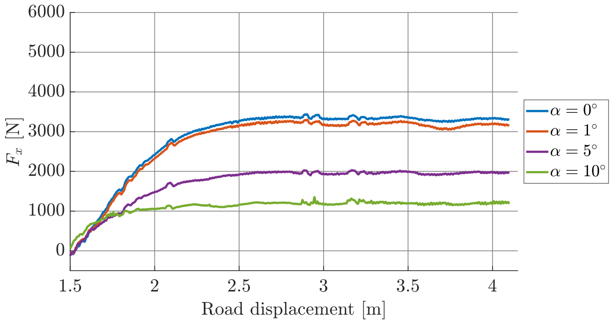

Figure 6.12: Longitudinal force as a function of road displacement since a longitudinal slip of 5 % has been applied, for four side slip angles.

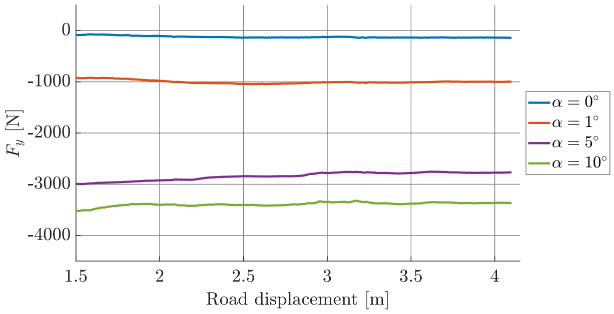

Figure 6.13: Lateral force as a function of road displacement since a longitudinal slip of 5 % has been applied, for four side slip angles.

The developed longitudinal and lateral forces during combined slip are limited by the friction ellipse. As a result, the increase in side slip angle limits the longitudinal force that can be developed. Similarly, the introduction of the longitudinal slip levels impacts the lateral force. The longitudinal slip stiffness and peak friction decrease with increasing side slip angle, which means the tire can only generate a smaller longitudinal force in comparison to the pure longitudinal slip measurement [1].

Increasing the side slip angle results in the transient response reaching steady state within a shorter road displacement. This is due to the decreasing longitudinal slip stiffness and peak friction for increasing side slip angle. A transient phase can be seen in the lateral force response when the longitudinal slip step for the larger side slip angles.

Camber Angle Variation

Figure 6.14 and Figure 6.15 depict the longitudinal force response of $\kappa = 5$ % and $\kappa = -5$ %, respectively, for $\gamma = 0°$ and $\gamma = 5°$. The steady-state force magnitudes remain approximately equal for both positive and negative longitudinal slip steps when the camber angle is increased. Increasing the camber angle appears to have no effect on the transient response.

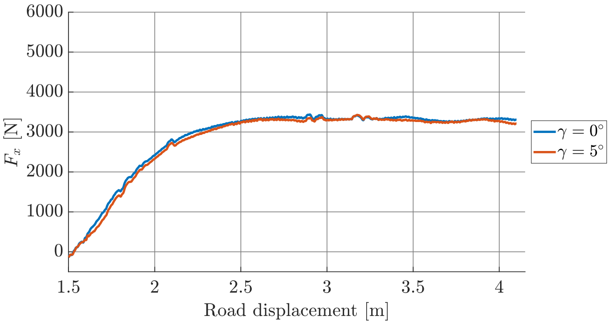

Figure 6.14: Longitudinal force as a function of road displacement since a longitudinal slip step of 5 % has been applied, for two camber angles.

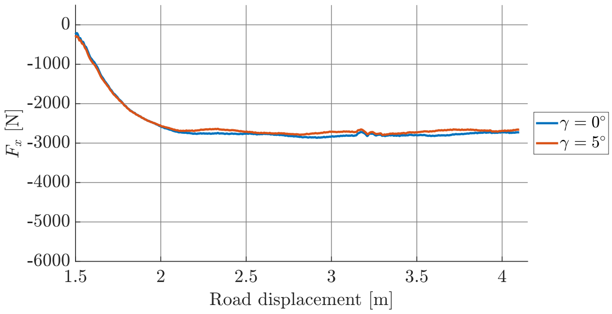

Figure 6.15: Longitudinal force as a function of road displacement since a longitudinal slip step of -5 % has been applied, for two camber angles.

An interesting effect occurs for the lateral force. The lateral force is shown in Figure 6.16 and Figure 6.17 for $\kappa = 5$ % and $\kappa = -5$ %, respectively. The tire develops a negative lateral force, since a positive camber angle shifts the F_y-α curve downwards. A small lateral force is generated for $\gamma = 0°$, which is due to the free play in the steering mechanism. The lateral force for $\gamma = 5°$ increases upon the application of a positive longitudinal slip value, where it becomes positive if $\kappa \geq 5$ %.

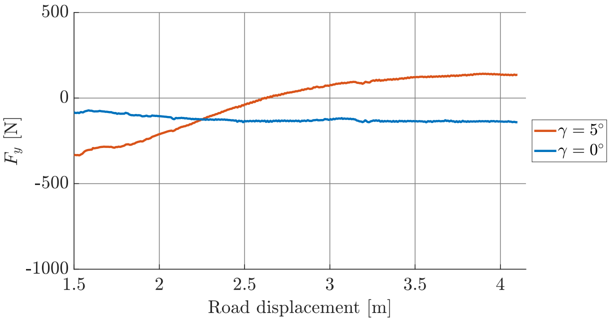

Figure 6.16: Lateral force as a function of road displacement since a longitudinal slip step of 5 % has been applied, for two camber angles.

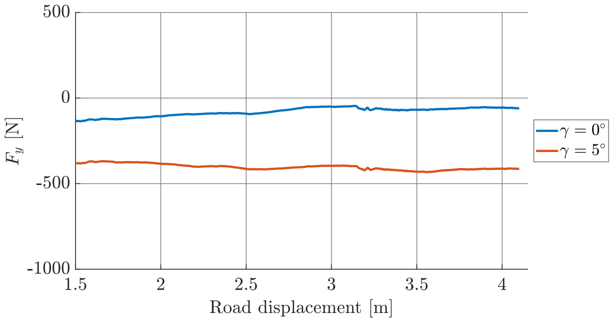

Figure 6.17: Lateral force as a function of road displacement since a longitudinal slip step of -5 % has been applied, for two camber angles.

The influence of camber on the longitudinal response of the combined slip measurements is visualized in Figure 6.18 and Figure 6.19 for $\kappa = 5$ % and $\kappa = -5$ %, respectively. The figures show that the influence of camber for positive slip values is small and higher for negative slip values. The differences between the longitudinal force responses for $\gamma = 0°$ and $\gamma = 5°$ decrease with increasing side slip angle.

The lateral force responses during combined slip for $\kappa = 5$ % and $\kappa = -5$ % are given in Figure 6.20 and Figure 6.21, respectively. It is seen that introducing a camber angle results in a larger force magnitude, which is due to the shift in the F_y-α curve. Similar behavior as for pure longitudinal slip is seen for $\alpha = 1°$ and $\alpha = 5°$ after the application of a positive longitudinal slip step, as visualized in Figure 6.20. This effect decreases for $\alpha = 10°$. The introduction of a negative longitudinal slip leads to a decrease in the lateral force for higher side slip angles, while it remains approximately constant for lower side slip angles.

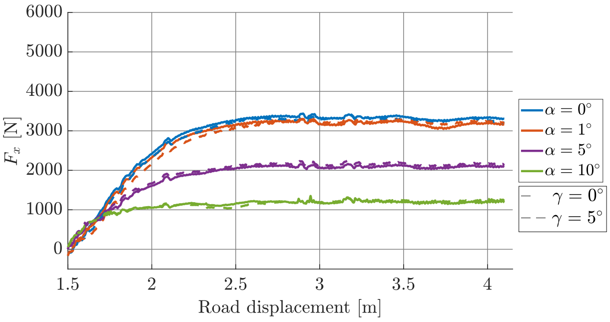

Figure 6.18: Longitudinal force as a function of road displacement since a longitudinal slip step of 5 % has been applied, for two camber angles.

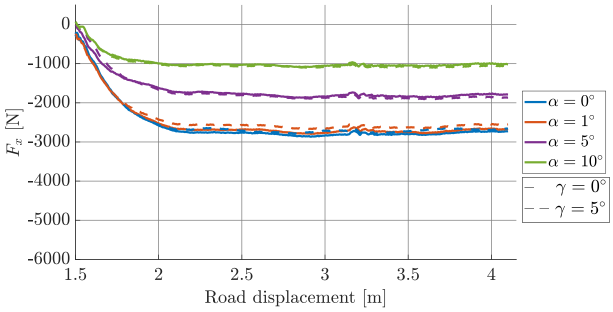

Figure 6.19: Longitudinal force as a function of road displacement since a longitudinal slip step of -5 % has been applied, for two camber angles.

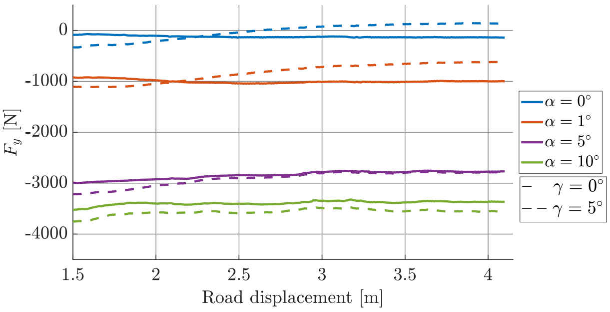

Figure 6.20: Lateral force as a function of road displacement since a longitudinal slip step of 5 % has been applied, for two camber angles.

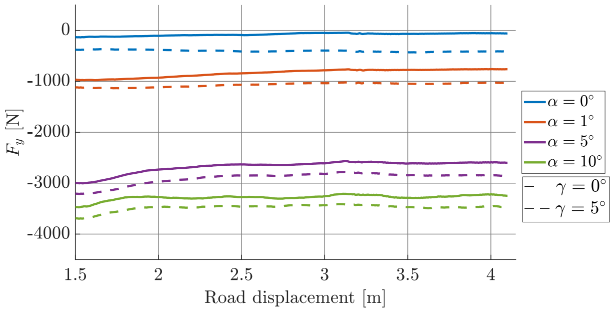

Figure 6.21: Lateral force as a function of road displacement since a longitudinal slip step of -5 % has been applied, for two camber angles.

Repetitions

Measurements for four different operating conditions have been repeated 10 times to investigate the repetitiveness of the force responses. The conditions are repeated below for convenience.

- **Condition 1**: $\kappa = 1$ % and $\alpha = 0°$,
- **Condition 2**: $\kappa = 1$ % and $\alpha = 5°$,
- **Condition 3**: $\kappa = 5$ % and $\alpha = 0°$,
- **Condition 4**: $\kappa = 5$ % and $\alpha = 5°$.

The standard deviation of the longitudinal force after the longitudinal slip step for each plank position is determined. It is normalized with the maximum longitudinal force of the corresponding condition. The results are shown in Figure 6.22. The figure shows that the standard deviation is mostly below 2 % for conditions 3 and 4, where a higher longitudinal slip step is applied. The peak of 6.8 % at 1.84 m of condition 4 is likely due to the sheared-off weld of the rack-and-pinion shaft, as discussed in Chapter 3. These ten measurements are performed on the day the weld sheared off. The build-up of longitudinal force during condition 4 is relatively large. The longitudinal force probably accelerates the plank, which cannot be prevented by the drive shaft due to the damaged weld. The acceleration is observed from the measured road velocity, which spikes at around 1.84 m as shown in Figure 6.23. As a result, the longitudinal force drops around that position. This leads to a peak in the standard deviation since the position where the decrease in force occurs is not exactly equal between the measurements.

The standard deviation is relatively high for conditions 1 and 2 with respect to conditions 3 and 4. This is the result of the normalization. The lower slip value for the first two conditions generates a lower longitudinal force. Lower forces are more susceptible to disturbances, and the lower maximum force means that variations in the longitudinal force are of higher impact on the normalized standard deviation. Additionally, the measurements of condition 2 have been performed on the same day as those of condition 4, meaning that the damage to the weld may influence the measured force response. In absolute terms, the maximum standard deviation for condition 1 is 41 N, 27 N for condition 2, 70 N for condition 3, and 32 N for condition 4. This observation excludes the peak of condition 4, which is due to an exceptional failure of the machine. Therefore, the results indicate that good repeatability is achieved for varying operating conditions. This means that, depending on the specific application, it could suffice to perform only one measurement per operating condition instead of three, effectively reducing the required time to perform measurements.

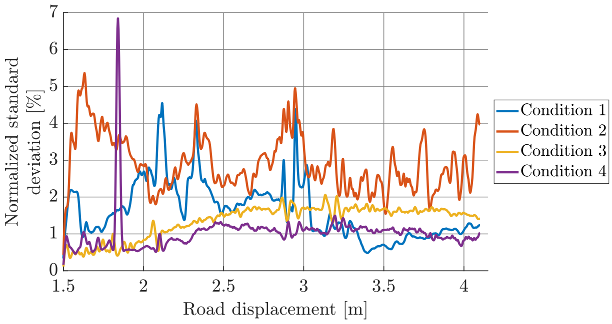

Figure 6.22: Normalized standard deviation as a function of the road displacement since the longitudinal slip step has been applied for the four conditions.

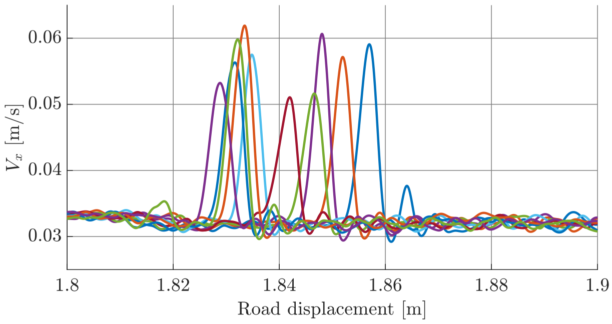

Figure 6.23: The measured road velocity for the ten measurements of condition 4, where it is seen that the velocity spikes around 1.84 m.

6.4 Summary

This chapter presents the measurement results of the Toyo tire. It has been subjected to nine longitudinal slip values under varying operating conditions, which are the vertical force, tire inflation pressure, side slip angle, and camber angle. The results show that the influences of the varying operating conditions on the longitudinal transient behavior are captured. Additionally, the influence of longitudinal slip on the lateral transient behavior is presented. Finally, the repeated measurements for four operating conditions indicate a good repeatability of the process.

Chapter 7

Tire Transient Behavior Modeling

The measurements presented in Chapter 6 are used to identify the parameters of three tire models, to investigate to what extent the models can represent the longitudinal transient behavior, and to determine the influence of the operating conditions on the model parameters. The first two models are the linear transient and nonlinear transient models of Pacejka [1], and the third model is the MF-Tyre/MF-Swift model. The MF-Tyre/MF-Swift model covers a larger operating envelope in comparison to the linear and nonlinear transient model. The linear and nonlinear transient models used in this study purely describe the transient behavior of the tire, and their parameters are directly based on the measured response. In contrast, the MF-Tyre/MF-Swift model not only captures the transient behavior but also steady-state longitudinal and lateral forces, stiffnesses, effective rolling radii, and contact patch dimensions. As a result, the MF-Tyre/MF-Swift model is able to accurately produce general results in a wide range of operating conditions with a single set of parameters, at the cost of somewhat less accuracy when compared with measurements in specific operating conditions.

Similar to Chapter 6, only the results for the Toyo tire are discussed. The given explanations and conclusions also hold for the Continental tire.

7.1 Linear Transient Model

The linear transient model is a single-contact-point model considering carcass compliance. The top view of the model is shown in Figure 7.1. The contact patch is represented by a single point S' which is suspended via a spring from the wheel slip point S, which is attached to the wheel rim. Point S moves with wheel slip velocity V_s with respect to the road surface, and contact patch slip velocity V_s' describes the velocity of point S'.

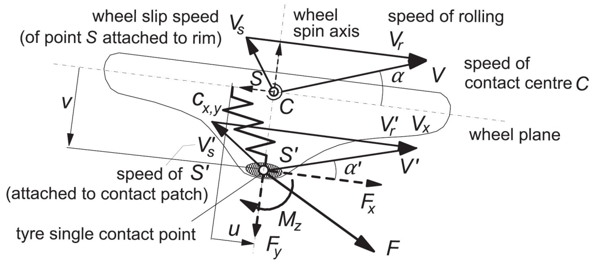

Figure 7.1: Top view of the single-contact-point tire model, showing the longitudinal and lateral carcass deflection. Adapted from [1, Figure 7.1].

The difference in slip velocities results in the longitudinal deflection u. This causes the carcass spring to deflect. The time derivative of the longitudinal deflection is equal to

$$\dot{u} = -\left(V_{sx} - V_{sx}'\right). \tag{7.1}$$

It is assumed that the applied longitudinal slip is in the vicinity of operating point κ_0. This means that the longitudinal force F_x acting from the road to the contact patch is equal to

$$F_x = C_{F\kappa}'\kappa' = -C_{F\kappa}'\frac{V_{sx}'}{|V_x|}, \tag{7.2}$$

where $C'_{F\kappa}$ is the local longitudinal slip stiffness and κ' is the longitudinal slip of the contact patch. The local longitudinal slip stiffness is equal to

$$C'_{F\kappa} = \left.\frac{\partial F_x}{\partial \kappa}\right|_{\kappa_0}. \tag{7.3}$$

Note that $C'_{F\kappa}$ is equal to $C_{F\kappa}$ for $\kappa_0 = 0$ % [14]. The elastic force that is in equilibrium with the longitudinal force is equal to

$$F_x = C_x u, \tag{7.4}$$

where C_x is the longitudinal tire stiffness at road level. The differential equation that governs the longitudinal deflection due to longitudinal slip can be found by equating (7.2) to (7.4), which gives

$$-C'_{F\kappa}\frac{V'_{sx}}{|V_x|} = C_x u. \tag{7.5}$$

Substitution of V'_{sx} using (7.1) and rewriting gives

$$-C'_{F\kappa}\frac{V_{sx}+\dot{u}}{|V_x|} = C_x u, \tag{7.6a}$$

$$-\frac{C'_{F\kappa}}{C_x}\frac{V_{sx}}{|V_x|} - \frac{C'_{F\kappa}}{C_x}\frac{1}{|V_x|}\dot{u} = u, \tag{7.6b}$$

$$\frac{C'_{F\kappa}}{C_x}\frac{1}{|V_x|}\dot{u} + u = -\frac{C'_{F\kappa}}{C_x}\frac{V_{sx}}{|V_x|}. \tag{7.6c}$$

Rewriting (7.6c) using longitudinal relaxation length σ_x, which is equal to

$$\sigma_x = \frac{C'_{F\kappa}}{C_x}, \tag{7.7}$$

and the longitudinal slip κ, given by

$$\kappa = \frac{-V_{sx}}{|V_x|}, \tag{7.8}$$

results in

$$\frac{\sigma_x}{|V_x|}\dot{u} + u = \sigma_x \kappa. \tag{7.9}$$

Transforming (7.9) to the Laplace domain provides the transfer function from κ to u:

$$u(s) = \frac{\sigma_x}{\frac{\sigma_x}{|V_x|}s + 1}\kappa(s). \tag{7.10}$$

Substitution of u using (7.4) and rewriting using the definition of the σ_x leads to the first-order transfer function from κ to F_x, which is equal to

$$F_x(s) = \frac{C'_{F\kappa}}{\frac{\sigma_x}{|V_x|}s + 1}\kappa(s). \tag{7.11}$$

A step in longitudinal slip is applied to the tire during the measurements. It is assumed that the road velocity is constant and the longitudinal slip step κ_{act} is the average longitudinal slip value determined during post-processing.

The two model parameters σ_x and $C'_{F\kappa}$ are identified by minimizing the error between the measured and modeled longitudinal force response, F_{meas} and F_{model}, respectively. F_{model} is the result of applying the first order filter (7.11) to the average slip step κ_{act} of the experiment. The error e is defined as

$$e = \sum_{i=1}^{N}\left(F_{meas,i} - F_{model,i}\right)^2, \tag{7.12}$$

where N is the number of data samples. The error is minimized using `fmincon` in MATLAB, where the initial values for the two parameters are $\sigma_{x,0} = 0.1$ m and $C'_{F\kappa,0} = 10^4$ N. Obviously, the parameters for $\kappa = 0$ % are not determined, and the modeled force response is equal to the average of the measured response. It is important to note that the model parameters are identified for each measurement individually, since the linear transient model assumes a constant value of the local slip stiffness in the vicinity of operating point κ_0. This operating point is different between the different measurements conducted at different levels of slip.

The steady-state longitudinal force of a measurement is defined as the maximum value of the corresponding modeled response. The steady-state force for $\kappa = 0$ % is determined by averaging the longitudinal force after the slip step is applied.

Nominal Results

The measurement and model results for the Toyo tire at nominal conditions are depicted in Figure 7.2. The model accurately matches the measurements for low values of longitudinal slip, for both the transient and the steady-state response. The model cannot represent the measured transient response for higher steps of slip due to the assumption of operation in the vicinity of κ_0. The steady-state results for higher steps of slip do conform with the measured result. This conclusion is supported by the root-mean-square error (RMSE). The RMSE is determined for the transient part of the response. The transient part of the response is defined as the force response up until the point where the gradient of the response, normalized with the steady-state longitudinal force, becomes smaller than 0.05. The RMSE per slip value is given in Table 7.1, where it is seen that the RMSE increases with increasing slip magnitude.

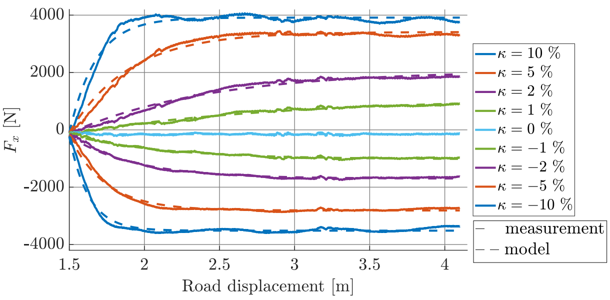

Figure 7.2: Measurement and model response for the Toyo tire at its nominal conditions.

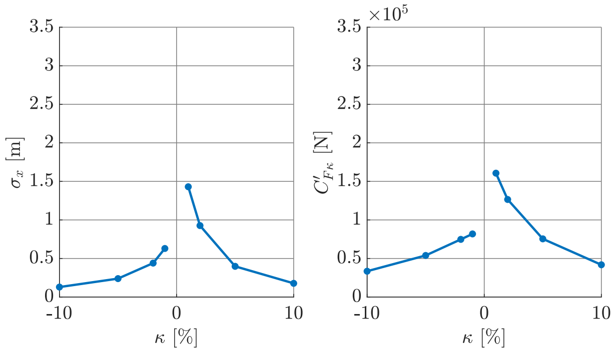

Figure 7.3: Identified longitudinal relaxation length and longitudinal slip stiffness for the Toyo tire at its nominal conditions using the linear transient model.

The identified parameters are depicted in Figure 7.3, which shows a significant difference between the model parameters for positive longitudinal slip and negative longitudinal slip for small values of slip. The suspected reason is a free play of 1.15 mm in the x-direction between the road and the plank structure. The tire is momentarily locked when the measurement starts, leading to a quick growth of negative force as visualized in Figure 6.3. As a result, the road is pushed against one side and the play is eliminated on that side. The build-up of positive longitudinal force moves the road through the play, which has been verified by means of a dial gauge. It is expected that the road does not move through the play for negative slip values since the longitudinal force does not become positive. This results in a smaller relaxation length.

Table 7.1: Root-mean-square error of the linear model for the Toyo tire under nominal conditions.

$\boldsymbol{\kappa}$ [%]	**-10**	**-5**	**-2**	**-1**	**0**	**1**	**2**	**5**	**10**
RMSE [N]	154	92	41	33	24	41	88	152	270

Additional measurements have been performed where the play is reduced to 0.05 mm to verify the hypothesis. The results are given in Figure 7.4, where the forces are vertically shifted to start from 0 N to be able to directly compare the force growth. Especially the responses for $\kappa = 1$ % and $\kappa = 2$ % are significantly affected. The model results for the measurements with the reduced longitudinal play are shown in Figure 7.5. It can be seen that the model response for $\kappa = 1$ % and $\kappa = 2$ % better match the measured response compared to the model results without the reduced longitudinal play. The model parameters identified before and after the reduction of the longitudinal play are displayed in Figure 7.6. It is seen that the longitudinal play influences the model parameters due to the change in force growth, which results in a decrease in the difference between the parameters for negative and positive slip values. Unfortunately, all measurements have been performed before the play was reduced, which means that each measurement exhibits this phenomenon. Nevertheless, both results clearly show that the relaxation length and longitudinal slip stiffness decrease with increasing values of longitudinal slip.

The steady-state longitudinal force $F_{x,ss}$ versus longitudinal slip κ curve is shown in Figure 7.7 for the measurement before the reduction of the longitudinal play. The steady-state response might be less accurate for low levels of slip since the slower transient response did not allow to fully reach steady-state conditions in the available road displacement.

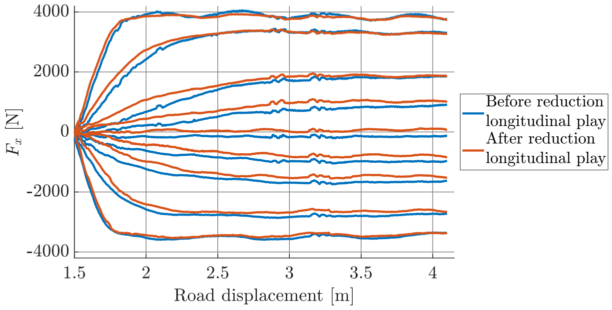

Figure 7.4: Measured response before and after the reduction of longitudinal play for the Toyo tire at nominal conditions. Note that the responses have been vertically shifted to start from 0 N and the longitudinal slip values are not indicated.

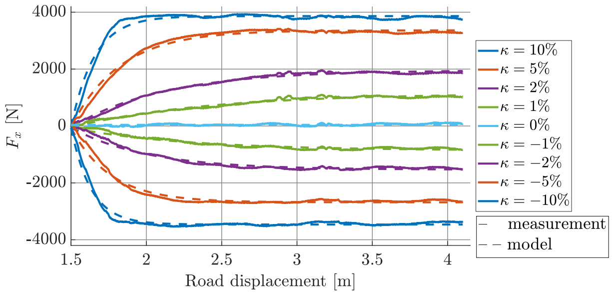

Figure 7.5: Measurement and model response for the Toyo tire at its nominal conditions, where the longitudinal play has been reduced to 0.05 mm.

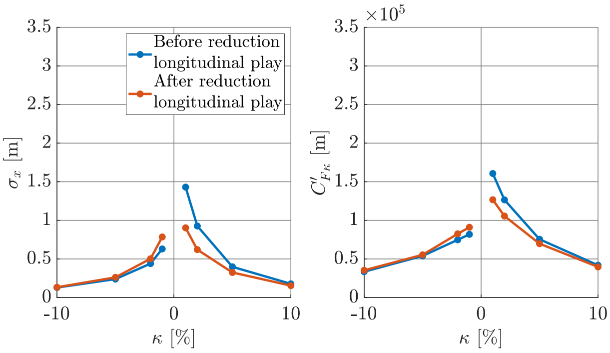

Figure 7.6: Identified model parameters before and after the reduction of the longitudinal play between the road and plank structure.

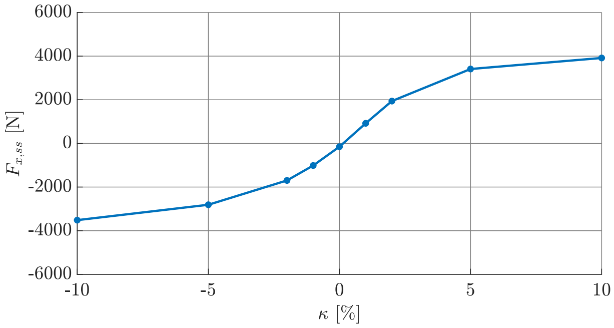

Figure 7.7: Steady-state F_x-κ curve for the Toyo tire under nominal conditions.

Vertical Force Variation

The influence of the vertical force on the longitudinal transient parameters at nominal tire inflation pressure is depicted in Figure 7.8, where it is seen that σ_x and $C'_{F\kappa}$ increase with increasing vertical force, as expected. Increasing the vertical force leads to a larger contact length. The longitudinal slip stiffness is proportional to the square of the half contact patch length according to the tire brush model [1]. As a result, the slip stiffness increases with increasing vertical force. The relaxation length increases due to the increasing slip stiffness, as (7.7) indicates. This also means that the increase in longitudinal slip stiffness is higher than the marginal increase in longitudinal tire stiffness with increasing vertical force. Figure 7.9 visualizes σ_x and $C'_{F\kappa}$ for $\kappa = -1$ % and $\kappa = 1$ % as a function of F_z. It is seen that both exhibit a linear relation with the vertical force, where the slope magnitude depends on the sign of the longitudinal slip value. The difference in the slope that is observed between the negative and positive slip conditions is presumably due to the asymmetry that arises from the longitudinal play, as explained in Chapter 3.

Tire Inflation Pressure Variation

The longitudinal relaxation length and slip stiffness for the two tire inflation pressures are shown in Figure 7.10. The lower inflation pressure results in a higher longitudinal slip stiffness for $|\kappa| \leq 5$ % and the characteristics are approximately equal for $|\kappa| = 10$ %. This is the result of the longitudinal peak friction value, which becomes increasingly dominant for higher slip values. The decrease in inflation pressure leads to an increasing contact length, resulting in higher slip stiffness according to the brush model. The relaxation length increases due to the increasing slip stiffness. The longitudinal tire stiffness moderately increases with increasing inflation pressure compared to the increase in slip stiffness. The steady-state force curve is given in Figure 7.11. The figure shows that the pressure has a low influence on the peak friction since the steady-state forces become approximately equal for $|\kappa| = 10$ %. It is expected that peak friction lies beyond the presented results. No conclusions are drawn on the relation between the model parameters and inflation pressure since only two pressures are tested, which is insufficient.

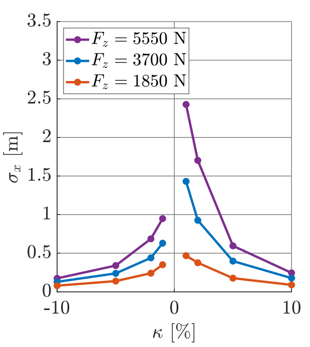

Figure 7.8: Identified model parameters for varying vertical force at nominal tire inflation pressure.

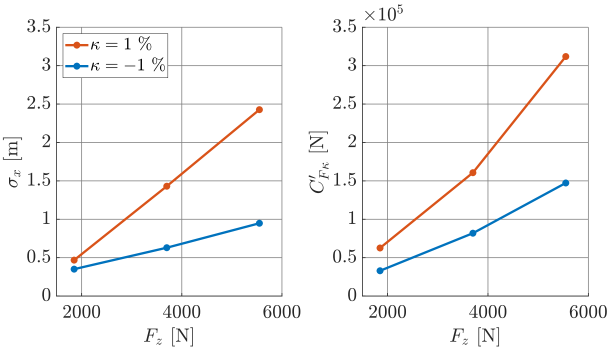

Figure 7.9: Identified model parameters for $\kappa = -1$ % and $\kappa = 1$ % as a function of the vertical force at nominal tire inflation pressure.

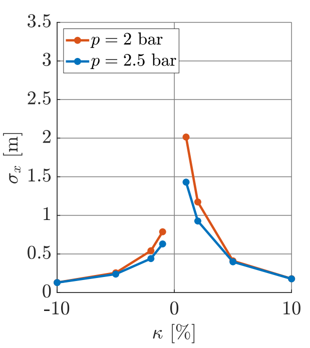

Figure 7.10: Identified model parameters for varying inflation pressure at nominal vertical force.

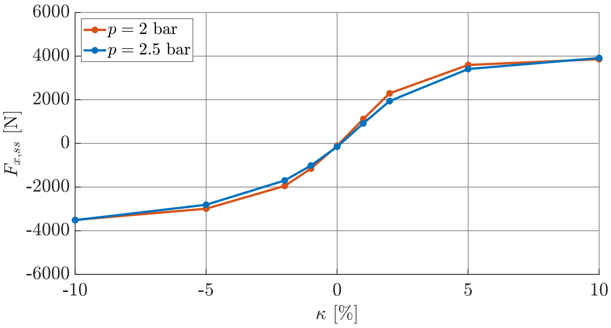

Figure 7.11: Steady-state $F_{x,ss}$-κ curve for varying inflation pressure at nominal vertical force.

Side Slip Angle Variation

The influence of the side slip angle on the model parameters is visualized in Figure 7.12, the steady-state curves are shown in Figure 7.13. A small increase in the side slip angle shows a slight increase in the model parameters for low positive longitudinal slip, while larger side slip angles result in a decrease of σ_x, $C'_{F\kappa}$, and $F_{x,ss}$. The increase in model parameters could be due to the play in the steering mechanism, as explained in Chapter 3. Additionally, it is suspected that the play between the rotation support and the half-moon guide influences the lateral force generation, similar to the influence of the play between the road and plank structure on the longitudinal force generation. Additional research is required to draw further conclusions. The behavior for larger side slip angles is due to the fact that the longitudinal and lateral forces are limited by the friction ellipse during combined slip conditions. The reduction in steady-state longitudinal force leads to a decrease in relaxation length, since the tire needs to deform less to reach the steady-state value. Figure 7.14 depicts the $F_{y,ss}$-α curve. The introduction of longitudinal slip reduces the steady-state lateral force. This is due to the friction ellipse limiting the force generation during combined slip.

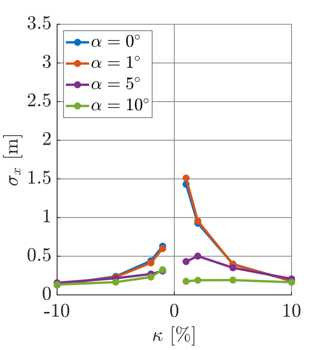

Figure 7.12: Identified model parameters for varying side slip angle.

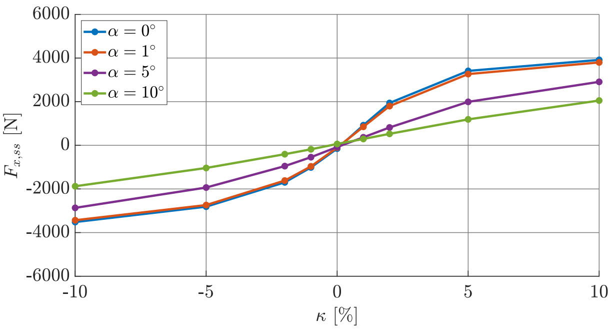

Figure 7.13: Steady-state $F_{x,ss}$-κ curve for varying side slip angle (combined slip).

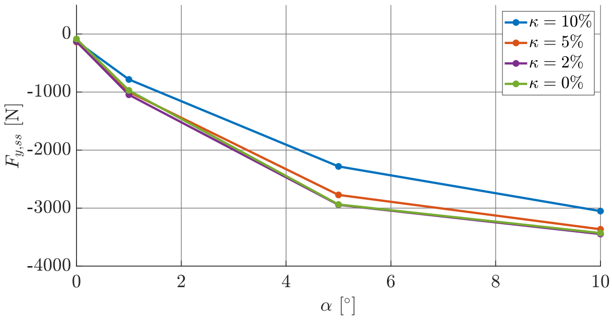

Figure 7.14: Steady-state $F_{y,ss}$-α curve for varying longitudinal slip values (combined slip).

The $F_{x,ss}$-κ curve shows that the linearity of the curve increases with the increasing side slip angle. Consequently, the linear model is also capable to represent the response for higher slip values. Figure 7.15 depicts the longitudinal force response of the measurement and model for $\alpha = 10°$ for the Toyo tire, where it is seen that the model accurately matches the measurement results.

The relation between the model parameters and the side slip angle is visualized in Figure 7.16. The parameters seem to have a monotonically decreasing relationship with the side slip angle, except for $\alpha = 0°$ and $\kappa = 1$ %. As mentioned before, it is currently not possible to draw a conclusion on this relation due to the issues in the measurement setup.

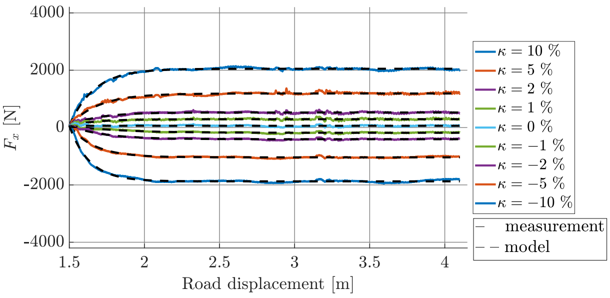

Figure 7.15: Measurement and model response for the Toyo tire at its nominal conditions for $\alpha = 10°$. The model results are colored in black to distinguish the measurement and model results.

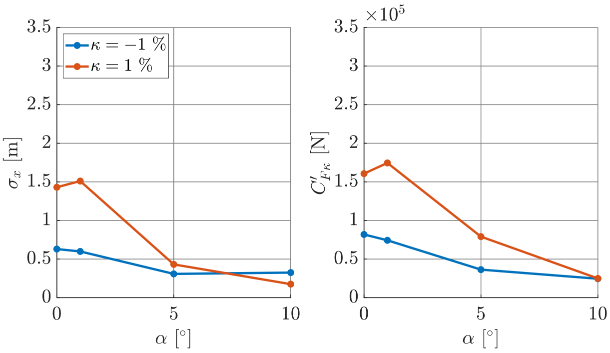

Figure 7.16: Identified model parameters for $\kappa = -1$ % and $\kappa = 1$ % as a function of the side slip angle at nominal vertical force and tire inflation pressure.

Camber Angle Variation

The identified model parameters are shown in Figure 7.17 for $\gamma = 0°$ and $\gamma = 5°$, the $F_{x,ss}$-κ curve is given in Figure 7.18. The results show that the difference in relaxation length is insignificant for $\kappa \leq -2$ % and $\kappa > 5$ %. A positive camber angle results in a lower $C'_{F\kappa}$ for negative slip values and higher stiffness for positive slip. The difference in the steady-state force curves is negligible.

The influence of camber on the parameters for the combined slip results is shown in Figure 7.19. It is seen that the observations for the pure slip condition also hold for the combined slip conditions, except for $\alpha = 5°$. The opposite is true for this case, where the longitudinal relaxation length and slip stiffness increase for negative slip and decrease for positive slip. The steady-state $F_{x,ss}$-κ curves are shown in Figure 7.20. It can be seen that the influence of the camber angle on the steady-state values is insignificant, except for $\alpha = 5°$ and $\kappa > 0$ %. The reasoning behind this behavior is outside the scope of this project. Furthermore, no conclusions are drawn on the relation between the model parameters and camber since only two camber angles are tested.

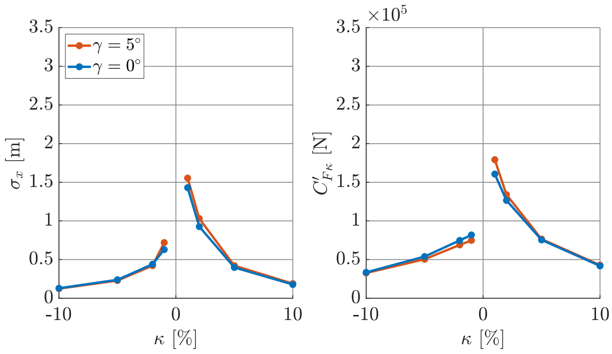

Figure 7.17: Identified model parameters for varying camber angle.

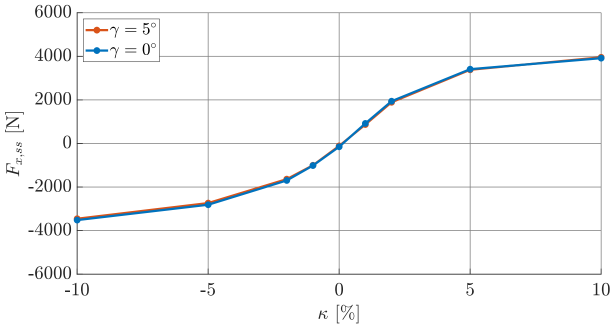

Figure 7.18: Steady-state $F_{x,ss}$-κ curve for varying camber angle.

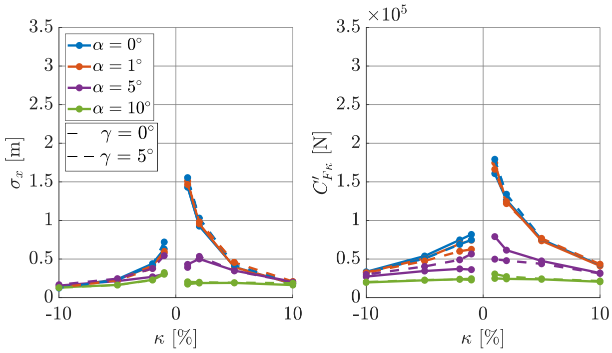

Figure 7.19: Identified model parameters for varying camber and side slip angle.

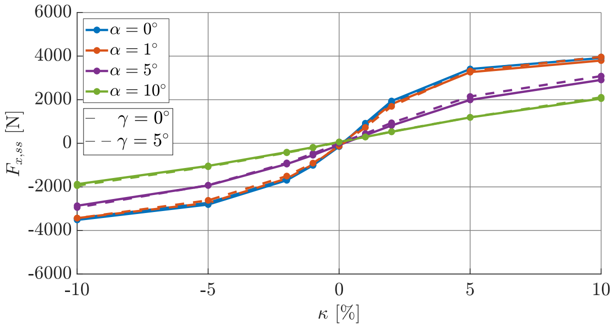

Figure 7.20: Steady-state $F_{x,ss}$-κ curve for varying camber and side slip angle (combined slip).

7.2 Nonlinear Transient Model

The linear transient model is a model that can describe the transient response of the tire for small values of longitudinal slip, but fails to do so for higher steps of slip. The nonlinear transient model separates the contact patch slip properties and carcass compliance. and accounts for the nonlinear slip characteristics for larger slip values [1]. This means that the nonlinear transient model can represent the transient response for both low and high slip values.

The nonlinear model consists of differential equations to model the mass-spring-damper system that represents the tire contact patch dynamics. Additionally, a contact patch relaxation length model is used to account for the transient response of the contact patch due to the finite contact patch length and to allow calculations near or at standstill [1, 5]. A schematic view of the nonlinear transient tire model for the longitudinal dynamics is shown in Figure 7.21.

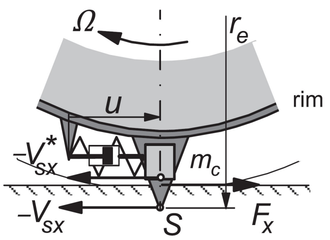

Figure 7.21: Side view of the transient tire model, showing the contact patch mass and carcass compliances. Adapted from [1, Figure 7.15].

The inputs of the model are the road velocity V_x, defined in the wheel plane, and the sliding velocity V_{sx} of the rim equal to

$$V_{sx} = V_x - r_e\omega_T, \tag{7.13}$$

where ω_T is the rotational velocity of the wheel. The equation of motion of the contact patch is given by

$$m_c \dot{V}_{sx}^* + k_{cx}\dot{u} + c_{cx}u = F_{x,ss}(\kappa', \alpha, \gamma, F_z, p), \tag{7.14}$$

where m_c is the contact patch mass, V_{sx}^* is the sliding velocity of the contact patch, u is the longitudinal deflection, c_{cx} is the longitudinal carcass stiffness, k_{cx} is the longitudinal carcass damping, and κ' is the longitudinal slip of the contact patch. $F_{x,ss}(\kappa', \alpha, \gamma, F_z, p)$ is a look-up table based on the steady-state curves. The deflection rate of the damper is given by

$$\dot{u} = V_{sx}^* - V_{sx}. \tag{7.15}$$

The relaxation behavior of the contact patch is modeled using a first-order differential equation, which provides the transient slip quantity κ'. This relaxation model [5] is equal to

$$\sigma_c \dot{\kappa}' + |V_x|\kappa' = -V_{sx}^*, \tag{7.16}$$

where σ_c is the relaxation length of the contact patch. The contact patch relaxation length is given by

$$\sigma_c = \frac{m(\kappa')a}{1+\kappa'}, \tag{7.17}$$

where m defines the fraction of the contact patch where adhesion occurs and a is half of contact length. This approach incorporates the diminishing relaxation length for increasing values of slip [1]. The coefficient m is defined by

$$m(\kappa') = \begin{cases} 1 - \theta\frac{|\kappa'|}{1+\kappa'} & \frac{|\kappa'|}{1+\kappa'} < \frac{1}{\theta}, \\ 0 & \text{otherwise,} \end{cases} \tag{7.18}$$

where θ is given by

$$\theta = \frac{2c_{px}a^2}{3\mu F_z}, \tag{7.19}$$

where c_{px} is the stiffness of the tread elements per unit length and μ is the friction coefficient. Fraction m has a lower limit of 0.01 to prevent vibration modes during simulations. Half the contact length a is dependent on the vertical force and tire inflation pressure and is determined using the empirical relation given by

$$a = r_0 \left(q_{ra2}\frac{F_z}{C_z r_0} + q_{ra1}\sqrt{\frac{F_z}{C_z r_0}} \right), \tag{7.20}$$

where r_0 is the free tire radius, C_z is the vertical stiffness and q_{ra1} and q_{ra2} are contact patch model parameters. The vertical stiffness is equal to

$$C_z = C_{z0}(1 + p_{Fz1}d_{pi}), \tag{7.21}$$

where C_{z0} is the vertical stiffness at nominal vertical force and tire inflation pressure, p_{Fz1} is a contact patch model parameter, and d_{pi} is the normalized pressure difference with respect to the nominal pressure. The normalized pressure difference is given by

$$d_{pi} = \frac{p - p_0}{p_0}. \tag{7.22}$$

Parameter Identification

Similar to the linear transient model parameters, the nonlinear model parameters are determined by minimizing the error between the measurement and model response. This approach determines only one parameter set per operating condition. The nonlinear transient model includes the dependency of the transient response on the slip level, so a single set of model parameters can capture the nonlinear phenomena. The model parameter that is determined is the carcass stiffness c_{cx}. It is difficult to identify the carcass damping since the transient response is not very sensitive to this parameter in the frequency range in which the tire operates during the measurements. Therefore, it assumed that k_{cx} is equal to

$$k_{cx} = t_{kcx}c_{cx}. \tag{7.23}$$

where t_{kcx} is the longitudinal carcass damping coefficient equal to 0.01 s. The known model parameters are given in Table 7.2. The contact patch mass is estimated without any further identification approach, which is valid due to the slow operating speed of the machine. The nominal vertical stiffness and the q_{ra1}, q_{ra2}, and p_{Fz1} parameters are identified using the measurement results given in Appendix G. The steady-state force $F_{x,ss}$ is dependent on the operating conditions, and the $F_{x,ss}$-κ lookup-table corresponding to the operating condition is used in the simulation. The effective rolling radius per operating condition is selected from a lookup-table corresponding to Figure 6.1 and Figure 6.2. The tread element stiffness is determined using the brush model [1, (3.27)]. The friction coefficient per operating condition is calculated by dividing the steady-state longitudinal force for $|\kappa| = 10$ % by the vertical force for the pure longitudinal slip conditions. The friction coefficient per tire is then determined by averaging the friction coefficient per the operating condition of that tire.

Table 7.2: Nonlinear model parameters of both tires.

	Toyo NanoEnergy	**Continental EcoContact**
m_c [kg]	1	1
r_0 [m]	0.318	0.350
c_{px} [N]	$1.70 \cdot 10^7$	$1.46 \cdot 10^7$
μ [-]	0.993	0.954
q_{ra1} [-]	0.924	0.877
q_{ra2} [-]	0.120	0.456
C_{z0} [N/m]	$2.13 \cdot 10^5$	$2.41 \cdot 10^5$
p_{Fz1} [-]	0.8451	0.8598

The model is implemented in MATLAB Simulink. It is assumed that the tire is in steady-state condition at the start of the simulation and the initial conditions are equal to, except the initial condition of u. This is equal to

$$u_0 = \frac{F_{x,ss}(\kappa', \alpha, \gamma, F_z, p)}{c_{cx}}, \tag{7.24}$$

to ensure that the measured and modeled force response start at the same value. The simulation result is used to determine the error per measurement j, which is given by

$$e_{w,j} = \sum_{i=1}^{N} w_i \left(F_{meas,i} - F_{model,i}\right)^2. \tag{7.25}$$

The steady-state part of the measured response increases with respect to the transient part for increasing slip values. As a result, the error becomes increasingly dominated by the steady-state part for higher slip values, while it is desired to model the transient part. Therefore, a weight w_i is introduced in the error calculation to increase the importance of the transient part of the response in the error calculation. The transient part of the response is defined as the force response up until the point where the gradient of the response, normalized with the steady-state longitudinal force, becomes smaller than 0.05. The weight is equal to 100 and 1 for the transient and steady-state parts, respectively. The combined error is equal to

$$e_t = \sum_{j=1}^{M} e_{w,j}, \tag{7.26}$$

where M is the number of longitudinal slip values per operating condition. The total error is minimized using `fmincon` in MATLAB, where the initial value of c_{cx} is set to $2 \cdot 10^5$ N/m.

Results

The transient responses of the measurement and model for the Toyo tire under nominal conditions are depicted in Figure 7.22. The figure shows that the modeled response for high positive and low negative values of slip is fairly accurate, while the model response is less accurate for the other slip values. This tendency is reflected in the RMSE values, which are shown Table 7.3.

The suspected first reason for this result is the influence of the longitudinal play on the transient response. This play influences the transient response for lower, positive slip values the most. This behavior is not included in the nonlinear transient model. Secondly, the c_{cx} value is identified using a set of measurements, rather than per measurement approach used for the linear model. Therefore, the modeled force responses have to match nine measured responses with one variable parameter. This conclusion is substantiated by Figure 7.23, where the measured and modeled transient response is shown for the measurement where the longitudinal play has been reduced. The corresponding RMSE values are given in Table 7.3. Both the figure and RMSE values show that the modeled transient response better matches the measured force, especially for low, positive longitudinal slip values. The accuracy of the response for low, negative slip values is slightly worse due to the constant force part after the application of the longitudinal slip, as explained in Section 6.3. This behavior is present to a greater extent in the measurements where the longitudinal play has been reduced. The measured road velocity is an additional reason that might influence the result. The measured road velocity is provided as a time-dependent input for the nonlinear model, although it is not the actual road velocity. It is actually the rotational velocity of the pinion gear multiplied by the pitch radius, as explained in Chapter 3. However, it is unknown to what extent the measured and actual road velocities differ and no conclusion is drawn on its influence on the model results.

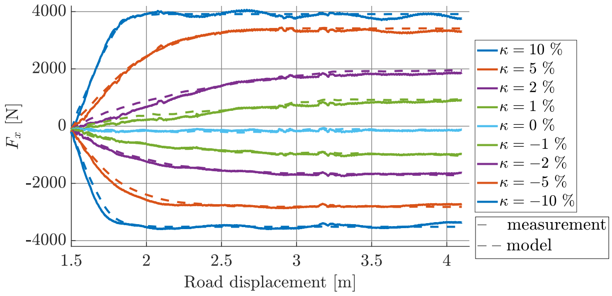

Figure 7.22: Measured longitudinal force response of the Toyo tire at nominal conditions, together with the nonlinear model result.

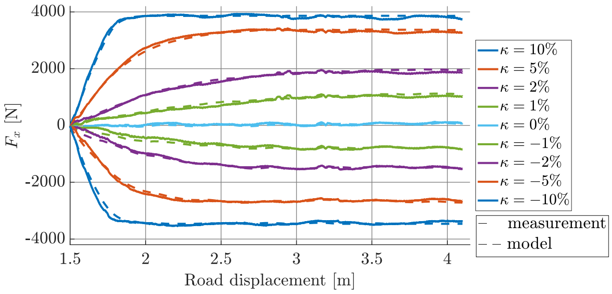

Figure 7.23: Measured longitudinal force response of the Toyo tire at nominal conditions where the longitudinal play has been reduced to 0.05 mm, together with the nonlinear model result.

Table 7.3: RMSE of the nonlinear model for the Toyo tire under nominal conditions, for the measurements before and after the reduction of the longitudinal play.

$\boldsymbol{\kappa}$ [%]	-10	-5	-2	-1	0	1	2	5	10
RMSE [N]	171	139	51	38	43	108	129	78	80
RMSE (reduced longitudinal play) [N]	134	81	64	79	37	67	47	64	66

The model responses for other operating conditions show similar trends in the RMSE in terms of longitudinal slip value dependency. The RMSE values for the other operating conditions are given in Appendix H and the general trends will be discussed here. The RMSE magnitude increases with increasing vertical force. This is the result of the increasing discrepancy between the transient responses for positive and negative slip when the vertical force is raised. The linear model parameters shown in Figure 7.8 substantiate this conclusion since the difference between the positive and negative slip parameters also increases with increasing vertical force. The change in tire inflation pressure and camber do not show a clear trend in the RMSE values. The increase in side slip angle leads to a decrease in the overall RMSE magnitude since the transient response becomes more symmetric for negative and positive slip responses. This is also supported by the linear parameters shown in Figure 7.12 and the force response in Figure 7.15.

Despite some discrepancies, the results of the nonlinear model show that it is capable of representing the measured transient response for both low and high slip values. This allows to identify the structural c_{cx} value of the tire under various operating conditions and investigate the influence of those conditions.

The identified c_{cx} values for the different operating conditions are shown in Figure 7.24. It is seen that the carcass stiffness increases with increasing inflation pressure, which follows from the fact that the tire stiffness increases when the inflation pressure is increased [6]. The carcass stiffness increases for decreasing or increasing vertical force with respect to the nominal vertical force. A side slip angle reduces c_{cx} up to $\alpha = 5°$, whereafter it increases. So, no clear trend is observed. Increasing the camber angle results in a decreasing carcass stiffness. Increasing the side slip angle for combined slip with camber shows a similar trend as for combined slip without camber. A detailed explanation of the influence of the operating conditions on carcass stiffness is outside the scope of this work. A good starting point to begin the research into the reasoning is the book of Clark, specifically, [3, Figure 7.4.1].

The longitudinal relaxation length is determined using the identified carcass stiffness using

$$\sigma_x = \frac{C_{F\kappa}}{C_x} = \frac{C_{F\kappa}}{c_{cx}} + \sigma_c. \tag{7.27}$$

In this case, it assumed that $\sigma_c = a$, as suggested by Pacejka [1]. The influence of this assumption is minor since a is in the range between 0.05 m for F_{z1} to 0.09 m for F_{z3} at nominal pressure. The resulting relaxation length is visualized in Figure 7.25. It is seen that σ_x rises with increasing vertical force. This is due to the clear increase in slip stiffness, visible in Figure 7.9, in comparison to the smaller variation in carcass stiffness. Additionally, a slightly increases for increasing vertical force. The higher tire inflation pressure reduces the relaxation length since a slightly decreases, the slip stiffness decreases, and the carcass stiffness increases for a higher tire inflation pressure. The camber angle influence on the relaxation length is negligible. The side slip angle increase leads to a reduction in relaxation length as a result of the decrease in slip stiffness compared to the smaller change in carcass stiffness. The longitudinal slip stiffness as a function of the side slip angle is displayed in Figure 7.16.

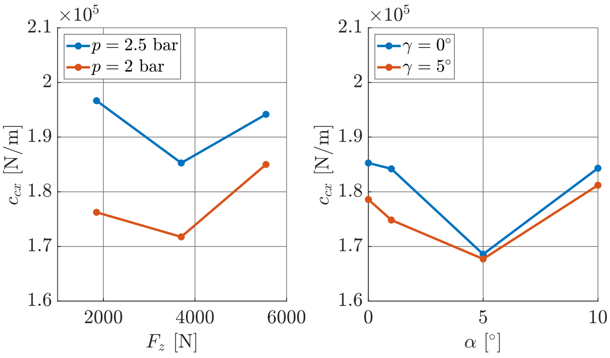

Figure 7.24: Identified carcass stiffness for various operating conditions for the Toyo tire.

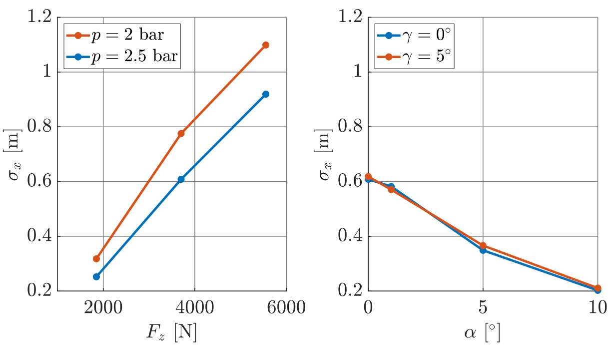

Figure 7.25: Calculated relaxation length using the identified carcass stiffness for the Toyo tire.

7.3 MF-Tyre/MF-Swift Model

The MF-Tyre/MF-Swift model implements the *Magic Formula* of Pacejka and allows for simulating the tire behavior in MATLAB Simulink from steady-state to high-frequency dynamics up to 60-80 Hz. The *Magic Formula* is capable of representing measured steady-state tire behavior based on mathematical, empirical equations. The equations are parameterized by minimizing the error, given in (7.12), between the measured and modeled longitudinal and lateral force. Figure 7.26 shows the resulting steady-state curves for the longitudinal force for three vertical forces at nominal tire inflation pressure as an exemplary result. Similarly, Figure 7.27 depicts the lateral steady-state curve for the Toyo at nominal conditions. In general, the relative error given by

$$e_r = \frac{\sum_{i=1}^{N} |F_{meas,i} - F_{model,i}|}{\sum_{i=1}^{N} |F_{meas,i}|} \cdot 100\ \%, \tag{7.28}$$

is below 10 % for all pure slip operating conditions. The parameters for combined slip are not identified, which means that the MF-Tyre/MF-Swift model estimates these parameters. Next to the steady-state characteristics, the *Magic Formula* parameters that are used in the equations for the vertical stiffness C_z, effective rolling radius r_e, half of contact length a, and overall longitudinal stiffness C_x are identified using the same approach. The resulting model parameters are listed in Appendix I.

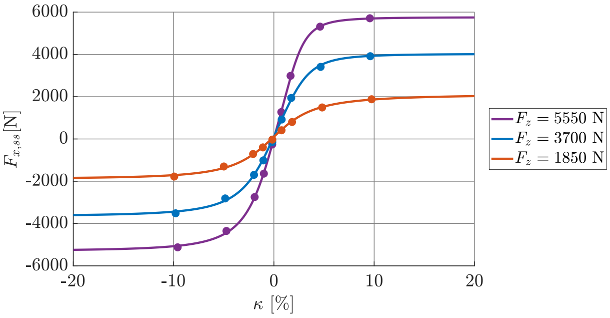

Figure 7.26: Measured steady-state longitudinal forces, indicated with dots, and the fitted *Magic Formula* steady-state curves.

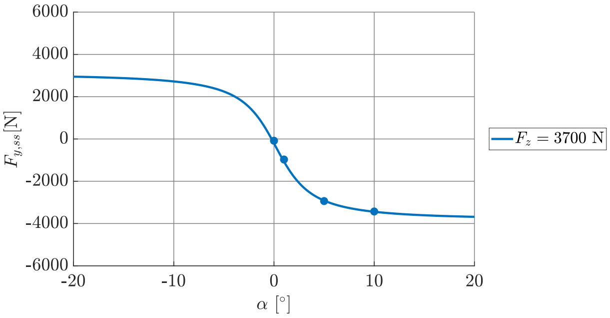

Figure 7.27: Measured steady-state lateral forces, indicated with dots, and the fitted *Magic Formula* steady-state curves.

Simulation Approach

The `contact point interface` (CPI) Simulink block of MF-Tyre/MF-Swift is used to simulate the modeled tire behavior. The block parameters are set to nonlinear dynamics with relaxation behavior and combined slip forces. The measured road velocity, wheel angular velocity, and vertical force are provided to the CPI block. Note that forward velocity in the CPI block is defined at the wheel center in the wheel plane. This means that the measured road velocity has to be multiplied by $\cos(\alpha)$. The lateral wheel slip velocity V_{sy} is determined by

$$V_{sy} = \tan(\alpha) V_x, \tag{7.29}$$

which is supplied to the CPI block as input, together with a constant camber angle. The yaw velocity about the road normal is kept at zero and all scaling factors are equal to one. The simulation is performed for the complete plank displacement to also compare the free-rolling conditions, before the slip step is applied, between the measurement and model.

Results

A zoomed-in section of the measurement and MF-Tyre/MF-Swift model results for the Toyo tire at nominal conditions around the application point of the longitudinal slip step is shown in Figure 7.29. It is seen that the measured and modeled longitudinal force slightly differ for free-rolling conditions due to a small mismatch in the measured and modeled F_x-κ curve for κ in the vicinity of 0°. The measured and modeled transient responses are depicted in Figure 7.28, where it is seen that the model fairly accurately captures the measured transient response for low negative and high positive longitudinal slip values. The longitudinal play of the road influences the measured response for $\kappa = 1$ % and $\kappa = 2$ %, which is the suspected reason for the difference in the measured and modeled response for low positive longitudinal slip values. The reason for the reduced accuracy for higher negative longitudinal slip values is unknown. It is might be caused by the change in vertical force for negative slip values, as has been explained in Section 6.3. However, further research is required to draw a final conclusion. The RMSE values, given in Table 7.4, reflect the observations.

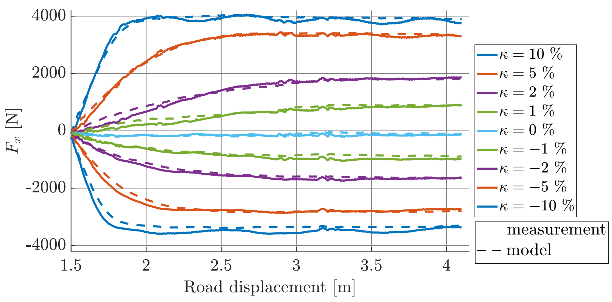

Figure 7.28: Longitudinal force response of the measurement and MF-Tyre/MF-Swift model for the Toyo tire at nominal conditions.

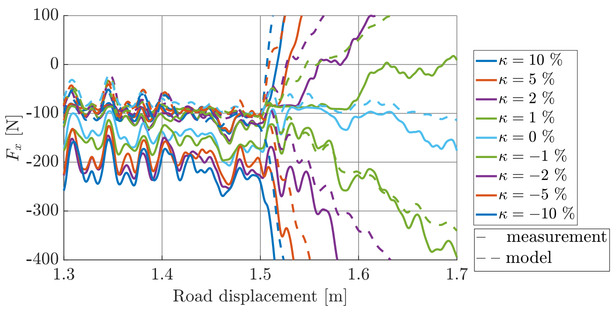

Figure 7.29: Zoomed-in section of Figure 7.28.

Table 7.4: RMSE for the MF-Tyre/MF-Swift model for the Toyo tire under nominal conditions.

$\boldsymbol{\kappa}$ [%]	**-10**	**-5**	**-2**	**-1**	**0**	**1**	**2**	**5**	**10**
RMSE [N]	253	179	87	40	52	101	108	106	116

The RMSE values for the other operating conditions are given in Appendix H and the general trends will be discussed here. Increasing the vertical force increases the RMSE values, especially for negative slip values. The RMSE values remain approximately constant when the tire inflation pressure or camber angle is varied. The RMSE values do not show a clear trend when increasing the side slip angle. Further research is required to draw a conclusion about this behavior. It should be noted that the combined slip parameters are not determined and are consequently estimated by the MF-Tyre/MF-Swift model. It is anticipated that, due to the estimation, differences to a certain degree arise between the measurement and model results for combined slip. Furthermore, the MF-Tyre/MF-Swift model does not incorporate a dependency on the effective rolling radius on the side slip and camber angle. However, the measurement results show that there seems to be a dependency between the two. The measured and modeled effective rolling radii are shown in Figure 7.30 and Figure 7.31.

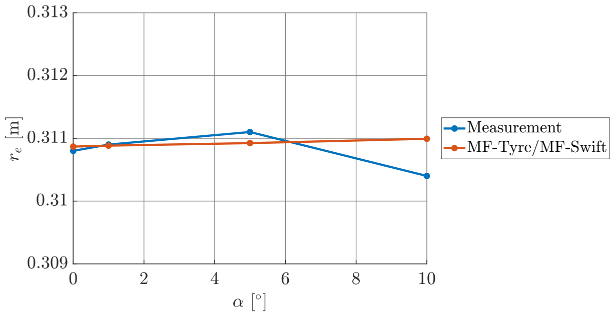

Figure 7.30: Effective rolling radius of the measurement and MF-Tyre/MF-Swift model as a function of side slip angle for the Toyo tire at nominal conditions and a camber angle of 0°.

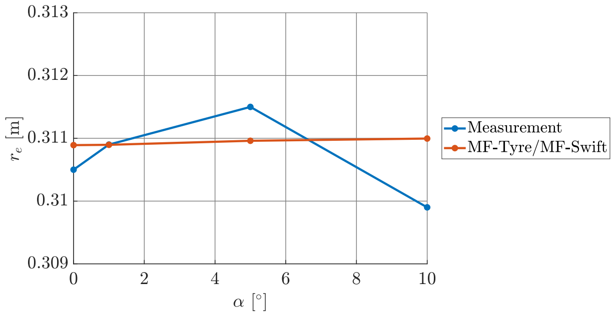

Figure 7.31: Effective rolling radius of the measurement and MF-Tyre/MF-Swift model as a function of side slip angle for the Toyo tire at nominal conditions and a camber angle of 5°.

7.4 Review of the Model Results & Summary

This chapter compares three models with the measurements of Chapter 6, where each model is parameterized using a different approach. The linear model is parameterized for each individual measurement. The carcass stiffness of the nonlinear transient model is identified per measurement condition consisting of multiple measurements with different longitudinal slip values. The model relies on the calculated parameters from dedicated experiment results, the resulting steady-state curve of the linear model, and the measured states of the machine. Similarly, the *Magic Formula* parameters of the MF-Tyre/MF-Swift model are identified using dedicated experiments and the steady-state curves. The measurement results show that not every response reaches steady-state conditions. As a result, the steady-state curves, on which the nonlinear transient and MF-Tyre/MF-Swift model rely, are not entirely accurate.

The inherent machine issues influence the measured longitudinal transient response. Firstly, the play of the road in the x-direction has been identified as the main issue. This has already been resolved but only after the measurements presented in this work. Secondly, the constant part after the longitudinal slip step application, shown in Figure 6.7, reduces the accuracy of the model fitting and the longitudinal force response since this effect is not implemented in either of the models. Thirdly, the vertical force variation throughout the road displacement is suspected to affect the results, which is not accounted for in the linear and nonlinear transient models. Lastly, the measured road and wheel velocity, which are supplied as inputs to the models, provide low-quality signals. This influences the modeled response to a certain, unknown degree.

The presented results have to be judged from a qualitative perspective since the underlying measurements contain multiple, non-tire-related phenomena that influence the measured response. Nevertheless, the results from the three models show that the existing approaches are capable of representing longitudinal transient behavior with fair accuracy. The demonstrated results clearly show how the varying operating conditions influence the longitudinal transient response and model parameters.

Chapter 8

Conclusion and Recommendations

The goals of this thesis are to improve the Flat Plank Tire Tester capabilities in terms of software and hardware, together with a first investigation of the longitudinal transient behavior of pneumatic tires. Four objectives have been defined, which are the design of Simulink software and free-rolling controller, the measurement of the longitudinal tire response under varying operating conditions, and the evaluation of three tire models regarding the longitudinal transient response. Additionally, the status of the machine is described to provide a clear, structured overview of the current machine condition, the issues, limitations, and proposed solutions. This chapter describes the conclusions and recommendations for future research.

8.1 Conclusions

- This thesis and the measurements executed reflect the importance of maintenance and the impact of the incremental improvements that have been applied on the operational status of the machine. Multiple issues are identified that have an effect on the measured states of the machine, for which solutions are proposed. As a result, the quality of the measurement data and the ease of use of the machine is enhanced, where proposed and soon-to-be-implemented improvements will further increase the quality and ease of use.
- The objectives and requirements for the Speedgoat software are derived from the operating procedure of the machine. A graphical user interface and a control model are developed in MATLAB that comply with requirements and allow the logging of measurement data and controlling of the wheel rotation actuator. Additionally, they provide the foundation for future improvements of the machine in terms of the electric actuation of the different degrees of freedom.
- A controller is designed that regulates the torque of the wheel rotation actuator to recreate the free-rolling conditions of the mounted tire. The functional testing results on the Flat Plank demonstrate that the controller is capable of creating free-rolling conditions for typical passenger car tires throughout the allowable vertical force range of the machine. As a result, the controller provides a practical method to obtain measurement data for the identification of the effective rolling radius of a tire. The controller is not capable of creating free-rolling conditions for a racing car tire, presumably due to the high longitudinal slip stiffness.
- Two passenger car tires are subjected to nine longitudinal slip step levels to measure the longitudinal transient tire behavior. The vertical force, tire inflation pressure, side slip angle, and camber angle are varied to study their influence on the longitudinal force response. The measurement results clearly show the effects of the longitudinal slip magnitude and the operating conditions on the longitudinal transient behavior. However, multiple setup problems have been identified that affect the quality of the longitudinal transient response measurements up to a certain extent.
- The linear transient model and the nonlinear transient model of Pacejka [1] and the MF-Tyre/MF-Swift model [4] are parameterized using the measurement results. In general, the models represent the measured longitudinal transient response to a satisfactory degree within the limits of their assumptions. However, at this point, only qualitative conclusions can be drawn since the measurements contain non-tire related dynamics that influence the measured transient response and identified model parameters. Nevertheless, the Flat Plank provides the opportunity to research longitudinal transient behavior from a new perspective due to the application of longitudinal slip to a slowly rolling tire.

8.2 Recommendations

- The main recommendation is to resolve the hardware issues of the machine listed in Chapter 3. The longitudinal, lateral, and vertical play have already been resolved, which are the issues with the most substantial influence on the presented results. Nevertheless, resolving the remaining problems undoubtedly increases the quality of the measurement results.
- The forces and moments measured at the wheel center are used in the calculation of the forces and moments at the tire-road contact point. The wheel could only rotate freely or be fully locked before the implementation of the wheel rotation actuator. Therefore, it is assumed in the calculations that the moment about the spin axis of the wheel is equal to zero. This assumption may no longer hold, since the wheel rotation actuator provides a moment to track the reference rotational wheel velocity. It should be investigated whether and how to incorporate the moment delivered by the wheel rotation actuator in the force and moment calculations.
- The implementation of the Stöber-brand servomotors is planned. Additionally, the Automotive Technology lab personnel is working on the replacement of the encoders with state-of-the-art versions at the correct location. Both improvements will result in many benefits, which are listed below.
  - The free-rolling conditions created using the wheel rotation actuator in slip control vary from the free-rolling conditions created by the free-rolling controller, while they should be the same. It is presumed that this is caused by the mismatch in the longitudinal road velocity, but further investigation is required. The new road velocity encoder should measure the actual road velocity instead of deriving it from the pinion shaft velocity. Furthermore, it should provide a high-quality signal to use directly in the longitudinal slip control calculations instead of an average, constant value. As a result of these implementations, the investigation into the mismatch is better facilitated, It is also possible to compensate the rotational velocity of the wheel for anomalies in the longitudinal velocity of the road to obtain a more constant longitudinal slip value.
  - The actuation of the wheel rotation is delayed with respect to the road displacement actuation, which means that the tire requires approximately 1.5 m of road displacement to obtain free-rolling conditions. As a result, the effective road length for longitudinal slip measurements is significantly reduced. The implementation of the Stöber servomotors provides the opportunity to simultaneously start the two motions to directly start the tire at free-rolling conditions to utilize the full road length for measurements. It might be necessary to introduce a delay in the actuation of one of the motions due to the multiple backlashes and difference in inertia.
  - All measurements are influenced to a certain extent by the varying vertical force. A controller may be designed that regulates the vertical force to the desired reference value once the Stöber servomotors have been installed. The controller should have minimal overshoot to ensure that the reference is tracked as accurately as possible throughout the allowable vertical force range of the machine. It might be challenging to control the vertical force due to significant free play in the actuation of the vertical position. A different mechanical actuation of the vertical position might be required.
  - Similar to the vertical force variation, the steering angle is not constant due to play in the worm drive. Therefore, it is advised to create a controller that regulates the steering angle to the desired, constant value. Additionally, a controller that controls the steering velocity is beneficial to perform parking measurements.
  - It is observed that the tire generates a constant force for up to 0.1 m of road displacement after a low longitudinal slip value is applied. It is suspected that this is caused by the interaction of the backlashes in the gearboxes of the wheel rotation actuator and backlash in the rack-and-pinion gear of the plank actuation. This should be further investigated since the longitudinal force response is influenced by this phenomenon. The replacement of the encoders will support this investigation.
- Furthermore, it is recommended to repeat the longitudinal and combined slip measurements due to the non-tire-related dynamics of the machine. The measurements can be used to further investigate the accuracy of the modeling approaches for longitudinal transient behavior and draw quantitative conclusions on the model results.
- It should be investigated how the effective rolling radius identified with the free-rolling controller relates to the effective rolling radius determined when the flexplate drum is disconnected, especially during measurements with a steering and/or a camber angle. It is suggested to implement the dependency of the effective rolling radius on the steering and camber angle into MF-Tyre/MF-Swift, if the results are in line with the results presented in this thesis.
- The combined slip parameters of the MF-Tyre/MF-Swift model should be identified from the measurements rather than the MF-Tyre/MF-Swift model estimating these parameters.

- The decrease in the update frequency of the GUI lengthens the execution of measurements, since the GUI needs to be restarted every 30 to 45 minutes. It is expected that this restart time will decrease once the other motors are replaced with Stöber-brand versions due to the increased amount of data that will be transferred between the Host PC and the Speedgoat. Therefore, the cause of the update frequency reduction should be identified and resolved to reduce the required measurement time as much as possible.
- The parasitic force filter reduces the effect of the radial preloading of the flexplate drum on the measurement results. A better approach is to resolve the issue mechanically by redesigning the shaft end piece to achieve proper concentricity with the measurement shaft. Additionally, it is encouraged to address the proposal of Van Blijderveen [2] to reinstate the longer flexplate drum.
- A more sustainable solution should be found for the sandpaper attached to the plank to create road-like friction levels. The wear of the sandpaper is significant and this will affect the results when performing many pure longitudinal and combined slip measurements.

Bibliography

[1] H. Pacejka, *Tire and Vehicle Dynamics*, 3rd ed. Elsevier Ltd, 2012.

[2] D. van Blijderveen, "Extending the Flat Plank Tire Tester with Longitudinal Slip Speed Control," Master's thesis, Department of Mechanical Engineering, Eindhoven University of Technology, Eindhoven, The Netherlands, 2022, DC 2022.005.

[3] S. K. Clark, *Mechanics of Pneumatic Tires.* Ann Arbor: U.S. Depar, 1971.

[4] "Tire Simulation & Testing — Siemens Software." [Online]. Available: https://www.plm.automation.siemens.com/global/en/products/simulation-test/tire-simulation-testing.html

[5] P. W. A. Zegelaar, "The Dynamic Response of Tyres to Brake Torque Variations and road unevennesses," Ph.D. dissertation, Delft University of Technology, 1998.

[6] J. D. Gent, Alan N., Walter, *The Pneumatic Tire.* Akron: U.S. Department of Transportation, National Highway Traffic Safety Administration, 2006.

[7] "RMOD-K Overview." [Online]. Available: https://www.rmod-k.com/

[8] "Tyre Testing — TASS International." [Online]. Available: https://tass.plm.automation.siemens.com/tyre-testing

[9] M. H. M. Baart, "Electric Actuation of the Tire Measurement Tower and Tire Model Evaluation," Master's thesis, Department of Mechanical Engineering, Eindhoven University of Technology, Eindhoven, The Netherlands, 2020, DC 2020.027.

[10] "MTS Flat-Trac® Tire Force & Moment Measurement Systems." [Online]. Available: https://www.mts.com/en/products/automotive/tire-test-systems/flat-trac-tire-system

[11] J. P. M. Vissers and R. E. A. Blom, "Experiments on the flat plank tyre tester," Department of Mechanical Engineering, Eindhoven University of Technology, Eindhoven, The Netherlands, 2003, DCT 2003.92.

[12] T. H. J. Pijs, "Measuring Tire Deformation for the Validation of the TreadSim Tire Model," Master's thesis, Department of Mechanical Engineering, Eindhoven University of Technology, Eindhoven, The Netherlands, 2020, DC 2020.90.

[13] S. Shetty, "Optical Tire Deformation Measurement for the Validation of the TreadSim Tire Model," Department of Mechanical Engineering, Eindhoven University of Technology, Eindhoven, The Netherlands, 2020, DC 2020.124.

[14] C. Lugaro, F. Niedermeier, B. Wassertheurer, S. Huisman, and J. Schüling, "Advanced method for virtual tire and braking distance simulation," in *8th International Munich Chassis Symposium 2017*, P. D. P. E. Pfeffer, Ed. Wiesbaden: Springer Fachmedien Wiesbaden, 2017, pp. 757–778.

[15] S. Dinesh, "Magic Formula improvements for in-plane tyre behaviour," Master's thesis, Department of Mechanical Engineering, Eindhoven University of Technology, Eindhoven, The Netherlands, 2018, DC 2018.077.

[16] ——, "Transient Tire Model Validation and Parameterization," Department of Mechanical Engineering, Eindhoven University of Technology, Eindhoven, The Netherlands, 2017, DC 2017.102.

[17] "Speedgoat - The Quickest Path to Real-Time Simulation and Testing." [Online]. Available: https://www.speedgoat.com/

[18] M. Bergmans, “User Manual Flat Plank Tyre Tester,” Eindhoven University of Technology, Eindhoven, Tech. Rep., 2016.

[19] “IO317: Configurable FPGA I/O module.” [Online]. Available: https://www.speedgoat.com/products/simulink-programmable-fpgas-fpga-i-o-modules-io317

[20] “IO132: Simultaneous sampling 16-bit analog I/O support for Simulink.” [Online]. Available: https://www.speedgoat.com/products/io-connectivity-analog-io132

[21] “3M™ Safety-Walk™ Anti-Sliptape Standaard 600 Serie — 3M Nederland.” [Online]. Available: https://www.3mnederland.nl/3M/nl_NL/p/d/b00008058/

[22] “Equipment and Prototype Center.” [Online]. Available: https://www.tue.nl/universiteit/over-de-universiteit/diensten/equipment-and-prototype-center/

[23] “STÖBER Antriebstechnik: Getriebe, Motoren und Antriebsregler.” [Online]. Available: https://www.stoeber.de/

[24] “EnDat: proven interface technology continuously further developed.” [Online]. Available: https://www.endat.de/de_EN/

[25] F. Wei, M. Xing, S. Li, J. Shan, and B. Guan, “Physical and Mechanical Properties of Epoxy–Bauxite Mortar of High-Friction Surface Treatment,” *Journal of Materials in Civil Engineering*, vol. 32, no. 6, pp. 1–8, 2020.

[26] “What is LabVIEW? - NI.” [Online]. Available: https://www.ni.com/nl-nl/shop/labview.html

[27] “EtherCAT Technology Group — EtherCAT.” [Online]. Available: https://www.ethercat.org/en/technology.html

[28] G. F. Franklin, D. J. Powell, and A. Emami-Naeini, *Feedback Control of Dynamic Systems*, 7th ed. Pearson, 2015.

[29] S.-H. Kim, “Control of direct current motors,” *Electric Motor Control*, pp. 39–93, jan 2017.

[30] KTR, “Backlash-free servo couplings ROTEX GS - precise & low-priced — KTR.” [Online]. Available: https://www.ktr.com/in/products/rotex-gs/rotex-gs/

[31] J. C. Maré, “Friction modelling and simulation at system level: Considerations to load and temperature effects,” *Proceedings of the Institution of Mechanical Engineers. Part I: Journal of Systems and Control Engineering*, vol. 229, no. 1, pp. 27–48, 2015.

[32] M. Iskandar and S. Wolf, “Dynamic friction model with thermal and load dependency: Modeling, compensation, and external force estimation,” *Proceedings - IEEE International Conference on Robotics and Automation*, vol. 2019-May, no. 2, pp. 7367–7373, 2019.

[33] Y. Wu, Z. Wang, Y. Li, W. Chen, R. Du, and Q. Chen, “Characteristic modeling and control of servo systems with backlash and friction,” *Mathematical Problems in Engineering*, vol. 2014, 2014.

[34] J. Huang, C. Li, and B. Y. Duan, “Adaptive backstepping integral control of servo systems with backlash,” *Proceedings of the Institution of Mechanical Engineers. Part I: Journal of Systems and Control Engineering*, vol. 225, no. 8, pp. 1149–1162, 2011.

[35] A. J. Schmeitz, I. J. Besselink, J. De Hoogh, and H. Nijmeijer, “Extending the Magic Formula and SWIFT tyre models for inflation pressure changes,” *VDI Berichte*, no. 1912, pp. 201–225, 2005.

Appendix A

Force and Moment Calculation from Strain Gauge Output

The measurement hub, of which an outdated sketch is given in Figure A.1, uses three measuring crosses that contain strain gauges in a Wheatstone bridge configuration to determine the stress and strain on the measurement hub. The Wheatstone bridge outputs a certain voltage corresponding to a certain stress or strain. An overview of the forces and moments is given in Figure A.2.

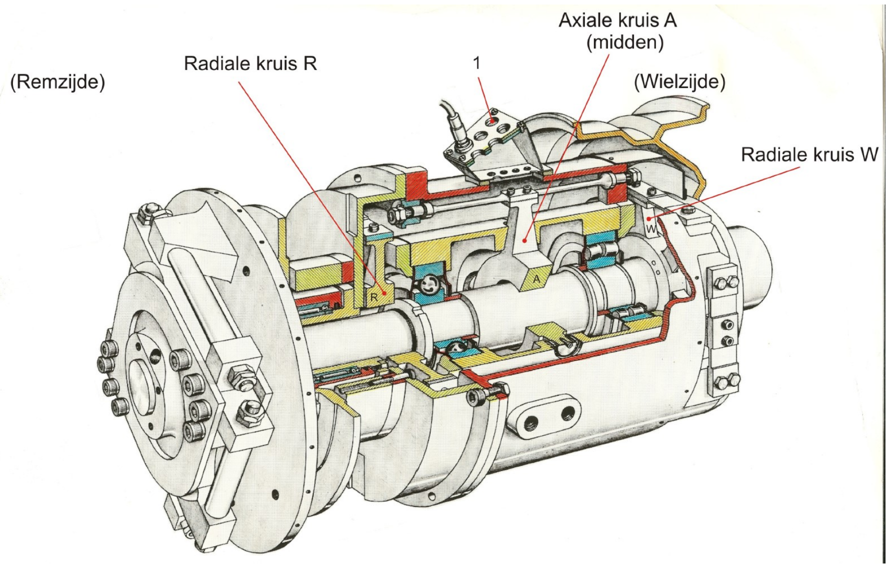

Figure A.1: Drawing with a partial cross-section of the measurement hub. Note that this sketch is outdated since the braking system is no longer mounted.

The output voltages of the strain gauges are converted to the forces and moments at the wheel center by the equations given below. The equations are taken from the LabVIEW software, and no documentation is available on the derivation of these equations. The symbols used in the equations are explained in Table A.1.

$$F_{xc} = -g\frac{4 \cdot 10^5}{A_{Fx}}\left(\frac{C_2}{k_{Fx1}} + \frac{C_3}{k_{Fx2}}\right), \tag{A.1a}$$

$$F_{yc} = g\frac{4 \cdot 10^5}{A_{Fy}k_{Fy}}C_1, \tag{A.1b}$$

$$F_{zc} = g\frac{4 \cdot 10^5}{A_{Fz}}\left(\frac{C_5}{k_{Fz2}} + \frac{C_6}{k_{Fz1}}\right), \tag{A.1c}$$

$$M_{xc} = g\frac{4 \cdot 10^5}{A_{Fz}}\left(\frac{C_5}{k_{Fz2}}(0.0475 - D_{ET} + D_A) + \frac{C_6}{k_{Fz1}}(0.3475 - D_{ET} + D_A)\right) \tag{A.1d}$$

$$M_{zc} = g\frac{4 \cdot 10^5}{A_{Fx}}\left(\frac{C_2}{k_{Fx1}}(0.3475 - D_{ET} + D_A) + \frac{C_3}{k_{Fx2}}(0.0475 - D_{ET} + D_A)\right). \tag{A.1e}$$

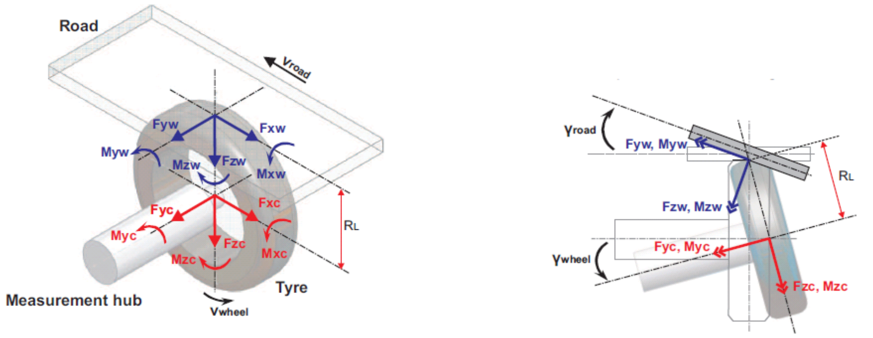

Isometric view **Side view**

Figure A.2: Forces and moments at the wheel center, subscript c, and at the tire-road contact point, subscript w. The ISO sign convention is used.

Table A.1: Symbols used in the force and moment calculation.

Symbol	Explanation	Value	Unit
C_1	Output of channel 1	-	V
C_2	Output of channel 2	-	V
C_3	Output of channel 3	-	V
C_5	Output of channel 5	-	V
C_6	Output of channel 6	-	V
k_{Fx1}	Wheatstone bridge constant of F_{x1}	3.5841	-
k_{Fx2}	Wheatstone bridge constant of F_{x2}	3.8158	-
k_{Fy}	Wheatstone bridge constant of F_y	3.8246	-
k_{Fz1}	Wheatstone bridge constant of F_{z1}	1.9775	-
k_{Fz2}	Wheatstone bridge constant of F_{z2}	1.9396	-
g	Gravitational acceleration	9.81	m/s^2
D_A	Thickness of mounted adapter	-	m
D_{ET}	ET-value of the mounted tire	-	m
A_{Fx}	Amplification factor for F_x of PIX Amplifier	1000	-
A_{Fy}	Amplification factor for F_y of PIX Amplifier	1000	-
A_{Fz}	Amplification factor for F_z of PIX Amplifier	1000	-

The moments and forces at the wheel center are used to determine those at the contact patch using

$$F_{xw} = F_{xc}, \tag{A.2a}$$
$$F_{yw} = \cos(\gamma)F_{yc} - \sin(\gamma)F_{zc}, \tag{A.2b}$$
$$F_{zw} = \sin(\gamma)F_{yc} + \cos(\gamma)F_{zc}, \tag{A.2c}$$
$$M_{xw} = M_{xc} - r_l F_{yc}, \tag{A.2d}$$
$$M_{yw} = r_l \cos(\gamma)F_{xc} - \sin(\gamma)M_{zc}, \tag{A.2e}$$
$$M_{zw} = r_l \sin(\gamma)F_{xc} + \cos(\gamma)M_{zc}, \tag{A.2f}$$

where r_l is the loaded wheel radius and γ is the total camber angle. The total camber angle is the sum of the camber angles of the measurement hub and the road.

Appendix B

Graphical User Interface

The four tabs of the GUI are shown in Figure B.1 to Figure B.4.

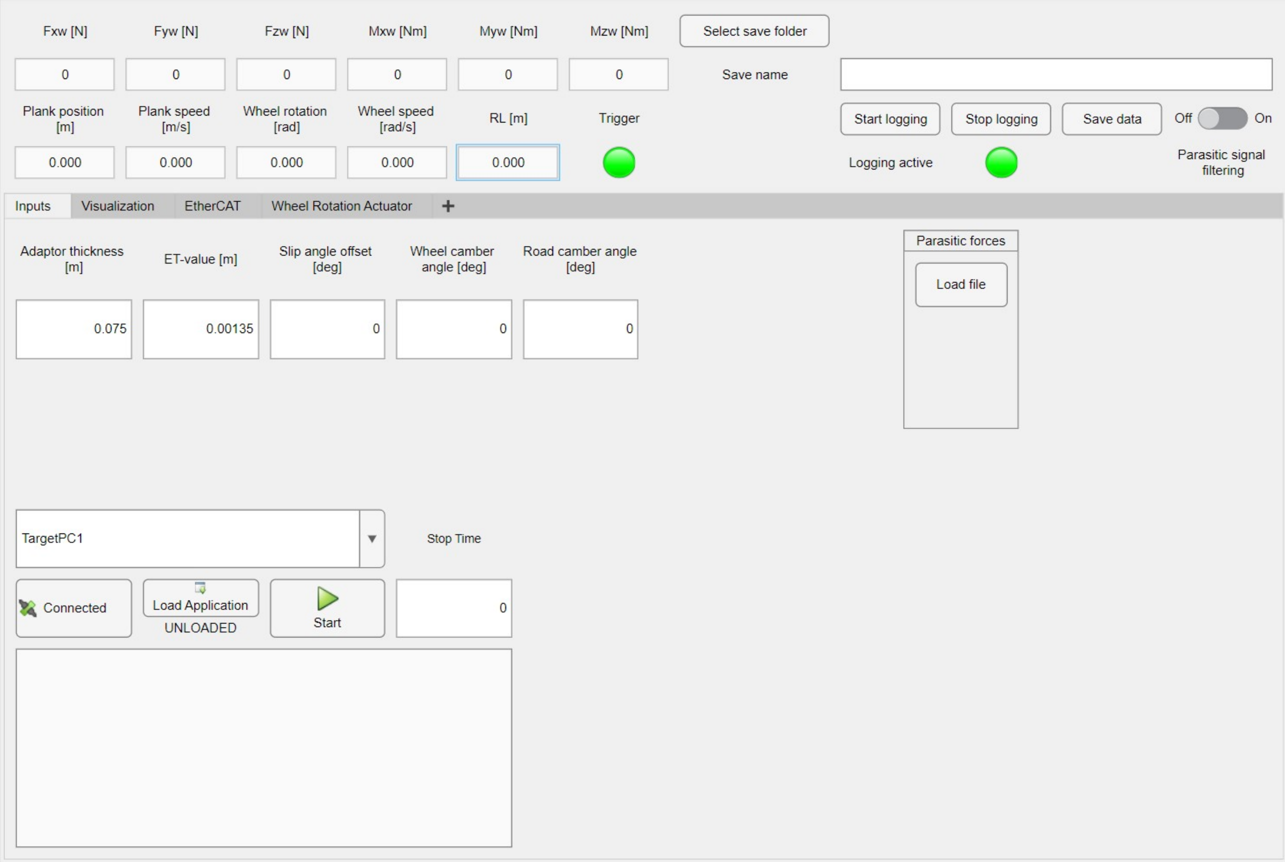

Fxw [N] 0
Fyw [N] 0
Fzw [N] 0
Mxw [Nm] 0
Myw [Nm] 0
Mzw [Nm] 0
Save name
Plank position [m] 0.000
Plank speed [m/s] 0.000
Wheel rotation [rad] 0.000
Wheel speed [rad/s] 0.000
RL [m] 0.000
Adaptor thickness [m] 0.075
ET-value [m] 0.00135
Slip angle offset [deg] 0
Wheel camber angle [deg] 0
Road camber angle [deg] 0
TargetPC1
Stop Time 0

Figure B.1: `Inputs` tab of the GUI.

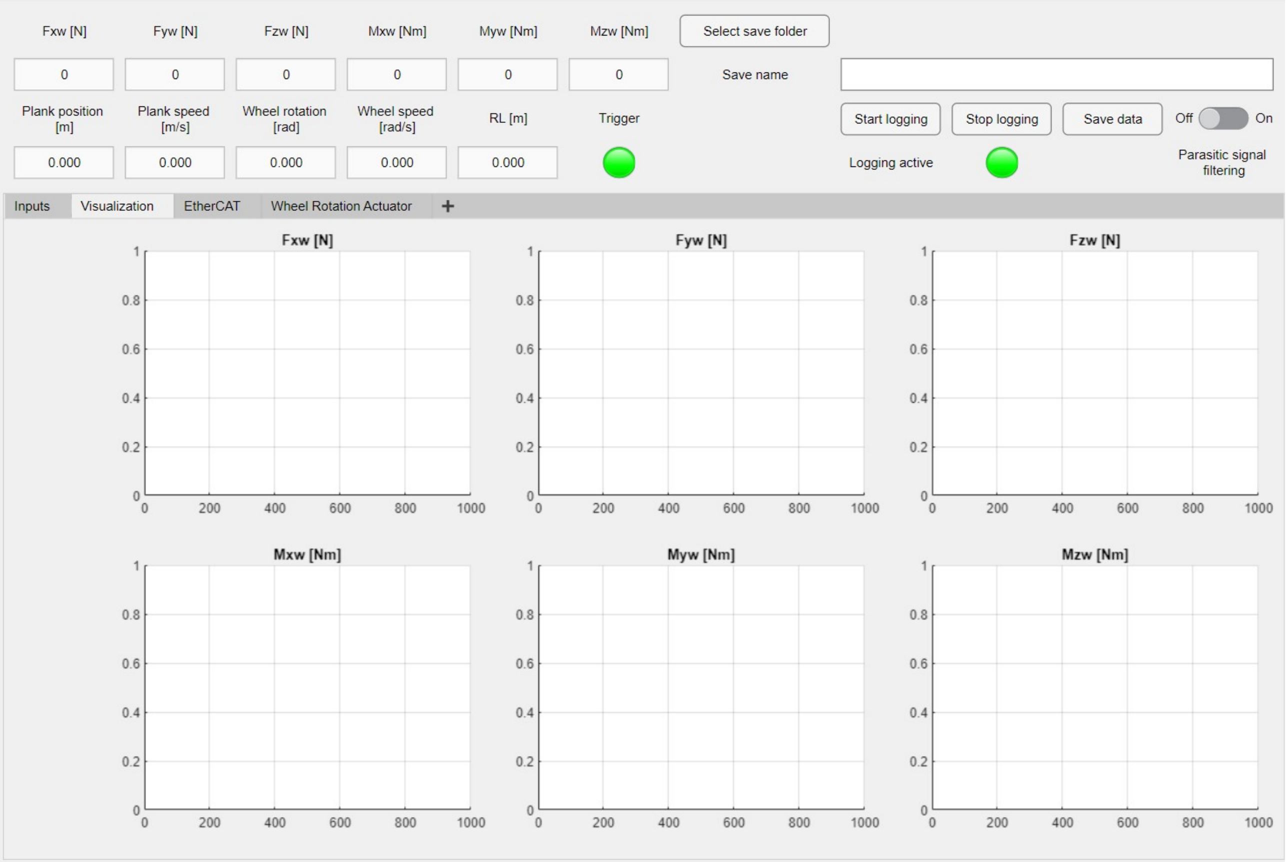

Fxw [N]	Fyw [N]	Fzw [N]	Mxw [Nm]	Myw [Nm]	Mzw [Nm]
0	0	0	0	0	0

Plank position [m]	Plank speed [m/s]	Wheel rotation [rad]	Wheel speed [rad/s]	RL [m]
0.000	0.000	0.000	0.000	0.000

Parasitic signal filtering: Off

Figure B.2: `Visualization` tab of the GUI.

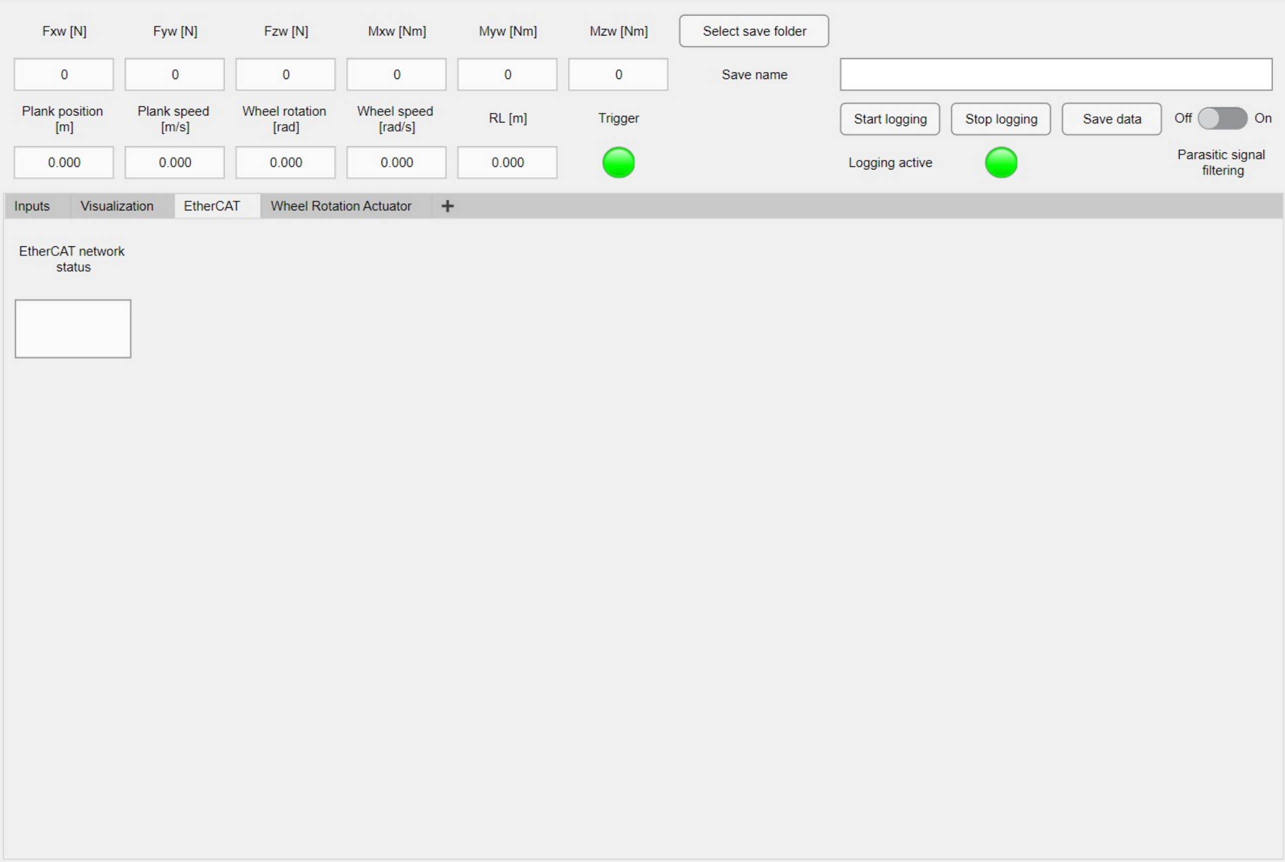

Fxw [N]	Fyw [N]	Fzw [N]	Mxw [Nm]	Myw [Nm]	Mzw [Nm]
0	0	0	0	0	0

Plank position [m]	Plank speed [m/s]	Wheel rotation [rad]	Wheel speed [rad/s]	RL [m]
0.000	0.000	0.000	0.000	0.000

Parasitic signal filtering: Off

Figure B.3: `EtherCAT` tab of the GUI.

Fxw [N]	Fyw [N]	Fzw [N]	Mxw [Nm]	Myw [Nm]	Mzw [Nm]
0	0	0	0	0	0

Plank position [m]	Plank speed [m/s]	Wheel rotation [rad]	Wheel speed [rad/s]	RL [m]
0.000	0.000	0.000	0.000	0.000

Operation mode
● No mode
○ Free Rolling
○ Longitudinal Slip Control
○ Homing
○ Wheel Position Control
○ Velocity Control
○ Torque Control

Waveform choice
● No mode
○ Sine
○ Constant
○ Triangle
○ Step
○ Double Step

Effective rolling radius [m] 0
Start distance [m] 1.5

Constant
Longitudinal slip [- 0

Step
Slip step value [-] 0

Sine & Triangle
Frequency for sine 0
Velocity for triangle [1/s] 0
Amplitude [-] 0
Number of periods ([0 inf]) 0
Direction (0 is positive, 1 is 0

Double step
Slip step value 1 [-] 0
Start distance 1 [m] 1.5
Slip step value 2 [-] 0
Start distance 2 [m] 2.5

Wheel position control
Target position [deg] 0
Actual position [deg]

Velocity control
Target velocity [RPM] 0
Actual velocity [RPM]

Free rolling & torque control
Effective rolling radius [m]
Actual torque [Nm]
Target torque [Nm] 0

Figure B.4: `Wheel Rotation Actuator` tab of the GUI.

Appendix C

Parasitic Signal Filtering

The flexplate drum of the wheel rotation actuator radially preloads the measurement shaft, which leads to parasitic longitudinal and vertical forces when the tire rotates. The parasitic forces are shown in Figure C.1, where the tire freely rotates with a constant rotational velocity. As shown in [2, Fig. 5.13], the parasitic forces are not velocity but position dependent. Van Blijderveen [2] states the preload is presumably due to the fact that the shaft end piece does not run true with the spin axis of the tire. Additionally, there is an inevitable play between the shaft end piece and the measurement shaft since the end piece is splined into the shaft. As a result, the runout is variable, which means that the parasitic signals may change throughout measurements.

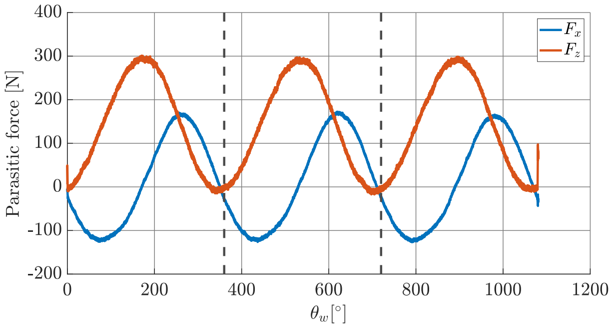

Figure C.1: Measured parasitic forces when the tire rotates freely at a constant rotational velocity.

The forces and moments that are generated by the tire are calculated using the output of the strain gauges. Therefore, the parasitic forces are a result of the parasitic strain gauge signals, which means that the filtering of the signals should be directly applied to the strain gauge output. These channels, equal to the channels in the force and moment calculation in Appendix A, are plotted in Figure C.2. This plot shows that the parasitic signals are sinusoidal with respect to the angular wheel position. The sinusoidal parameters per channel are identified, whereafter the sinusoidal signal is subtracted from the measured signals to reduce the influence of the preloading on the measurement results.

The identification procedure starts with performing a measurement where the tire rotates three full revolutions. The operator needs to save this measurement, whereafter he loads the same measurement using the dedicated button on the `Inputs` tab of the GUI. The data is trimmed to obtain the measurement data from 360° to 720° to remove the data where the tire is accelerated or decelerated to the constant velocity. This portion of data is indicated in Figure C.2 by the two vertical, dashed lines. Then, the A, B, C and D parameters of the sine function

$$y = A\sin(Bx + C) + D, \tag{C.1}$$

are fitted for each channel, where y is the strain gauge output and x is the angular wheel position. The trimmed measurement data and the resulting fit are shown in Figure C.3. The fitted parameters are provided to the subsystem in the control model. The parasitic signal is subtracted from the measured signal based on the measured wheel angular position if the operator enables the parasitic signal filtering in the GUI.

Figure C.4 shows the effect of the parasitic signal filtering if the tire is freely rotated at a constant velocity. The force amplitude reduces from approximately 300 N to approximately 25 N. Additional measurements have been performed to verify whether the parasitic signals change when the tire is vertically loaded and various longitudinal slip values are applied. Each measurement has been performed twice, once with the filtering

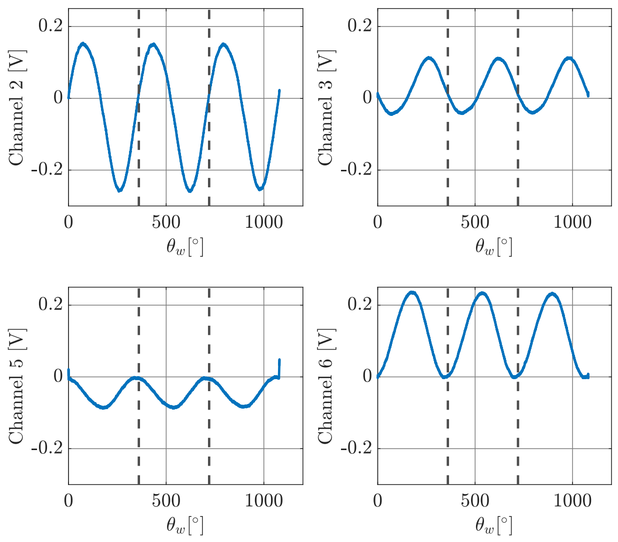

Figure C.2: Measured parasitic strain gauge outputs when the tire rotates freely at a constant rotational velocity.

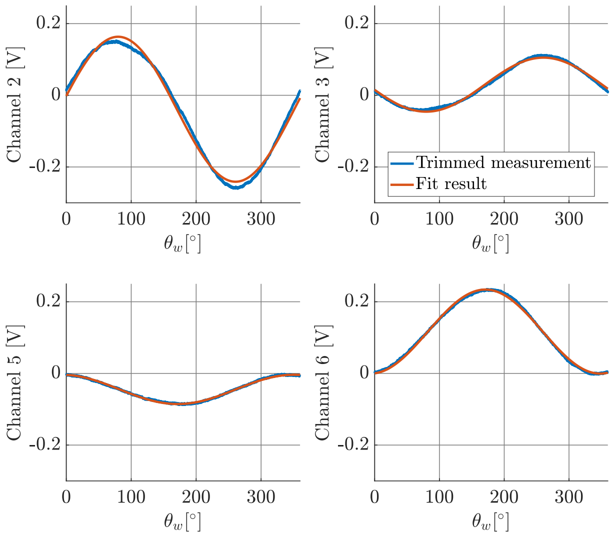

Figure C.3: Trimmed measurement data per channel, with the fitted result.

enabled and once without filtering. Previous measurements show that the measured forces are approximately equal when the same measurement is repeated ten times. Therefore, the filtered measurement is subtracted from the unfiltered one, which should approximately yield the parasitic forces. Figure C.5 and Figure C.6 show the calculated parasitic longitudinal and vertical force from the measurements for different slip values, and the parasitic forces that are calculated using the fit parameters from the parasitic signal filtering and the wheel angular position from the corresponding measurement. Both figures show that the amplitude and phase are approximately equal, but there is a difference in vertical offset for some results. The offset in vertical force can be the result of the difference in vertical loading conditions between the measurements. The vertical force is not constant between and throughout measurements since there is no controller that regulates the vertical forces. Additionally, the Stöber motor induces a significant amount of noise in the measurement signals, which is also not constant. Therefore, the measured forces vary between measurements under similar conditions due to noise.

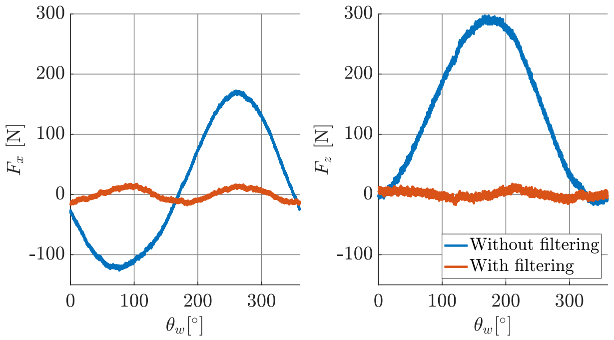

Figure C.4: Unfiltered and filtered parasitic forces when the tire is freely rotated at constant velocity.

The results presented in this appendix show that parasitic signal filtering reduces the influence of the preloading of the measurement shaft on the measurement results. The approach to identifying the required parameters is straightforward but might become cumbersome when multiple different tires have to be measured. Therefore, the filtering should be a temporary solution for the preloading and it is strongly advised to mechanically solve the problem using the suggested longer drum by Van Blijderveen [2] and reproduce the shaft end piece.

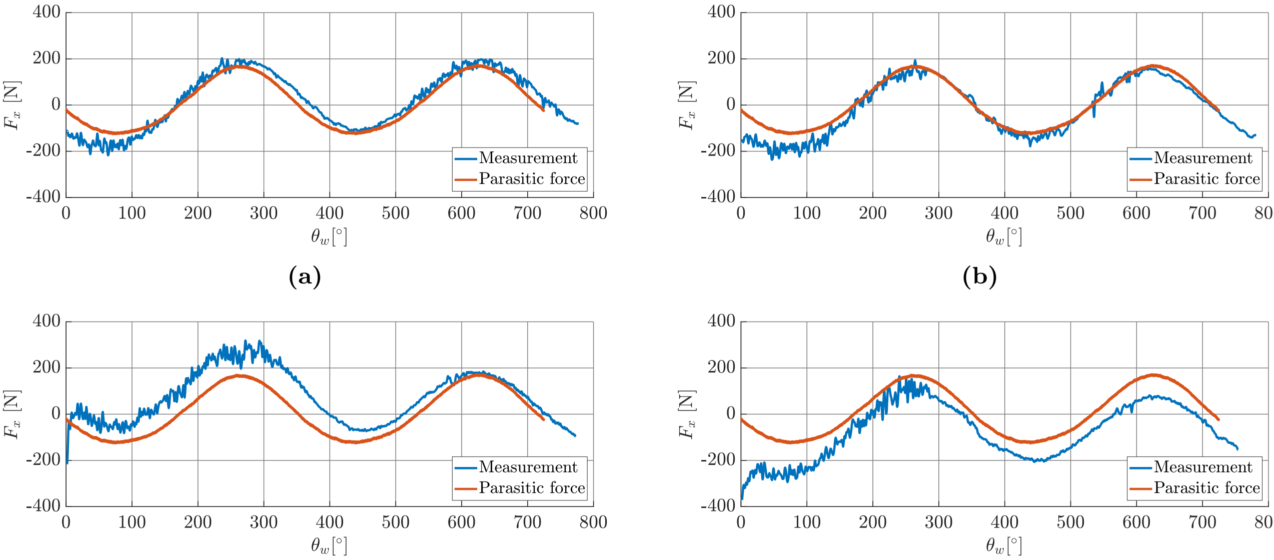

(a) (b)

(c) (d)

Figure C.5: Longitudinal parasitic forces for (a) $\kappa = 0\%$, (b) $\kappa = 1\%$, (c) $\kappa = -1\%$, (d) $\kappa = -5\%$. The measurement result is obtained by subtracting the filtered measurement from the unfiltered version, and the parasitic force is calculated from the fitted sine parameters for the strain gauge signals.

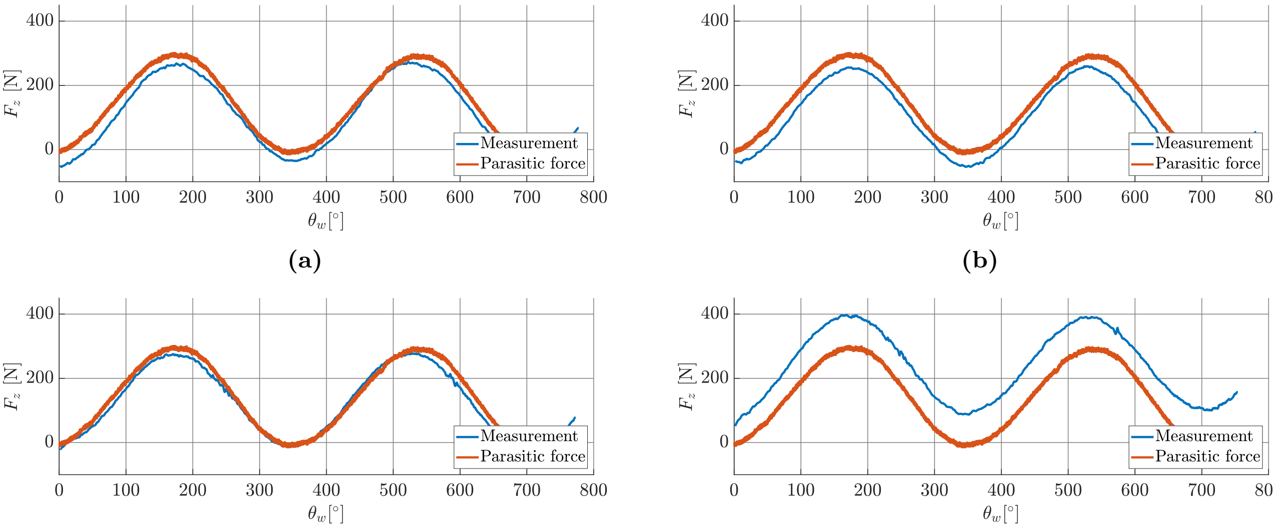

(a) (b)

(c) (d)

Figure C.6: Vertical parasitic forces for (a) $\kappa = 0\%$, (b) $\kappa = 1\%$, (c) $\kappa = -1\%$, (d) $\kappa = -5\%$. The measurement result is obtained by subtracting the filtered measurement from the unfiltered version, and the parasitic force is calculated from the fitted sine parameters for the strain gauge signals.

Appendix D

Calculation of the Effective Inertia of the Wheel Rotation Actuator

Firstly, the equations that describe the dynamics of the rotating parts of the actuator are determined using Newton's second law for rotation:

$$\tilde{M}_M - \frac{\tilde{M}_{WS}}{i_{RED}} = J_M \frac{d\tilde{\omega}_M}{dt}, \tag{D.1a}$$

$$\tilde{M}_{WS} - \frac{\tilde{M}_{SD}}{\eta i_{SD}} = J_{WS} \frac{d\tilde{\omega}_{WS}}{dt}, \tag{D.1b}$$

$$\tilde{M}_{SD} - \tilde{M}_T = (J_{WW} + J_T) \frac{d\tilde{\omega}_T}{dt}, \tag{D.1c}$$

where $\tilde{\omega}_M$ and $\tilde{\omega}_{WS}$ are the rotational velocities of the motor and worm screw, respectively. Since it is assumed that there is no backlash between the gears, it holds that

$$\tilde{\omega}_M = i_{SD} i_{RED} \tilde{\omega}_T, \tag{D.2a}$$

$$\tilde{\omega}_{WS} = i_{SD} \tilde{\omega}_T. \tag{D.2b}$$

Substituting (D.2) into (D.1) and rewriting gives

$$\tilde{M}_{WS} = i_{RED} \tilde{M}_M - i_{SD} i_{RED}^2 J_M \frac{d\tilde{\omega}_T}{dt}, \tag{D.3a}$$

$$\tilde{M}_{SD} = \eta i_{SD} \tilde{M}_{WS} - \eta i_{SD}^2 J_{WS} \frac{d\tilde{\omega}_T}{dt}, \tag{D.3b}$$

$$\tilde{M}_T = \tilde{M}_{SD} - (J_{WW} + J_T) \frac{d\tilde{\omega}_T}{dt}. \tag{D.3c}$$

Substituting (D.3a) and (D.3b) into (D.3c) gives

$$\tilde{M}_T = \eta i_{SD} i_{RED} \tilde{M}_M - \left(J_{WW} + J_T + \eta i_{SD}^2 (J_{WS} + i_{RED}^2 J_M)\right) \frac{d\tilde{\omega}_T}{dt}. \tag{D.4}$$

The worm wheel torque $\tilde{M}_{WW}$ is equal to

$$\tilde{M}_{WW} = \tilde{M}_{WS} - \tilde{M}_T = \eta i_{SD} i_{RED} \tilde{M}_M, \tag{D.5}$$

which means that (D.4) simplifies to

$$\tilde{M}_{WW} = \left(J_{WW} + J_T + \eta i_{SD}^2 (J_{WS} + i_{RED}^2 J_M)\right) \frac{d\tilde{\omega}_T}{dt}. \tag{D.6}$$

Therefore, the effective inertia J_{eff} in (5.4) is equal to

$$J_{eff} = J_{WW} + J_T + \eta i_{SD}^2 \left(J_{WS} + i_{RED}^2 J_M\right). \tag{D.7}$$

Appendix E

Settling Distance Calculation

To determine the settling distance of a measurement, it is convenient to fit a smooth function to the measurement data to improve the accuracy of the calculation. Due to noise and oscillations in the measured longitudinal force, it is difficult to accurately calculate the settling distance.

Therefore, a function is fitted to the measurement data. When observing the shape of the measured longitudinal force for a road displacement between 0.1 m and 4.2 m as shown in Figure E.1, an exponential curve can be seen. The exponential function that is fitted is given by

$$y(x) = p_1 \exp(-p_2 x) + p_3, \tag{E.1}$$

where x is the road displacement, y is the fitted longitudinal force, and p_1 to p_3 are fit parameters. The function is fitted using the Matlab function `lsqvurvefit` that minimizes the error between the measurement and the fit function in a least-squares sense. The resulting fitted curve is then used to calculate the settling distance by finding the road displacement where $|y_{ref} - y(x)| \leq 0.05 y_{ref}$, where $y_{ref} = 50$ N. The settling distance is indicated in the figure by the dashed orange vertical line and is equal to 1.55 m.

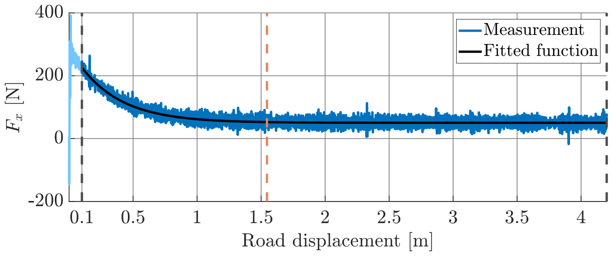

Figure E.1: Measured longitudinal tire force and the fitted exponential function, plotted against the road displacement.

Appendix F

Measurement Data File Structure & Naming Convention

This appendix describes the file structure and naming convention of the measurement data, which is stored on the fileserver of the AT lab. The naming structure is similar to the structure used by TNO, which is described in the manual of the Flat Plank. The measurement data is stored in folder `TASS - Aertssen`, where each type of measurement has its dedicated subfolder. The structure is shown below, together with the naming convention for the folders.

- `TASS - Aertssen`
  ↳ `ERR`: Effective rolling radius measurements,
  ↳ `REL_COM`: Relaxation measurements combined slip without camber,
  ↳ `REL_COM_CAM`: Relaxation measurements combined slip with camber,
  ↳ `REL_LNG`: Relaxation measurements longitudinal slip without camber,
  ↳ `REL_LNG_CAM`: Relaxation measurements longitudinal slip with camber,
  ↳ `REP_REL`: Repetition of relaxation measurements for longitudinal and combined slip without camber,
  ↳ `STF`: Stiffness measurements

In the folders, the naming structure is as follows: `XXX_VVV_ZZZ_T_pXX_FzYYYY_N`

- `XXX` is the tire name, being `TOY` for the Toyo tire and `BMW` for the Continental tire.
- `VVV` is the type of measurement, which is equal to the folder structure given above.
- `ZZZ` gives the κ, α, and γ settings corresponding to the measurement. `A` indicates the camber angle in degrees, `B` gives the steering angle in degrees, and `C` indicates the longitudinal slip value in percentages.
  - `ERR`: corresponding to the operating condition, e.g. `REL_COM`, without `_Cperc`,
  - `REL_COM`: `Bdeg_Cperc`,
  - `REL_COM_CAM`: `Adeg_Bdeg_Cperc`,
  - `REL_LNG`: `Cperc`,
  - `REL_LNG_CAM`: `Adeg_Cperc`,
  - `REP_REL`: `Cperc` for longitudinal slip, `Adeg_Cperc` for combined slip,
  - `STF`: empty.
- `T` is the identification of the tire, which is unused in this project and kept equal to `T`.
- `pXX` indicates the tire inflation pressure, where `XX` is the tire inflation pressure in bar multiplied by a factor of ten.
- `FzYYYY` is the vertical force, where `YYYY` is the vertical force in Newton to which the tire is subjected.
- `N` indicates the starting position.

So, for example, the following measurements are performed.

- `BMW_ERR_REL_LNG_T_p23_Fz1625_1`: An effective rolling measurement for the Continental tire for pure longitudinal slip, at a tire pressure of 2.3 bar, a vertical force of 1625 N and from starting position 1.
- `TOY_REL_LNG_5perc_T_p25_Fz5550_2`: A longitudinal relaxation measurement for the Toyo tire at 5% longitudinal slip, a tire pressure of 2.5 bar, a vertical force of 5550 N and from starting position 2.
- `TOY_REL_COM_CAM_5deg_1deg_2perc_T_p25_Fz3700_3`: A combined slip measurement with camber for the Toyo tire. The camber angle is 5°, the steering angle is 1°, the longitudinal slip value is 2%, the tire pressure is 2.5 bar, the vertical force is 3700 N and the starting position is 3.

Appendix G

Contact Patch and Stiffness Measurement Results

G.1 Contact Patch Measurements

The contact patch measurements of the Toyo tire at nominal tire pressure and three vertical forces are shown in Figure G.1 to Figure G.3. The contact patch dimensions increase with increasing vertical force, corresponding to the theory [1]. Half of contact length a is plotted against the vertical force in Figure G.4.

Figure G.1: Contact patch measurement for $F_z = 1850$.

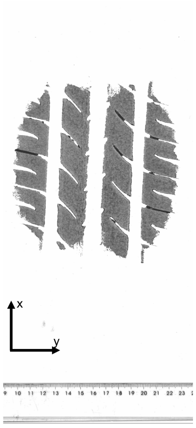

Figure G.2: Contact patch measurement for $F_z = 3700$.

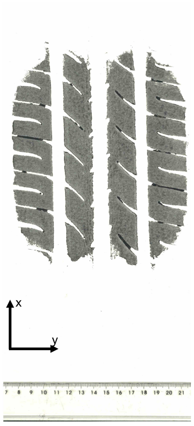

Figure G.3: Contact patch measurement for $F_z = 5550$.

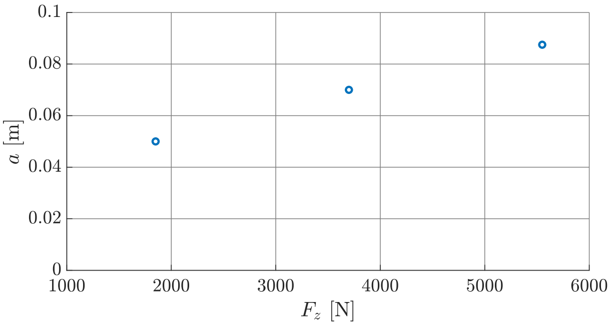

Figure G.4: Half of contact length a plotted against the vertical force for the Toyo tire for nominal tire pressure.

G.2 Stiffness Measurements

The vertical stiffness measurements for the Toyo tire for 2 bar and 2.5 bar are given in Figure G.5. The force responses show a slight decrease in force growth between $r_l = 0.305$ m and $r_l = 0.310$ m, which is presumably due to the play between the half-moon guides and rotation supports. Therefore, the data indicated in lighter colors is used to determine the vertical stiffness ($r_l \in [0.285\ 0.305]$). The figure shows two distinct lines per tire pressure, one for loading and unloading the tire. The vertical stiffness is determined by fitting the linear relation between the loaded wheel radius and the vertical force for both loading and unloading conditions, whereafter the two values are averaged to obtain the vertical stiffness for both tire pressures. The dashed lines in Figure G.5 indicate the fit result. The resulting vertical stiffness values are visualized in Figure G.6 and are equal to $1.77 \cdot 10^5$ N/m for $p = 2$ bar and $2.13 \cdot 10^5$ N/m for $p = 2.5$ bar.

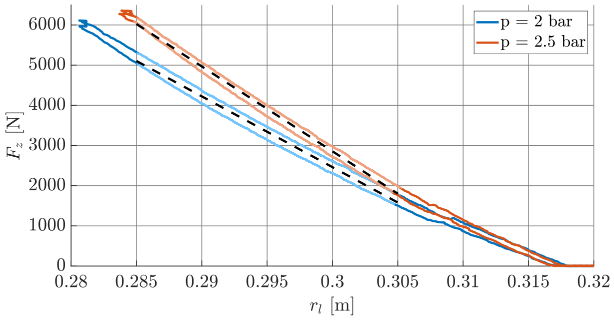

Figure G.5: Vertical stiffness measurement for $p = 2$ bar and $p = 2.5$ bar. The light-colored part of the measurements is used for the identification of the vertical stiffness.

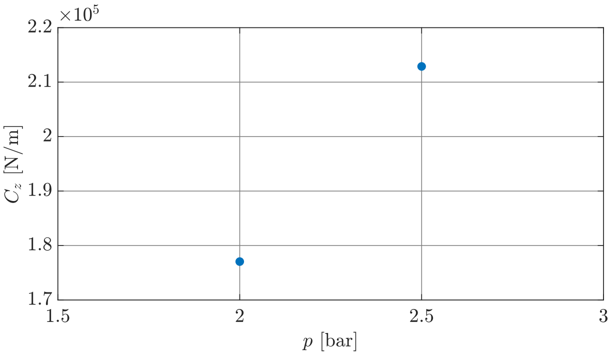

Figure G.6: Vertical stiffness C_z plotted against the tire pressure for the Toyo tire.

Appendix H

RMSE Values

H.1 Nonlinear Transient Model

In Table H.1, the RMSE values of the nonlinear transient model with respect to the measurements for varying operating conditions are given.

Table H.1: RMSE values of the nonlinear transient model for varying operating conditions.

$\boldsymbol{\kappa}$ [%]	**-10**	**-5**	**-2**	**-1**	**0**	**1**	**2**	**5**	**10**
$F_z = 1850$ N [N]	68	50	32	42	31	69	59	28	50
$F_z = 3700$ N [N]	171	139	51	38	43	108	129	78	80
$F_z = 5550$ N [N]	161	167	91	73	47	95	141	131	115
$p = 2$ bar [N]	162	140	63	55	43	98	123	98	82
$p = 2.5$ bar [N]	171	139	51	38	43	108	129	78	80
$\gamma = 0°$ [N]	171	139	51	38	43	108	129	78	80
$\gamma = 5°$ [N]	213	168	63	34	33	96	144	91	96
$\alpha = 0°$ [N]	171	139	51	38	43	108	129	78	80
$\alpha = 1°$ [N]	161	146	57	33	38	96	136	65	82
$\alpha = 5°$ [N]	146	98	40	32	28	31	42	45	89
$\alpha = 10°$ [N]	68	27	28	31	22	30	31	51	85

H.2 MF-Tyre/MF-Swift Model

In Table H.2, the RMSE values of the MF-Tyre/MF-Swift model with respect to the measurements for varying operating conditions are given.

Table H.2: RMSE values of the MF-Tyre/MF-Swift model for varying operating conditions.

$\boldsymbol{\kappa}$ [%]	**-10**	**-5**	**-2**	**-1**	**0**	**1**	**2**	**5**	**10**
$F_z = 1850$ N [N]	124	45	50	68	32	49	50	52	122
$F_z = 3700$ N [N]	253	179	87	40	52	101	108	106	116
$F_z = 5550$ N [N]	315	259	112	206	56	119	175	165	141
$p = 2$ bar [N]	281	208	107	46	60	75	141	129	117
$p = 2.5$ bar [N]	253	179	87	40	52	101	108	106	116
$\gamma = 0°$ [N]	253	179	87	40	52	101	108	106	116
$\gamma = 5°$ [N]	216	135	63	45	54	102	118	130	241
$\alpha = 0°$ [N]	253	179	87	40	52	101	108	106	116
$\alpha = 1°$ [N]	168	88	41	28	46	115	152	89	183
$\alpha = 5°$ [N]	235	123	65	42	39	25	51	50	133
$\alpha = 10°$ [N]	371	201	69	27	24	45	70	167	265

Appendix I

MF-Tyre/MF-Swift Parameters

Table I.1 lists the MF-Tyre/MF-Swift parameters for the Toyo NanoEnergy and Continental EcoContact tires. The parameters have been identified by minimizing the error between the measured and modeled values using `fmincon` in MATLAB.

Table I.1: MF-Tyre/MF-Swift parameters for the Toyo NanoEnergy and Continental EcoContact tires.

	Toyo NanoEnergy	**Continental EcoContact**
LONGVL	0.03	0.03
VXLOW	0	0
UNLOADED_RADIUS	0.3173	0.3498
WIDTH	0.195	0.155
RIM_RADIUS	0.1905	0.2413
NOMPRES	250000	280000
FNOMIN	3700	3250
VERTICAL_STIFFNESS	213000	241000
PFZ1	0.5243	0.8078
BREFF	3.2036	3.2525
DREFF	0.2743	0.2566
FREFF	0.0219	0.0187
Q_RE0	1	1
Q_V1	0	0
LONGITUDINAL_STIFFNESS	162230	167180
PCFX1	0.121	0.125
PCFX2	0.073	0.001
PCFX3	0.261	0.154
Q_RA1	0.9244	0.8773
Q_RA2	0.1201	0.4555
PCX1	1	1
PDX1	1.0157	1.002
PDX2	-0.0976	-0.083
PDX3	2.0216	0
PEX1	-0.8172	-1.331
PEX2	-1.9513	-2.487
PEX3	0.5553	0.6
PEX4	-0.9000	-0.9
PKX1	27.5806	27.114
PKX2	-7.9134	14.957
PKX3	0.5000	-0.5
PHX1	-0.0015	0
PHX2	-0.0011	-0.001
PVX1	0.0979	0.072
PVX2	0.0002	0.002
PPX1	-0.5508	-0.888
PPX2	2.4801	0.482

Table I.1: MF-Tyre/MF-Swift parameters for the Toyo NanoEnergy and Continental EcoContact tires.

	Toyo NanoEnergy	**Continental EcoContact**
PPX3	0.0234	0.825
PPX4	-0.4468	2.103
PCY1	1	1
PDY1	0.929	1.121
PDY2	0	0
PDY3	0.956	0
PEY1	0.396	0.667
PEY2	0	0
PEY3	0	0
PEY4	18.547	0
PEY5	-22.97	0
PKY1	-23.734	-15.148
PKY2	0	0
PKY3	0.038	0
PKY4	1.609	1.123
PKY5	0	0
PKY6	0.093	0.122
PKY7	0	0
PHY1	-0.01	0
PHY2	0	0
PVY1	0.1	-0.09
PVY2	0	0
PVY3	0.063	0
PVY4	0	0
PPY1	0	0
PPY2	0	0
PPY3	0	0
PPY4	0	0
PPY5	0	0